

**Volume 1, Issue 1**

**2010**

**Special Topics & Reviews in  
Porous Media  
An International Journal**

**KAMBIZ VAFAI**  
EDITOR-IN-CHIEF



begell house, inc.  
publishers

## **AIMS AND SCOPE**

Special Topics & Reviews in Porous Media-An International Journal (STRPM) publishes up-to-date research works related to special topics and reviews covering a wide range of fields related to porous media. Special topics and reviews can be related to applications and research areas in contemporary and traditional technology, such as biological, electronics cooling, thermal insulation engineering, geothermal and environmental engineering, heat pipes, underground spreading of chemical waste, nuclear waste repository, grain storage, enhanced recovery of petroleum reservoirs, packed bed heat exchangers, drying technology, catalytic reactors, petroleum industries, geothermal systems, tissue engineering, drug delivery, avionics, miniature refrigerators, nanoporous materials, microtextured surfaces for enhanced boiling, particle migration and deposition; material processing applications; particle transport and deformable porous bodies; direct contact heat exchangers, coal combustors, nuclear waste repositories, experimental and measuring techniques; industrial and environmental heat transfer and flow, characterization of porous materials, etc. This journal provides a comprehensive forum for communication between researchers and practicing engineers. The excellence of contributions is assured through a rigorous peer review process. STRPM is the only journal of its kind that covers the entire spectrum related to special topics and reviews covering a wide range of fields related to porous media.

# Special Topics & Reviews in Porous Media

## An International Journal

**EDITOR-IN-CHIEF**

**KAMBIZ VAFAI**

Department of Mechanical Engineering  
University of California, Riverside  
A 363 Bourns Hall, Riverside, CA 92521-0425

### **EDITORIAL ADVISORY BOARD**

---

**A. BEJAN**

Department of Mechanical Engineering  
Duke University  
Durham, NC 27706

**P. CHENG**

School of Mechanical and Power Engineering  
Shanghai Jiaotong University  
1954 Hua Shan Road, Shanghai 200030, P.R. China

**FARUK CIVAN**

Mewbourne School of Petroleum and Geological Eng.  
University of Oklahoma  
Norman, OK

**M. J. S. DE LEMOS**

Department of Energy, IEME/ITA/CTA  
San Jose dos Campos, Sao Paulo 12228-900, Brazil

**W. G. GRAY**

Department of Environmental Sciences and Engineering  
University of North Carolina  
Rosenau Hall, CB #7431, Chapel Hill, NC 27599-7431

**S. M. Hassanizadeh**

Department of Earth Sciences  
Utrecht University  
Utrecht, Netherlands

**J. H. HE**

College of Science, Inst. of Physics of Fibrous Soft Matter  
Donghua University  
Shanghai 200051, China

**C. E. HICKOX, JR.**

Engineering Sciences Center, Sandia National Labs  
Albuquerque, NM 87185

**M. KAVIANY**

Dept. of Mechanical Engineering and Applied Mechanics  
University of Michigan  
Ann Arbor, MI 48109

**J. H. MASLIYAH**

Department of Chemical Engineering  
University of Alberta  
Edmonton, Alberta T6G 206, Canada

**R. MC KIBBIN**

Institute of Information and Mathematical Sciences  
Massey University at Albany  
Auckland, New Zealand

**W. J. MINKOWYCZ**

Department of Mechanical Engineering (M/C251)  
University of Illinois at Chicago  
Chicago, IL 60607

**A. NAKAYAMA**

Department of Mechanical Engineering  
Shizuoka University  
3-5-1 Johoku, Hamamatsu 432-8561, Japan

**V. E. NAKORYAKOV**

Institute of Thermal Physics  
Siberian Branch of the Academy of Sciences of Russia  
Novosibirsk, 630090, Russia

**D. A. NIELD**

Department of Engineering Science  
University of Auckland  
Auckland, New Zealand

**D. Or**

Department of Environmental Sciences  
Institute of Terrestrial Ecosystems  
Soil and Terrestrial Environmental Physics  
Zurich, Switzerland

**V. PARKHUTIK**

Materials Science R&D Centre MTM,  
Ciudad Politecnica de Innovacion, Edificio 8G, Seccion C  
Cami de Vera s/n 46022 Valencia, Spain

**I. POP**

Faculty of Mathematics  
University of Cluj  
R-3400 Cluj, CP 253, Romania

**D. POULIKAKOS**

Department of Mechanical and Process Engineering  
Institute of Energy Technology  
Swiss Federal Institute of Technology (ETH)  
ETH Center, Zurich, Switzerland

**D. A. S. REES**

Department of Mechanical Engineering  
University of Bath  
Claverton Down, Bath, BA2 7A Y, UK

**N. RUDRAIAH**

Dept. of Mathematics, UGC-DSA Center in Fluid Mechanics  
Natl. Research Inst. for Applied Mathematics  
Bangalore University, Bangalore-560 001, India

**M. SAHIMI**

Department of Chemical Engineering  
University of Southern California  
Los Angeles, CA 90089

**S. WHITAKER**

Department of Chemical Engineering  
University of California, Davis  
Davis, CA 95616

---

# SPECIAL TOPICS & REVIEWS IN POROUS MEDIA — AN INTERNATIONAL JOURNAL

Volume 1, Number 1, 2010

---

## CONTENTS

<b>Key Issues to Enable High Heat Flux Removal Exceeding 10 MW/m<sup>2</sup> by Use of Metal Porous Media as a Latent Heat-Transfer Device</b>	<b>1</b>
<i>K. Yuki, H. Hashizume, &amp; S. Toda</i>	
<b>Thermohydrodynamic Instability of Viscous Rotating Dielectric Fluid Layer in Porous Medium with Vertical AC Electric Field</b>	<b>15</b>
<i>M.F. El-Sayed</i>	
<b>Study on the Longitudinal Gas Permeability of Juvenile Wood and Mature Wood</b>	<b>31</b>
<i>H.R. Taghiyari, A.-N. Karimi, D. Parsapajouh, &amp; K. Pourtahmasi</i>	
<b>Wettability Effects in Gas Gravity—Assisted Flow as Related to Displacement Instability</b>	<b>39</b>
<i>B. Rostami, R. Kharrat, V. Alipour Tabrizy, M. Khosravi, &amp; C. Ghotbi</i>	
<b>Theory, Method, and Application of a Numerical Simulation in an Oil Resources Basin Methods of Numerical Solutions of Aerodynamic Problems</b>	<b>49</b>
<i>Y.-R. Yuan, W.-G. Wang, &amp; Y.-J. Han</i>	
<b>On Flexural Vibrations of Poroelastic Circular Cylindrical Shells Immersed in an Acoustic Medium</b>	<b>67</b>
<i>S. A. Shah &amp; M. Tajuddin</i>	
<b>Reconciliation of Packed Column Permeability Data—Part 1. The Teaching of Giddings Revisited Fluctuations</b>	<b>79</b>
<i>H. M. Quinn</i>	

---

*Special Topics & Reviews in Porous Media – An International Journal* (ISSN: 2151-4798) is published 4 times per year and is owned by Begell House, Inc. 50 Cross Highway, Redding, Connecticut 06896, Phone (203) 938-1300. USA subscription rate for 2010 is \$625.00. Add \$10.00 per issue for foreign airmail shipping and handling fees for all orders shipped outside the United States or Canada. All subscriptions are payable in advance. Subscriptions are entered on an annual basis, i.e., January to December. For immediate service and charge card sales, please call (203) 938-1300 Monday through Friday 9 AM — 5 PM EST. Orders can be faxed to (203) 938-1304 or mailed to Subscriptions Department, Begell House, Inc. 50 Cross Highway, Redding, Connecticut 06896.

Copyright © 2010 by Begell House, Inc. All rights reserved. Printed in the United States of America. Authorization to photocopy items for internal or personal use, or the internal or personal use of specific clients, is granted by Begell House, Inc. for libraries and other users registered with the Copyright Clearance Center (CCC) Transactional Reporting Service, provided that the base fee of \$35.00 per copy, plus .00 per page is paid directly to CCC, 222 Rosewood Drive, Danvers, MA 01923, USA. For those organizations that have been granted a photocopy license by CCC, a separate system of payment has been arranged. The fee code for users of the Transactional Reporting Service is [ISSN 2151-562X \$35.00 + \$0.00]. The fee is subject to change without notice.

Begell House, Inc.'s consent does not extend to copying for general distribution, for promotion, for creating new works, or for resale. Specific permission must be obtained from Begell House, Inc. for such copying.

This journal contains information obtained from highly regarded sources. Reprinted material is quoted with permission, and sources are indicated. A wide variety of references are listed. Reasonable efforts have been made to publish reliable data and information, but the editor and the publisher assume no responsibility for any statements of fact or opinion expressed in the published papers or in the advertisements.

Printed February 26, 2010

# KEY ISSUES TO ENABLE HIGH HEAT FLUX REMOVAL EXCEEDING 10 MW/M<sup>2</sup> BY USE OF METAL POROUS MEDIA AS A LATENT HEAT-TRANSFER DEVICE

Kazuhisa Yuki,<sup>1,\*</sup> Hidetoshi Hashizume,<sup>2</sup> & Saburo Toda<sup>2</sup>

<sup>1</sup>Department of Mechanical Engineering, Faculty of Engineering, Tokyo University of Science, Yamaguchi, Daigaku-dori 1-1-1, Sanyo-Onoda, Yamaguchi, 756-0884 Japan

<sup>2</sup>Department of Quantum Science and Energy Engineering, Graduate School of Engineering, Tohoku University, Aramaki-Aoba 6-6-01-2, Aoba, Sendai, Miyagi, 980-8579, Japan

\*Address all correspondence to K. Yuki E-mail: kyuki@ed.yama.tus.ac.jp

Original Manuscript Submitted: 7/6/2007; Final Draft Received: 8/19/2009

Heat transfer characteristics of two-phase flow in particle-sintered porous media are experimentally investigated in order to clarify the key issues to enable extremely high heat flux removal exceeding 10 MW/m<sup>2</sup>. The porous media experimented on are stainless steel particle-sintered and bronze particle-sintered compacts. The experiments under some heat flux inputs clarify that the effects of porous structure such as pore size and porosity on the heat transfer characteristics highly depend on the level of the heat flux input. The results suggest that liquid-vapor exchange due to capillary and pumping effects works effectively under several MW/m<sup>2</sup> in this cooling system. However, under conditions exceeding the heat flux level, permeability for vapor discharge outside the porous medium becomes the most important factor in enabling the heat flux removal of over 10 MW/m<sup>2</sup>. Furthermore, in order to evaluate what kind of porous material is appropriate for higher heat removal, the two-phase flow characteristics in the porous media are simulated by the two-phase mixture model. The results show that utilizing a higher thermal-conductivity matrix facilitates a delay in the onset of the phase change near the heating wall and leads to much higher heat flux removal, even at the same liquid saturation, compared with the case utilizing a lower thermal-conductivity matrix.

**KEY WORDS:** metal porous media, high heat flux removal, two-phase flow, two-phase mixture model

## 1. INTRODUCTION

In the development of a nuclear fusion reactor, it is critically important not only to prove its engineering feasibility by operating an international thermonuclear experimental reactor (ITER) that will be constructed in France, but to also work toward promoting new technology for the development of a commercial reactor. In particular, extremely high heat flux of ~10–20 MW/m<sup>2</sup>, which is approximately 20% of the energy of a fusion reaction, steadily flows into a divertor that is one of the plasma facing components. Therefore, the development of a heat transfer promoter with high thermal efficiency as well as

high cooling performance must be an important R&D issue in order to achieve the low cost of electricity (COE) required by a commercial reactor.

As the conventional cooling techniques for the divertor, (Japan Atomic Energy Research Institute (JAERI) [presently Japan Atomic Energy Agency (JAEA)] has developed special heat transfer promoters that are swirl tubes and screw tubes, and succeeded in the heat removal of over 50 MW/m<sup>2</sup> (Araki et al., 1996; Ezato et al., 2006). On the other hand, since these cooling techniques are put together in high-pressure, high-velocity, high-subcooled conditions, there are still some economical issues that need to be settled in the development of a commercial

### NOMENCLATURE

<p><math>c</math> specific heat [J/kg K]  <math>d_p</math> particle diameter [m]  <math>D(s)</math> diffusion coefficient by capillarity [<math>\text{m}^2/\text{s}</math>]  <math>f(s)</math> hindrance function  <math>g</math> gravity [<math>\text{m}/\text{s}^2</math>]  <math>h</math> enthalpy [J/kg]  <math>h_{ave}</math> average heat transfer coefficient [<math>\text{W}/\text{m}^2\text{K}</math>]  <math>h_L</math> local heat transfer coefficient [<math>\text{W}/\text{m}^2\text{K}</math>]  <math>h_{fg}</math> latent heat of vaporization [J/kg]  <math>H</math> volumetric enthalpy [<math>\text{J}/\text{m}^3</math>]  <math>k</math> thermal conductivity [<math>\text{W}/\text{m K}</math>]  <math>k_r</math> relative permeability  <math>K</math> absolute permeability [<math>\text{m}^2</math>]  <math>L</math> nozzle-target distance [m]  <math>l_Z</math> length of porous medium [m]  <math>p</math> pressure [Pa]  <math>q_{in}</math> heat flux input [<math>\text{W}/\text{m}^2</math>]  <math>Re</math> Reynolds number  <math>s</math> liquid saturation  <math>T</math> temperature [K]  <math>u_{in}</math> inlet velocity [m/s]  <math>u</math> mixture velocity vector [m/s]</p> <p><b>Greek Symbols</b>  <math>\beta</math> coefficient of cubical expansion</p>	<p><math>\gamma_h</math> advection correction coefficient  <math>\Gamma_h</math> effective diffusion coefficient [<math>\text{m}^2/\text{s}</math>]  <math>\varepsilon</math> porosity  <math>\lambda</math> relative mobility  <math>\mu</math> viscosity [Pa s]  <math>\nu</math> kinematic viscosity [<math>\text{m}^2/\text{s}</math>]  <math>\rho</math> density [<math>\text{kg}/\text{m}^3</math>]  <math>\Omega</math> effective heat capacitance ratio</p> <p><b>Subscripts</b>  <math>c</math> capillary  <math>eff</math> effective  <math>f</math> fluid phase  <math>gap</math> gap  <math>l</math> liquid phase  <math>R</math> <math>R</math> direction  <math>s</math> solid phase  <math>sat</math> saturated state  <math>st</math> static state  <math>v</math> vapor phase  <math>w</math> wall  <math>Z</math> <math>Z</math> direction  <math>\kappa</math> kinetic</p>
--	---

reactor, such as an increase in thermal efficiency, an decrease in flow velocity that eases maintenance activity of piping system and contributes to lower pumping power, and compactification.

To cope with these difficulties, authors have developed a heat removal device, the evaporated fluid porous thermodevice (EVAPORON) (Toda and Yuki, 2000; Yuki et al., 2005; Togashi et al., 2005), which utilizes metal porous media and enables the multiplied effects of increased heat transfer surface (fin effect) and latent heat transport (heat pipe effect). Figure 1 shows the concept of EVAPORON, where a metal porous medium is attached onto the back side of a high heat-loading surface, removing the heat by vaporizing the coolant that flows into the porous medium counter to the heat flow. In that sense, this device has the following features and advantages.

1. High heat removal performance under low pumping power leads to excellent COE.
2. Active vaporization in the porous medium enables

high thermal efficiency due to the direct acquisition of high-temperature steam

3. Flow-accelerated corrosion (FAC) and flow-induced vibration (FIV) in piping systems, which have become a problem recently in nuclear power plants, can be dramatically reduced by low flow velocity operation.

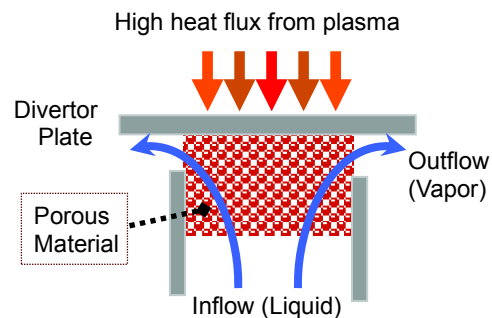


**FIG. 1:** Heat removal system by EVAPORON

Until now, heat transfer performance for sintered compacts made by bronze particle, stainless steel particle, and copper fiber has been evaluated using a plasma arc jet as a high heat-flux source. The following facts have been clarified (Yuki et al., 2005):

- (1) Heat removal performance exceeding the local heat input of  $50 \text{ MW/m}^2$  under low flow rate conditions. (Caution: the removal heat flux is not  $50 \text{ MW/m}^2$ , lower than  $10 \text{ MW/m}^2$ .)
- (2) Stable heat removal, even under a wall temperature of over  $300^\circ\text{C}$ .
- (3) Achievement of an evaporation rate of approximately 10%

These findings prove that there is a viable case for mounting EVAPORON on the divertor at the current stage. However, it is necessary to evaluate the effect of porous structures such as pore size, porosity, and some other cooling parameters on the boiling heat transfer characteristics and to figure out the formation of the two-phase region in the porous media in order to optimize the cooling conditions beyond  $10 \text{ MW/m}^2$ .

In this study, bronze particle-sintered compacts and stainless steel particle-sintered compacts are chosen from various metal porous media and focused on again to evaluate the detailed heat transfer characteristics, especially the effects of flow velocity, heat flux input, thermal conductivity, and porous structures on the heat transfer coefficient and wall temperature characteristics. These systematic experiments could clarify the key issues to enable high heat flux removal exceeding  $10 \text{ MW/m}^2$ . In addition, the two-phase flow characteristics in the porous media are evaluated by numerical simulation using the two-phase mixture model (Wang, 1997; Wang and Beckerman, 1993, 1994) in order to numerically visualize the formation of the two-phase region and meet the guidelines for the optimization of the cooling system.

## 2. EXPERIMENTAL INVESTIGATIONS ON HEAT REMOVAL CHARACTERISTICS OF PARTICLE-SINTERED POROUS MEDIA

### 2.1 Experimental Apparatus and Test Section

The experimental apparatus, which is shown in Fig. 2, is composed of a test section having a tested EVAPORON fabricated from a metal porous medium, a coolant-supplying section with a circulating pump and a storage tank, and a heating source unit using a plasma arc jet to

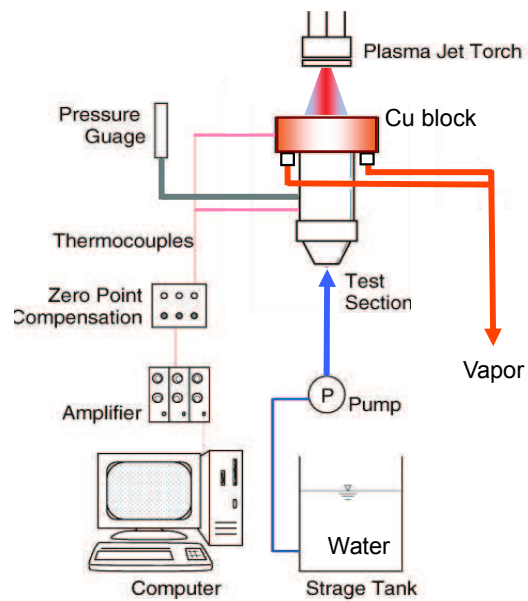


FIG. 2: Experimental apparatus

provide high heat-flux input onto the heat transfer block of the test section. The plasma nozzle shoots out a high-temperature nontransfer type plasma arc jet of an ionized hydrogen-nitrogen-argon mixture gas. In the present experiment, a discharged electric current is fixed at 300 A and the voltage is almost 150 V.

Figure 3 shows a schematic view of the test section. The test section is composed of an irradiated target and

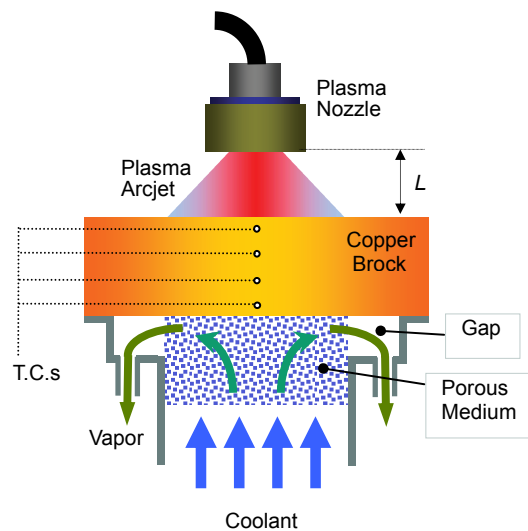


FIG. 3: Schematic view of the test section

a stainless steel flow channel in which a porous medium is inserted. The irradiated target is a copper block with a diameter of 120 mm and a thickness of 12.5 mm, whose side is insulated by a thick layer of heat-proof cement. The flow channel is a stainless circular pipe of 90 mm in length and 50 mm in inner diameter, and its top is welded to a flange that is fixed tightly onto the back side of the copper block. The flange has six pipes of 8 mm in inner diameter, which are exits to guide the two-phase evaporated fluid from the porous medium through the gap that is a narrow space between the flange and the copper block. The gap width is set to be 4 mm. The flow channel also has a branch tube for measuring the inlet pressure of the fluid with a pressure gauge.

Temperatures in the copper block are measured with four sheathed K-thermocouples of 1.0 mm in diameter with the error of  $\pm 0.75\%$ , which are inserted on the central axis of the block at intervals of 2.5 mm. Temperatures of the inlet and outlet fluids are measured with thermocouples of 0.5 mm in diameter at 20 mm upstream from the porous medium and in the middle of the gap.

## 2.2 Experimented Elements of the Porous Media

The porous media introduced in this experiment are a sintered compact composed of microsized metal particles. The shape of the porous media is cylindrical with a diameter of 50 mm and a height of 20 mm. Two kinds of metal particles are selected; one is stainless steel (SUS316L), with a corrosion resistance to high-temperature steam, and another is bronze (Cu90-Sn10), with a high thermal conductivity. Five kinds of porous elements with different pore sizes and porosities are tested, as shown in Table 1. The parameters characterizing the particle-based porous media are pore size and porosity. The pore sizes are 20, 60, and 100  $\mu\text{m}$  for the bronze particle-sintered porous media and 15 and 25  $\mu\text{m}$  for the stainless particle-sintered porous media. The porosity does not vary as much as the pore size; around 0.37 and around 0.45 for the bronze and stainless porous media, respectively. The structure is almost homogeneous and similar to closest packing.

## 2.3 Experimental Procedures

First, the coolant water flows into the bottom of the porous medium at a constant inlet pressure from the storage tank kept at a temperature of around  $12^\circ\text{C}$ . Then, the plasma arc jet is irradiated onto the copper block. The distance  $L$  between the plasma nozzle and the copper block is varied at 12, 8.0, and 5.0 cm, according to an intended

heat flux input by referring to the data obtained in the preliminary experiment (Yuki et al., 2005). The inlet velocity of water  $u_{\text{in}}$  flowing into the porous medium is varied by regulating the inlet pressure with the flow control and bypass valves and measured with a turbine flowmeter. The coolant heated in the porous medium flows out through the gap at the upper side of the porous medium. After a steady state is attained, the temperature data in the copper block and the inlet and outlet temperatures of the coolant are measured for 30 s. The incident heat flux from the plasma and the removal heat flux are estimated from the temperature profile on the central axis of the copper block. The profile is determined by the method of least squares, assuming an exponential form as the function. The bottom wall temperature of the copper block  $T_w$  is also extrapolated by the predicted temperature profile. The removal heat flux  $q_{\text{rmv}}$  is estimated using Fourier's law, and the heat transfer coefficient is defined as  $h_L = q_{\text{rmv}}/(T_w - T_{\text{in}})$ . Here,  $T_{\text{in}}$  is the inlet temperature of the water.

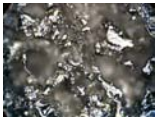

## 3. EXPERIMENTAL RESULTS AND DISCUSSION

Figure 4 shows the heat transfer coefficients and the wall temperatures at the nozzle-target distance of 12, 8.0, and 5.0 cm. Although the heat transfer coefficient is locally estimated at a stagnation point, it reflects the heat transfer characteristics by the convective and boiling heat transfers in the porous medium. Here, the characteristics of the removal heat flux itself are not discussed, since the heat input from the plasma fluctuates slightly during experiments.

To begin with, the heat transfer characteristics of EVAPORON at the nozzle-target distance of 12 cm are discussed. In this case, the heat flux input from the plasma is  $4.5\text{--}5.0\text{ MW/m}^2$ , and the removal heat flux is  $\sim 1.5\text{--}1.7\text{ MW/m}^2$ . Under the equal flow velocity conditions, the tendency that the heat transfer coefficient increases with the decrease in the pore size can be confirmed for all the porous media. As a primary cause, it is mentioned that the liquid is more easily supplied to the two-phase region by the capillary effect in the finer porous media. Also, as the second cause, the finer porous medium not only has a wider heat transfer surface, but also a higher local flow velocity due to its lower porosity, so that it seems to promote convective heat transfer in the porous medium. Especially for all the bronze porous media, the heat transfer coefficient is almost proportional to the flow velocity under higher flow velocity conditions. In addition, since the lowest wall tempera-



**TABLE: 1** Porous characteristics and structures

Characteristics	SUS316		Bronze		
	Porosity [vol. %]	44	47	35	37
Average pore diameter [μm]	15	25	20	60	100
Average particle diameter [μm]	160	500	100	300	500
Thermal Conductivity (base) [W/mK]	21		53		
Porous structure					

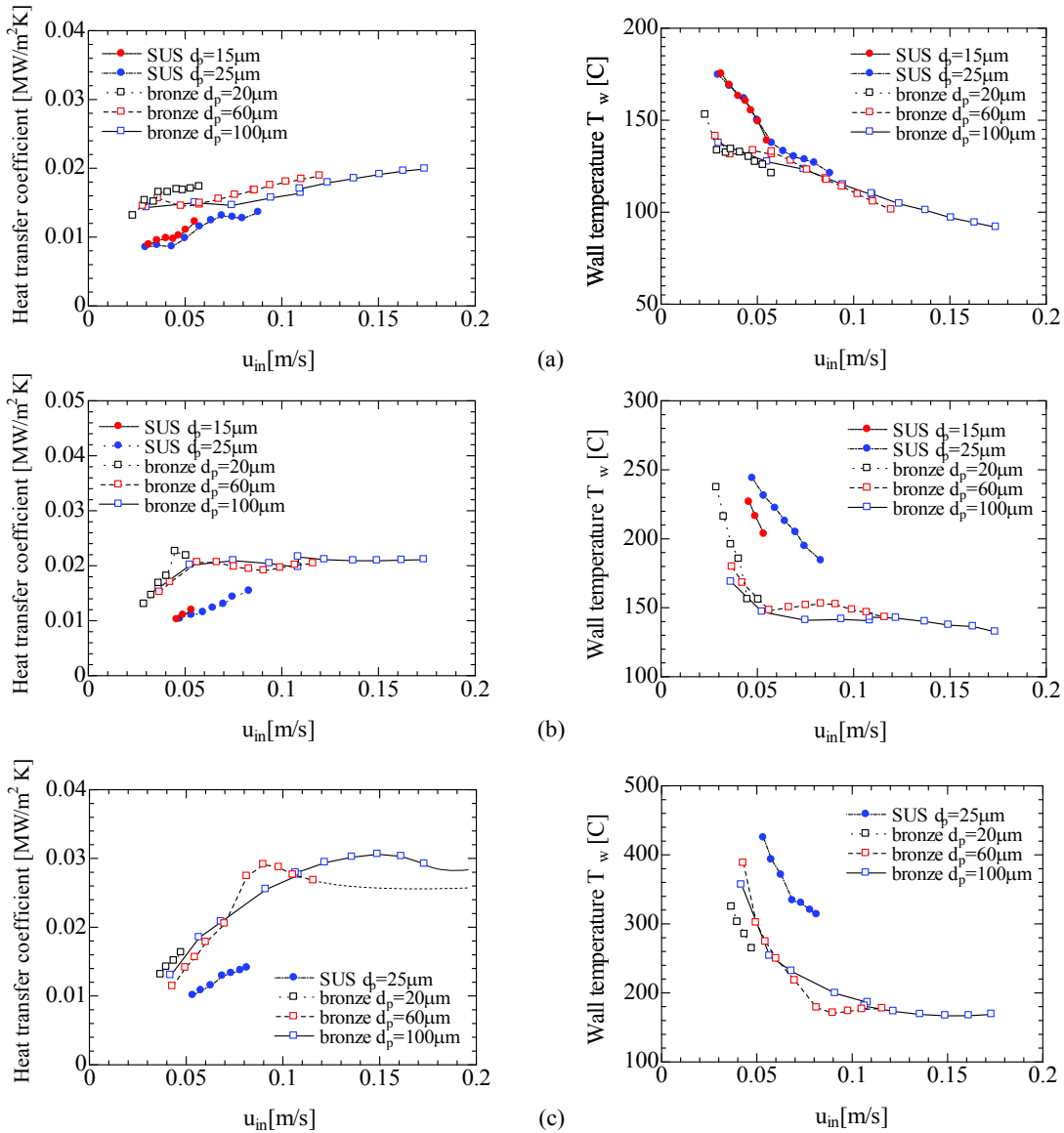


**FIG. 4:** Characteristics of heat transfer coefficient and wall temperature (nozzle-target distance **a)**  $L = 12$  cm; **b)**  $L = 8$  cm; **c)**  $L = 5$  cm)

ture is around 100°C except for the case of  $d_p = 20 \mu\text{m}$ , the convective heat transfer is still more dominant than the heat transport by the phase change. In the meantime, it can also be confirmed that there is a region where the heat transfer coefficient is not dependent on the flow velocity under lower velocity conditions. In this region, since the wall temperature is sufficiently higher than the saturation temperature of water, the phase change inside the porous medium becomes more active. On the other hand, the heat transfer coefficients of the stainless steel porous media are lower than those of the bronze porous media. The effective thermal conductivity of the stainless steel porous media is much lower than that of the bronze porous media because the stainless steel porous media have higher porosity, lower thermal conductivity as the base and material. Since the wall temperature rapidly rises as the flow velocity decreases, there is a possibility that the vapor phase formed in the stagnation area excessively develops and works as a thermal resistance layer.

Next, the heat transfer characteristics at the nozzle-target distance of 8.0 cm are discussed. In this case, the incident heat flux is  $\sim 8.9\text{--}11.0 \text{ MW/m}^2$ , and the removal heat flux is  $\sim 2.4\text{--}2.7 \text{ MW/m}^2$ . As for the bronze porous media, there exists a stable cooling state where the heat transfer coefficients do not change in the wide flow velocity range, which corresponds to the fully developed nucleate boiling regime of the boiling curve. This means that the latent heat transport accompanying the phase change becomes more active in this heat flux level because the heat transfer coefficient itself is higher than that in the  $L = 12 \text{ cm}$  case. However, the heat transfer coefficients show almost equivalent values regardless of the pore sizes. From the wall temperature characteristics, when the wall temperature exceeds about 150°C, the wall temperature rapidly rises and then the heat transfer performance is degraded with the lowering of the flow velocity, which suggests that the wetting limit temperature determined by combination of the bronze and water in this cooling system could be around 150°C and that the minimum liquid saturation in the two-phase region reach zero under temperatures higher than this limiting temperature. As for the stainless steel porous media, the heat transfer coefficients are much lower than those of the bronze media as well as the case of  $L = 12 \text{ cm}$ . That is, it is considered that the vapor phase excessively develops and inhibits the liquid-vapor exchange near the heating surface because the wall temperature, which is over 180°C, is much higher than the wetting limit temperature. This results in the sharp drop of the

heat transfer coefficient with the decrease in the flow velocity.

Finally, the case of the nozzle-target distance of 5 cm is discussed. At this distance, the incident heat flux is  $\sim 18.4\text{--}23.6 \text{ MW/m}^2$ , and the removal heat flux is  $\sim 4.1\text{--}4.6 \text{ MW/m}^2$ . Since the heat removal was impossible for the stainless steel porous medium of 15  $\mu\text{m}$  pore size, it is not reported. Also for the stainless steel porous medium of 25  $\mu\text{m}$  pore size, the wall temperature exceeds 300°C, which indicates excessive development of the vapor phase in which the completely dry area expands with decreasing the flow velocity. However, it can be said that one of the important advantages of using porous media for the heat removal is that it does not reach the heat removal limit, even under such high wall temperature conditions, which proves that EVAPORON cooling easily enables a stable cooling even in the film boiling-like regime. In that sense, the heat removal limit is determined by the allowable temperature of the heat sink material used. On the other hand, in this heat flux level, the wall-temperature on using the bronze porous media sharply rises from around 170°C, which could be over the wetting limit temperature. This value is a little higher than that in the  $L = 12 \text{ cm}$  case due to a thermal resistance between the porous medium and the copper block. Under the wide flow velocity conditions, the heat transfer coefficients lower with the decrease of the flow velocity, but the region where the flow velocity does not affect the heat transfer coefficient seems to appear under higher flow velocity conditions, especially for the porous media with pore sizes of 60  $\mu\text{m}$  and 100  $\mu\text{m}$ . Taking into account this prediction, the heat transfer coefficient seems to become higher in the larger-pore case. This is a fact worthy of mention in that the dependency of the heat transfer performance on the pore size reverses as the heat flux increases before achieving a heat removal rate of 10  $\text{MW/m}^2$ . As the vapor phase becomes easier to develop under higher heat flux, it can be assumed that the discharge performance of the vapor, that is to say, permeability, is more of a factor than the heat transport by the capillarity and the fin effect because the discharge performance of the vapor is contradictory to the capillarity effect in connection with the pore size. It is therefore considered that the heat transfer performance of the porous material with the larger pore size tends to become higher under much higher heat flux conditions.

Figure 5 shows the heat transfer characteristics of the bronze porous medium of 100  $\mu\text{m}$  in pore size at each heat flux input. From this figure, it is obvious that the stabilized cooling state appears under higher velocity conditions with the increase of heat flux input. Summariz-

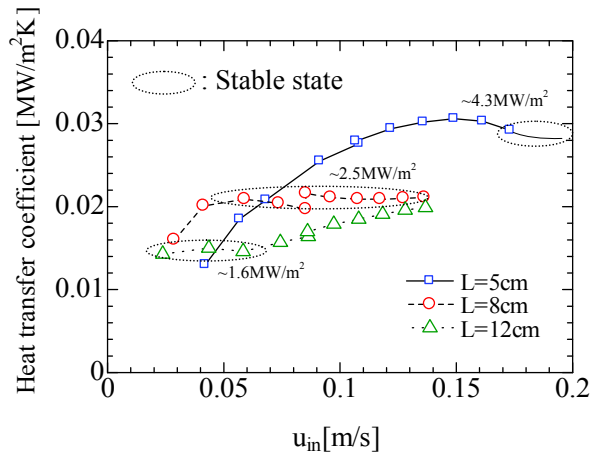


FIG. 5: Effect of heat flux level on heat transfer

ing the findings from the experiments, the utilization of higher permeability and higher effective thermal conductivity porous media is needed under much higher-velocity conditions in order to enable a heat flux removal rate exceeding  $10.0\text{MW/m}^2$ . In particular, spherical particle-based porous media such as the bronze porous media used generally have higher permeability than those of the other porous media, even with the same scale structure in spite of its low porosity structure [see Fig. 6, which includes the permeabilities of fiber-sintered porous media (Yuki et al., 2005)], which leads to high discharge performance of the vapor without losing the capillary effect as well as with keeping high effective thermal conductivity (i.e., lower porosity leads to higher thermal conductivity). In the following numerical calculation, the two-phase flow

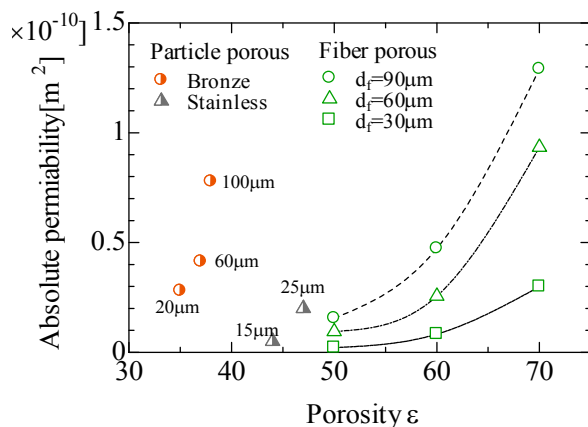


FIG. 6: Permeability for various porous media characteristics (bronze : pore size  $100\ \mu\text{m}$ )

characteristics in the porous media are discussed to clarify the detailed effect of the thermal conductivity.

#### 4. NUMERICAL SIMULATION OF PHASE-CHANGE CHARACTERISTICS IN POROUS MEDIA

##### 4.1 Calculation System

The present simulation focuses on what kind of porous material is more suitable for removing heat flux exceeding  $10\text{MW/m}^2$ . The computational domain and the coordinate system ( $R, Z$ ) shown in Fig. 7 are almost the same as the present experiment. It is assumed that the porous medium is homogeneous and isotropic, so that the analysis is two-dimensionally performed under axially symmetrical and steady conditions. The height of the channel is  $l_z$ , the radius is  $l_R$ , and gap width of the outlet is  $l_g$ . In this calculation, the porosity and the particle diameter are fixed at 0.44 and  $160\ \mu\text{m}$ , respectively. Three kinds of porous material are introduced, which are stainless steel, iron, and copper porous media whose thermal conductivities are 20.15, 72.00, and 395.0, respectively.

##### 4.2 Governing Equations and Constitutive Equations

The present simulation focuses on porous media composed of microsized metal particles. Since the flow velocity in the porous medium is not fast (laminar regime), Darcy's law can be applied to the liquid and vapor phases. In that sense, the two-phase mixture model developed by Wang (1997) and Wang and Beckerman (1993, 1994) is introduced to simulate the two-phase flow characteristics. In their model, since heat transfer between the fluid phase

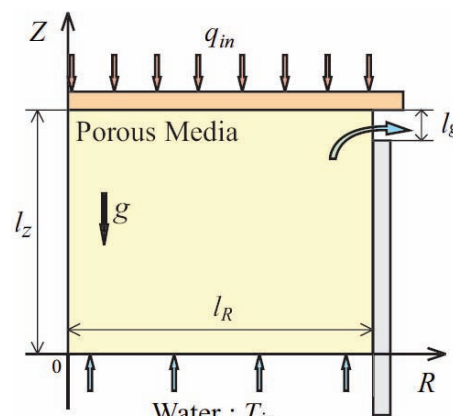


FIG. 7: Computational domain

and the solid phase is based on local thermal equilibrium, both temperatures in the two-phase region are at the saturated temperature  $T_{\text{sat}}$ . All the governing equations and the mixture variables are completely the same as their formulation. In general, the influence of the thermal nonequilibrium between the solid phase and the fluid phase is not negligible, especially in the two-phase region (Yuki et al., 2008). However, it is reasonable to apply the local equilibrium model in order to qualitatively evaluate the influence of the thermal conductivity of the porous medium.

The governing equations using the two-phase mixture model can be written as follows.

Continuity

$$\varepsilon \frac{\partial \rho}{\partial t} + \nabla \cdot (\rho \mathbf{u}) = 0 \quad (1)$$

Momentum equation

$$\mathbf{u} = -\frac{K}{\mu(s)} [\nabla p - \rho_{\kappa}(s) \mathbf{u}] \quad (2)$$

Energy Conservation

$$\begin{aligned} \Omega \frac{\partial H}{\partial t} + \nabla \cdot (\gamma_{\text{h}} \mathbf{u} H) &= \nabla \cdot (\Gamma_{\text{h}} \nabla H) \\ + \nabla \cdot \left[ f(s) \frac{K \Delta \rho h_{\text{fg}}}{\nu_{\text{v}}} g \right] & \end{aligned} \quad (3)$$

where the mixture variables and some major coefficients are defined below.

Density and velocity

$$\rho = \rho_{\text{l}} s + \rho_{\text{v}} (1 - s) \quad (4)$$

$$\rho \mathbf{u} = \rho_{\text{l}} \mathbf{u}_{\text{l}} + \rho_{\text{v}} \mathbf{u}_{\text{v}} \quad (5)$$

Enthalpy

$$H = \rho(h - 2h_{\text{vsat}}) \text{ with } \rho h = \rho_{\text{l}} s h_{\text{l}} + \rho_{\text{v}} (1 - s) h_{\text{v}} \quad (6)$$

Kinetic Density

$$\begin{aligned} \rho_{\kappa} &= \rho_{\text{l}} [1 - \beta_{\text{l}}(T - T_{\text{sat}})] \lambda_{\text{l}}(s) \\ + \rho_{\text{v}} [1 - \beta_{\text{v}}(T - T_{\text{sat}})] \lambda_{\text{v}}(s) & \end{aligned} \quad (7)$$

Viscosity

$$\mu = \frac{\rho_{\text{l}} s + \rho_{\text{v}} (1 - s)}{(k_{\text{rl}}/\nu_{\text{l}}) + (k_{\text{rv}}/\nu_{\text{v}})} \quad (8)$$

Advection Correction Coefficient

$$\gamma_{\text{h}} = \frac{[(\rho_{\text{v}}/\rho_{\text{l}})(1 - s) + s][h_{\text{vsat}}(1 + \lambda_{\text{l}}) - h_{\text{lsat}}\lambda_{\text{l}}]}{(2h_{\text{vsat}} - h_{\text{lsat}})s + (\rho_{\text{v}}h_{\text{vsat}}/\rho_{\text{l}})(1 - s)} \quad (9)$$

Effective Heat Capacitance Ratio

$$\Omega = \varepsilon + \rho_{\text{s}} c_{\text{s}} (1 - \varepsilon) \frac{dT}{dH} \quad (10)$$

Effective Diffusion Coefficient

$$\Gamma_{\text{h}} = \frac{1}{1 + (1 - \rho_{\text{v}}/\rho_{\text{l}})h_{\text{vsat}}/h_{\text{fg}}} D(s) + k_{\text{eff}} \frac{dT}{dH} \quad (11)$$

Relative Mobility

$$\begin{aligned} \lambda_{\text{l}}(s) &= \frac{k_{\text{rl}}/\nu_{\text{l}}}{(k_{\text{rl}}/\nu_{\text{l}}) + (k_{\text{rv}}/\nu_{\text{v}})} \\ \lambda_{\text{v}}(s) &= \frac{k_{\text{rv}}/\nu_{\text{v}}}{(k_{\text{rl}}/\nu_{\text{l}}) + (k_{\text{rv}}/\nu_{\text{v}})} \end{aligned} \quad (12)$$

Capillary diffusion coefficient

$$D(s) = \frac{K}{\mu_{\text{l}}} \frac{k_{\text{rl}} k_{\text{rv}}}{(\nu_{\text{v}}/\nu_{\text{l}})k_{\text{rl}} + k_{\text{rv}}} \left[ -\frac{\partial p_{\text{c}}(s)}{\partial s} \right] \quad (13)$$

Hindrance Function

$$f(s) = \frac{k_{\text{rl}} k_{\text{rv}}/\nu_{\text{l}}}{(k_{\text{rl}}/\nu_{\text{l}}) + (k_{\text{rv}}/\nu_{\text{v}})} \quad (14)$$

The temperature of the fluid phase and the liquid saturation are estimated by the volumetric enthalpy  $H$  in Eq. (3).

To complete the above-mentioned governing equations, the constitutive equations need to be decided. It is difficult, however, to generalize them because various correlations have been proposed according to the porous structure and the cooling system. The selection in this study should be based on the fact that the spherical particle-sintered porous media are also going to be evaluated in the future.

Permeability  $K$  can be estimated as a function of porosity  $\varepsilon$ , and particle diameter  $d_{\text{p}}$  by the Carman and Kozney correlation (Nield and Bejan, 1992) as

$$K = \frac{\varepsilon^3 d_{\text{p}}^2}{180(1 - \varepsilon)^2} \quad (15)$$

Relative permeability for each phase  $k_{\text{r}}$  is simply given as a linear function of the liquid saturation  $s$  (Udell, 1985) as

$$k_{\text{rl}} = s, \quad k_{\text{rv}} = (1 - s) \quad (16)$$

Capillary pressure  $p_{\text{c}}(s)$  is represented by Udell (1985) as

$$\begin{aligned} p_{\text{c}}(s) &= \sqrt{\frac{\varepsilon}{K}} \sigma [1.417(1 - s) - 2.120(1 - s)^2 \\ + 1.263(1 - s)^3] & \end{aligned} \quad (17)$$

Effective thermal conductivity  $k_{\text{eff}}$  is estimated by using the correlation by Yagi and Kunii (1957, 1960),

$$\frac{k_{\text{eff}}}{k_f} = \frac{k_{\text{st}}}{k_f} + 0.4 \left( \frac{d_p |u|}{\nu} \right) \left( \frac{c_{pf} \mu}{k_f} \right) \quad (18)$$

where  $k_{\text{st}}$  is the thermal conductivity in case that a porous medium is in a static state, and  $k_f$  is that of working fluid,

$$k_{\text{st}} = k_s(1 - \varepsilon) + k_l \varepsilon s + k_v \varepsilon(1 - s) \quad (19)$$

$$k_f = k_l s + k_v(1 - s) \quad (20)$$

### 4.3 Numerical Conditions and Procedures

Although the present study aims to evaluate the influence of the thermal conductivity of porous material, the inlet velocity  $u_{\text{in}}$  and heat flux input  $q_{\text{in}}$  are also chosen as significant parameters in order to figure out general two-phase flow characteristics in the porous media. The boundary conditions of this calculation are listed as follows.

At inlet ( $Z = 0$ )

$$\begin{aligned} u &= u_{\text{in}} \\ v &= 0 \\ H_{\text{in}} &= \rho_l(h_{\text{in}} - 2h_{\text{vsat}}) \end{aligned} \quad (21)$$

At heating surface ( $Z = l_Z$ )

$$-\Gamma_h \frac{\partial H}{\partial Z} = q_{\text{in}} \quad (22)$$

At center axis ( $R = 0$ )

$$\frac{\partial u}{\partial R} = v = \frac{\partial p}{\partial R} = \frac{\partial H}{\partial R} = 0 \quad (23)$$

At sidewall ( $R = l_R$ )

$$\begin{aligned} \frac{\partial H}{\partial R} &= 0 (0 < Z < l_Z - l_g) \\ p &= 1 \text{ atm} (l_Z - l_g < Z < l_Z) \end{aligned} \quad (24)$$

The governing equations are discretized by the finite volume method and solved by the SIMPLE algorithm (Patankar, 1980). The computational domain is divided into equal grid spacing in the  $R$  direction and inhomogeneous grid spacing in the  $Z$  direction, where finer mesh is used near the heating wall.

### 4.4 Numerical Results and Discussion

*General phase-change characteristics:* Figures 8a–8c show the effects of the inlet velocity on the temperature, liquid saturation, and pressure distributions in the stainless steel porous medium. The heat flux input  $q_{\text{in}}$  is  $0.28 \text{ MW/m}^2$  and the inlet velocities are  $2.5 \times 10^{-3}$ ,  $3.0 \times 10^{-3}$ , and  $3.5 \times 10^{-3} \text{ m/s}$ , respectively. These figures suggest general features in this cooling system. The velocity vectors for the liquid and the vapor are also drawn in Figs. 8a and 8b. Acceleration of the liquid velocity near the outlet, as shown in Fig. 8a, enhances the heat transfer and lowers the temperature rise of the heating wall near the outlet. Since vapor occurring near the stagnation region is diffused by the capillarity, the vectors of vapor velocity shown in Fig. 8b point from the heating wall toward the liquid phase, which can transport the latent heat of evaporation to the liquid. For this reason, the heat transport by latent heat as well as by sensible heat plays an important roll in this system. The penetration depth of the heat transport toward the entrance becomes shallower as the inlet velocity increases. In addition, the two-phase region becomes narrower, and the minimum value of liquid saturation becomes higher. One reason for this is that the increase in inlet velocity, i.e., the increase in inlet pressure, inhibits the growth of the two-phase region. Needless to say, heat transfer enhancement through an increase in the inlet flow velocity strongly affects the temperature and liquid saturation distributions. Figures 9a and 9b show the temperature and liquid saturation distributions for the stainless steel porous medium at the inlet heat fluxes of  $0.26$ ,  $0.28$ , and  $0.30 \text{ MW/m}^2$ . The inlet velocity is fixed at  $u_{\text{in}} = 3.0 \times 10^{-3} \text{ m/s}$ . The depth of the heat penetration becomes deeper and the two-phase region expands as the heat flux increases in order to remove higher heat flux input. Furthermore, each spacing between the  $330 \text{ K}$  and  $360 \text{ K}$  contour lines shown in Fig. 9a do not change excessively, regardless of the heat flux input. This results from active phase-change heat transfer, which leads to the stable heat transfer performance mentioned in the last section. It is obvious that the minimum liquid saturation decreases with an increase in the heat flux input. The thermal insulation effect brought on by the two-phase region mentioned before seems to appear when the dry area (zero liquid saturation) is formed in the two-phase region.

*Effect of thermal conductivity:* Figure 10 shows the temperature distributions in the stainless steel, iron, and copper porous media under the same conditions at  $u_{\text{in}} = 3.0 \times 10^{-3} \text{ m/s}$  and  $q_{\text{in}} = 0.28 \text{ MW/m}^2$ . The phase

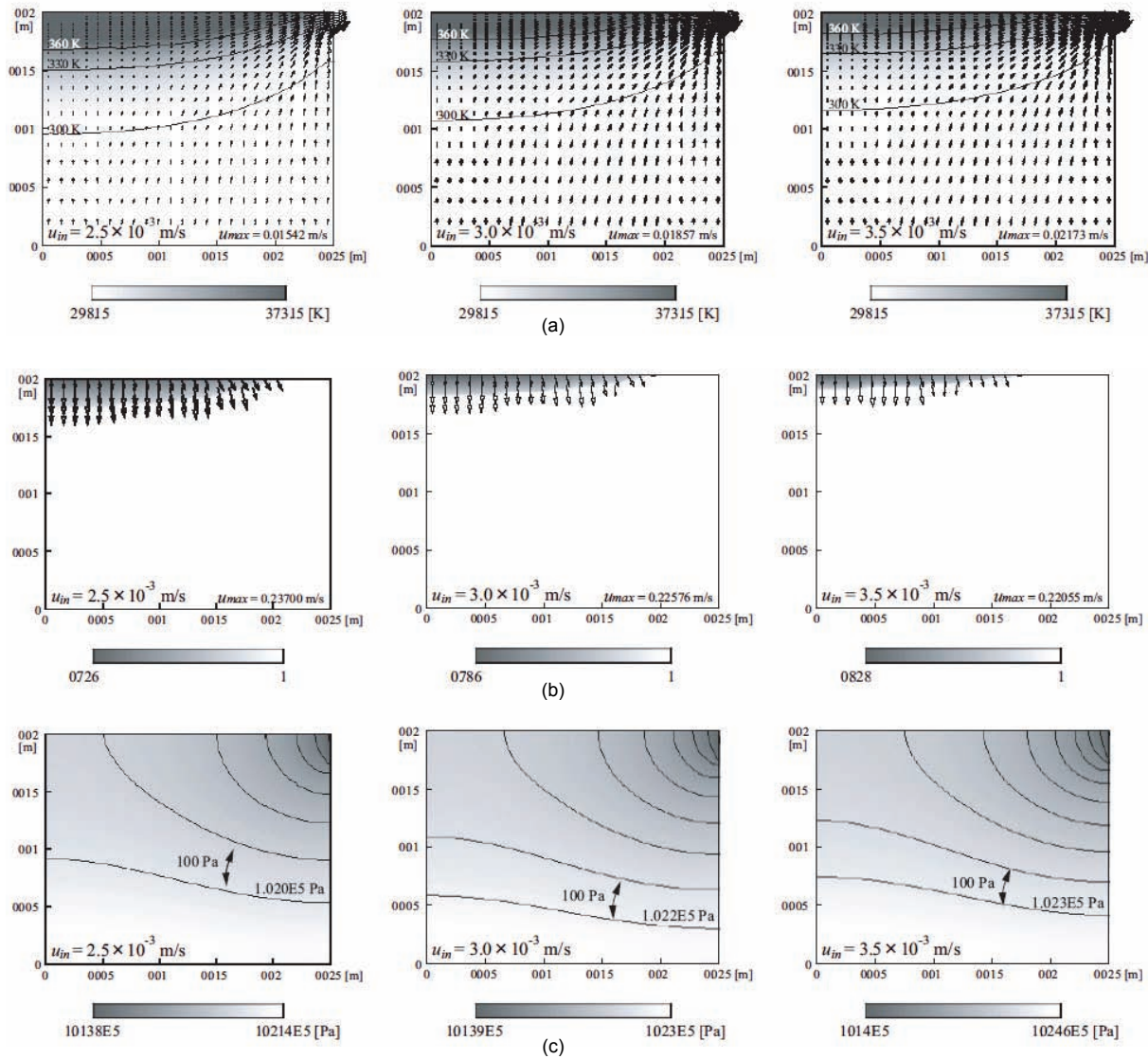


**FIG. 8:** Effect of inlet velocity on two-phase flow characteristics for stainless steel porous medium: **a)** temperature distribution; **b)** liquid saturation distribution; **c)** pressure distribution

change occurs only in the case of the stainless steel porous medium. As for the iron and copper media, higher thermal conductivity in comparison with the stainless steel makes it possible to transport the input heat further inside of the porous medium, where most heat exchange is conducted by sensible heat transport. On the other hand, the temperature gradient near the heating wall on using the stainless porous medium is extremely steep due to its low thermal conductivity, making it easier to reach saturation temperature. Figure 11 shows the av-

erage heat transfer coefficient  $h_{ave}$ , which is calculated by averaging the local heat transfer coefficient  $h_L = q_{in}/(T(l_Z, R) - T_{in})$ , versus the particle Reynolds number  $Re_p = d_P u_{in}/\nu$  at  $q_{in} = 0.28 \text{ MW/m}^2$ . Enhancement of the heat transfer due to an increase in the flow velocity is confirmed for all the porous media, especially for the higher-thermal conductivity material. Enhancement by vaporization only plays a major role in the case of the stainless steel porous medium, so that the enhancement by an increase of  $Re_p$  is minute. Figure 12 shows

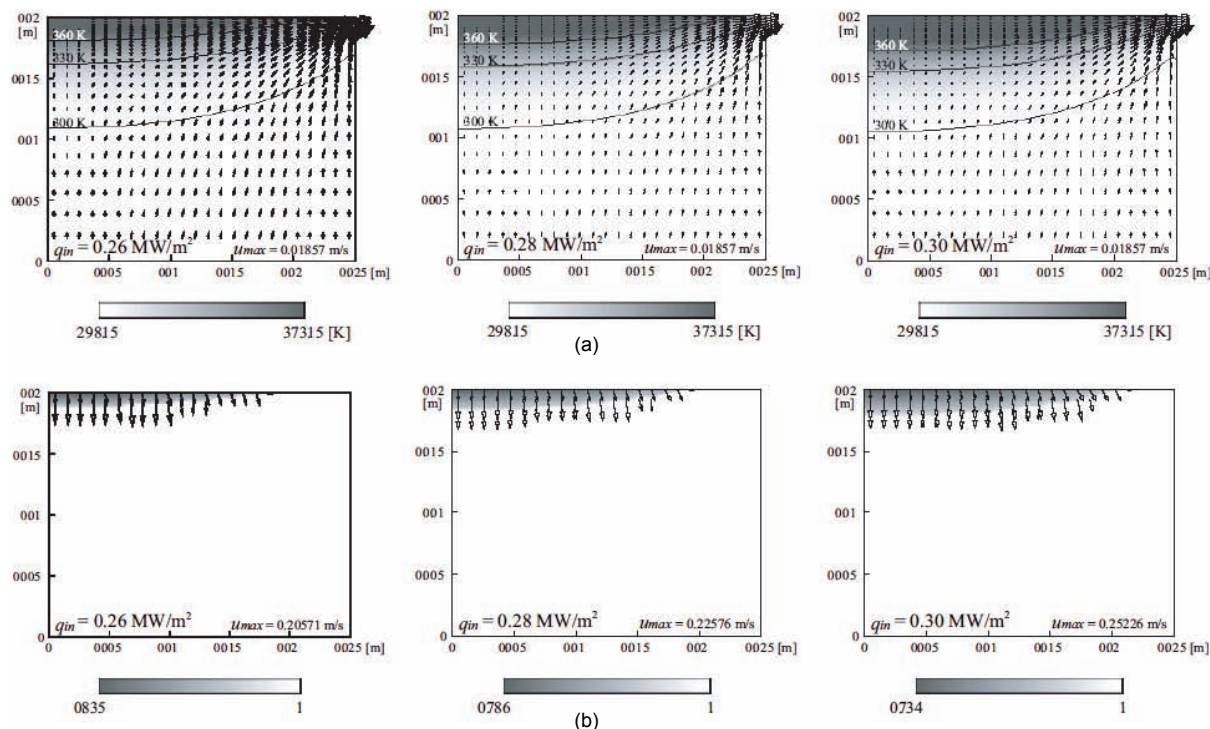


**FIG. 9:** Effect of heat flux input on two-phase flow characteristics for stainless steel porous medium: **a)** temperature distributions; **b)** liquid saturation distribution

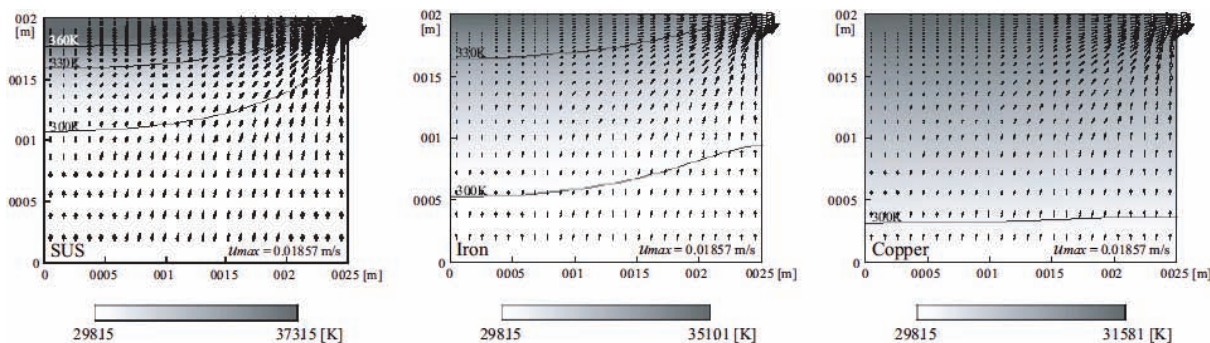


**FIG. 10:** Temperature distributions for stainless steel, iron, and copper porous media under the same conditions

the removal heat flux versus the thermal conductivity at the same liquid saturation values of  $s = 0.99, 0.85,$  and  $0.66,$  which represents the minimum in the two-phase region. In this cooling system, the critical-like heat flux could occur when the liquid saturation reaches zero and, then, the dry area with  $s = 0$  expands to a certain degree with the increase of heat flux input or the decrease of flow velocity, which contributes to the rapid rise of the wall temperature due to the decrease in effective ther-

mal conductivity in the dry area. Needless to say, this cooling limit is highly affected by the wetting limit temperature too. However, this figure indicates the significant fact that the CHF is expected to improve more when using higher-thermal conductivity material because the copper porous medium can delay the onset of the phase change on the higher heat flux side and enables much higher heat flux removal even at the same liquid saturation.

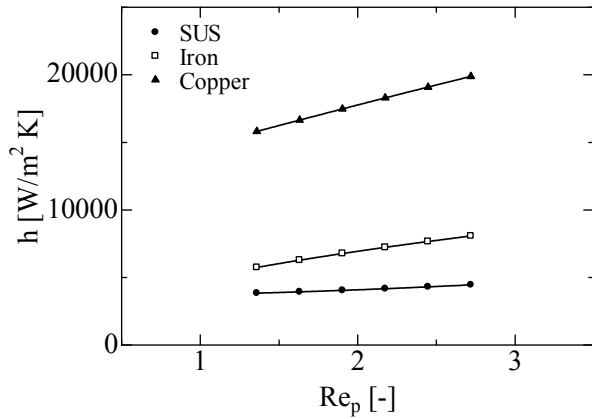


FIG. 11: Average heat transfer coefficient versus particle Reynolds number  $Re_p$

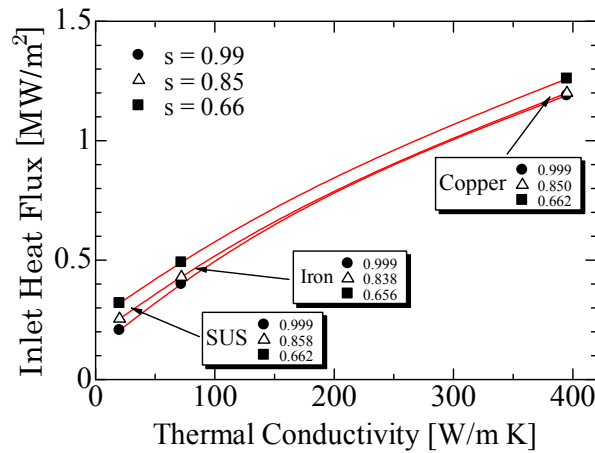


FIG. 12: Removal heat flux versus thermal conductivity of porous material

## 5. CONCLUSION

In this study, the detailed heat transfer characteristics in the stainless steel and bronze porous media, which are both particle-sintered compacts, were evaluated first, and then the two-phase flow characteristics in the porous media were simulated by the two-phase mixture model in order to clarify key issues for achieving a heat flux removal exceeding  $10 \text{ MW/m}^2$ . Our findings are summarized as follows:

1. Experiments under some heat flux inputs clarified that the heat transfer characteristics strongly depended on the level of the heat flux input.

2. The dependency of the heat transfer performance on the pore scale reverses as the heat flux increases before achieving the heat removal of  $10 \text{ MW/m}^2$  because the discharge performance of the vapor is more of a factor than the heat transport by the capillarity.
3. Spherical particle-sintered porous media could be more suitable than the other porous media for heat removal exceeding  $10 \text{ MW/m}^2$  because the spherical particle-based porous medium has high permeability in spite of its low-porosity structure.
4. Numerical results clarified the general two-phase flow features and showed that utilizing a higher thermal-conductivity matrix delay the onset of the phase change on the higher heat flux side and enabled much higher heat flux removal, even at the same liquid saturation.

## REFERENCES

- Araki, M., Ogawa, M., Kunugi, T., Ikeda, S., Satoh, K., and Suzuki, S., Experiment on heat transfer of smooth and swirl tubes under one-sided heating conditions, *Int. J. Heat Mass Transfer*, vol. 39, no. 14, pp. 3045–3055, 1996.
- Ezato, K., Suzuki, S., Dairaku, M., and Akiba, M., Experimental examination of heat removal limitation of screw cooling tube at high pressure and temperature conditions, *Fusion Eng. Des.*, vol. 81, pp. 347–354, 2006.
- Nield, D. A. and Bejan, A., *Convection in Porous Media*, Chap. 1, Springer-Verlag, New York, 1992.
- Patankar, S. V., *Numerical Heat Transfer and Fluid Flow*, McGraw-Hill, New York, 1980.
- Toda, S. and Yuki, K., A challenge to extremely high heat flux removal technique using a porous medium, *J. HTSJ*, vol. 39, no. 159, pp. 23–28, 2000 (in Japanese).
- Togashi, H., Yuki, K., and Hashizume, H., Heat transfer enhancement technique with copper fiber porous media, *Fusion Sci. Technol.*, vol. 47, no. 3, pp. 740–745, 2005.
- Udell, K. S., Heat transfer in porous media considering phase change and capillarity (The heat pipe effect), *Int. J. Heat Mass Transfer*, vol. 28, pp. 485–494, 1985.
- Wang, C. Y., A fixed-grid numerical algorithm for two-phase flow and heat transfer in porous media, *Numer. Heat Transfer, Part B*, vol. 31, pp. 85–105, 1997.
- Wang, C. Y. and Beckermann, C., A two-phase mixture model of liquid-gas flow and heat transfer in capillary porous media—I. Formulation, *Int. J. Heat Mass Transfer*, vol. 36, no. 11, pp. 2747–2758, 1993.
- Wang, C. Y., Beckermann, C., and Fan, C., Numerical study of boiling and natural convection in capillary porous media



- using the two-phase mixture model, *Numer. Heat Transfer, Part A*, vol. 26, pp. 375–398, 1994.
- Yagi, S. and Kunii, D., Studies on effective thermal conductivities in packed beds, *AIChE J.*, vol. 3, pp. 373–381, 1957.
- Yagi, S. and Kunii, D., Studies on heat transfer near wall surface in packed beds, *AIChE J.*, vol. 6, pp. 97–104, 1960.
- Yuki, K., Abei, J., Hashizume, H., and Toda, S., Numerical investigation of thermofluid flow characteristics with phase change against high heat flux in porous media, *ASME J. Heat Transfer*, vol. 130, no. 1, 012602, 2008.
- Yuki, K., Abei, J., Hashizume, H., and Toda, S., Super-high heat flux removal using sintered metal porous media, *J. Thermal Sci.*, vol. 14, no. 3, pp. 272–280, 2005.

# THERMOHYDRODYNAMIC INSTABILITY OF VISCOUS ROTATING DIELECTRIC FLUID LAYER IN POROUS MEDIUM WITH VERTICAL AC ELECTRIC FIELD

*M. F. El-Sayed*

*Department of Mathematics Faculty of Education, Ain Shams University, Heliopolis (Roxy), Cairo Egypt*

Address all correspondence to M. F. El-Sayed E-mail: mfahmye@yahoo.com

*Original Manuscript Submitted: 5/13/2009; Final Draft Received: 1/19/2010*

*The effects of uniform rotation and porous medium on the onset of convective instability in a dielectric fluid confined between two horizontal planes under the simultaneous action of a vertical ac electric field and a vertical temperature gradient is considered. Applying linear perturbation theory and approximations analogous to the usual Boussinesq approximations, an equation of tenth order is derived. Under appropriate boundary conditions, this equation is solved exactly and the eigenvalue equations for the critical electrical Rayleigh number are obtained for both the cases of exchange of stabilities and overstability, respectively. The corresponding critical wave numbers are also obtained for both cases. It is shown that the medium permeability and Rayleigh number have destabilizing effects on the considered system, where as the porosity of porous medium, Taylor number, and Prandtl number have stabilizing effects. It is found also that, at high values of Taylor number or at any value of Prandtl number, the critical electrical Rayleigh number is independent of the Rayleigh number.*

**KEY WORDS:** *hydrodynamic stability, brinkman model, convection in porous media, electrohydrodynamics*

## 1. INTRODUCTION

A temperature gradient applied to a dielectric fluid produces a gradient in the dielectric constant and electrical conductivity. The application of a dc electric field then results in the accumulation of free charge in the fluid. The free charge buildup occurs exponentially in time with a time constant  $\epsilon/\sigma$ , where  $\epsilon$  is the dielectric constant and  $\sigma$  is the electrical conductivity. This constant is known as the electrical relaxation time (Melcher, 1981). If an ac electric field is applied at a frequency much higher than the reciprocal of the electrical relaxation time, the free charge does not have time to accumulate. The electrical relaxation times of most dielectric fluids appear to be sufficiently long to make free charge effects negligible at standard power line frequencies. At the same time, dielectric loss at these frequencies is so low that it makes

no significant contribution to the temperature field. Furthermore, variations in the body force are so rapid that its mean value can be assumed as the effective value in determining fluid motions, except in the case of fluids of extremely low viscosity. Thus, the case of an ac electric field is more tractable than that of a dc electric field. The ac electric field case has been examined by Turnbull and Melcher (1969) and Turnbull (1968a,b; 1970).

The classical problem of thermal convection in a fluid layer heated from below and rotating about a vertical axis with prescribed temperatures at the boundaries has been the subject of investigation by many authors because of its unusual dynamical properties (Cebeci and Bradshaw, 1984; Nepomnyashchy et al., 2006). Among studies made in this domain, one can mention works presented in pure fluid by Chandrasekhar (1981) for the linear stability study, and by Malkus and Veronis (1958) and Kelly and

Pal (1978) for the finite amplitude. The coriolis effect on gravity-driven convection was investigated by Busse and Heikes (1980) for experimental studies, Cross and Kim (1988) for numerical simulations, and Vadasz (1998) for asymptotic studies. Among the applications in engineering disciplines, one can find the food-process industry, centrifugal casting of metals and rotating machinery.

Convective flows in porous media have been extensively studied during the last several decades and that have included several different physical effects (Weber, 1974; Nield, 1991, 1994, 1998). This interest is due to the many practical applications which can be modeled or approximated as transport phenomena in porous media (Lapwood, 1948; Hennenberg et al., 1997). These flows appear in a wide variety of industrial applications, as well as in many natural circumstances, such as geothermal extraction, storage of nuclear waste material, ground water flows, industrial and agricultural water distribution, oil recovery processes, thermal insulation engineering, pollutant dispersion in aquifers, cooling of electronic components, packed-bed reactors, food processing, casting and welding of manufacturing processes, the dispersion of chemical contaminants in various processes in the chemical industry and in the environment, soil pollution, fibrous insulation, and even for obtaining approximate solutions for flow through turbomachinery (Payne and Straughan, 1998; Clever and Busse, 2000; Siddheshwar and Srikrishna, 2001; Malashetty and Gaikwad, 2003; Tan and Masuoka, 2007). This topic is of vital importance in all these applications, thereby generating the need for a full understanding of transport processes through porous media. Theories and experiments of thermal convection in porous media and the state-of-the-art reviews, with special emphasis on practical applications, have been presented in the recent monographs of Ingham and Pop (1998), Nield and Bejan (1999), Vafai (2000), and Pop and Ingham (2001).

The aim of the present study is to theoretically examine the combined effects of rotation and a porous medium on the onset of convective instability in a viscous dielectric fluid confined between two horizontal planes under the simultaneous action of a vertical ac electric field and a vertical temperature gradient. This problem, to the best of my knowledge, has not been investigated yet. We studied here the linear stability, when both the principles of exchange of stabilities and overstability occur, for the critical electrical Rayleigh number and the corresponding critical wavenumber values, and the effects of various physical parameters on the stability analysis of the considered system.

## 2. FORMULATION OF THE PROBLEM

We consider an infinite horizontal layer of dielectric fluid of thickness  $d$ , which is kept rotating about the vertical  $z$ -axis with a constant angular velocity  $\Omega$  through a porous medium. The lower surface at  $z = 0$  and the upper surface at  $z = d$  are maintained at constant temperatures  $\theta_0$  and  $\theta_1$ , respectively. In addition to a temperature gradient, a vertical ac electric field is also imposed across the layer; the lower surface is grounded, and the upper surface is kept at an alternating potential, where the root-mean-square value is  $\phi_1$ . One can assume the gravity buoyancy to be dominant and neglect the centrifugal buoyancy, hence, limiting the effect of rotation to the Coriolis acceleration and assuming the centrifugal acceleration to be constant and absorbed in the reduced pressure term (Khiri, 2004). This assumption is usually correct when the boundary conditions of the layer are homogeneous in the horizontal dimensions. We have the Boussinesq approximation of the basic Navier-Stokes equations of motion; because all the material properties are assumed to be constant except for the density, the temperature dependence is taken into account only in the gravity term and we anticipate that there can be instability only when  $\theta_0 > \theta_1$ .

If we observe the fluid from a frame of reference that is rotating about the  $z$ -axis with the same angular velocity as the fluid, and if we neglect the centrifugal force, then the equations of motion and continuity are (Hsu and Cheng, 1985; Nazzar et al., 2003)

$$\frac{\rho}{m} \left[ \frac{\partial \mathbf{v}}{\partial t} + \frac{1}{m} (\mathbf{v} \cdot \nabla) \mathbf{v} \right] = -\nabla P + \rho \mathbf{g} + \frac{2\rho}{m} (\mathbf{v} \times \boldsymbol{\Omega}) + \frac{\mu}{m} \nabla^2 \mathbf{v} - \frac{\mu}{k_1} \mathbf{v} + \mathbf{f}_e \quad (1)$$

$$\nabla \cdot \mathbf{v} = 0 \quad (2)$$

where  $\rho$  is the mass density,  $\mu$  is the coefficient of viscosity,  $m$  is the porosity of porous medium,  $k_1$  is the medium permeability,  $P$  is the pressure,  $\mathbf{v}$  is the velocity of the liquid,  $\mathbf{g} = (0, 0, -g)$  is the gravitational acceleration,  $\boldsymbol{\Omega} = (0, 0, \Omega)$  is the angular velocity of the rotating fluid layer, and  $\mathbf{f}_e$  is the force of electrical origin, which may be expressed as (Landau and Lifshitz, 1960)

$$\mathbf{f}_e = -\frac{1}{2} (\mathbf{E} \cdot \mathbf{E}) \nabla \varepsilon + \frac{1}{2} \nabla \left[ \rho \frac{\partial \varepsilon}{\partial \rho} (\mathbf{E} \cdot \mathbf{E}) \right] \quad (3)$$

where  $\varepsilon$  is the dielectric constant and  $\mathbf{E}$  is the root-mean-square value of the electric field, In Eq. (3), the Coulomb

force term has been neglected, because as was previously stated the free charge density can be assumed to be zero. If the pressure is replaced by (El-Sayed, 2008)

$$\Pi = P - \frac{1}{2} \rho \frac{\partial \varepsilon}{\partial \rho} \mathbf{E}^2 \quad (4)$$

the electrostriction term disappears from the equation.

The equation of energy, neglecting the dissipation terms, is (Rudraiah and Kaloni, 2003; Rudraiah et al., 2007)

$$\rho c \left[ \frac{\partial \theta}{\partial t} + \frac{1}{m} (\mathbf{v} \cdot \nabla) \theta \right] = k \nabla^2 \theta \quad (5)$$

where  $\theta$  is the temperature,  $c$  is the specific heat, and  $k$  is the thermal conductivity. Because there is no free charge, the electrical equations are (El-Sayed, 1999)

$$\nabla \cdot (\varepsilon \mathbf{E}) = 0 \quad (6)$$

$$\nabla \times \mathbf{E} = 0, \text{ or } \mathbf{E} = -\nabla \phi \quad (7)$$

where  $\phi$  is the root-mean-square value of the electric potential. Finally, the mass density  $\rho$  and the dielectric constant  $\varepsilon$  are assumed to be functions of temperature as follows (Takashima, 1976)

$$\rho = \rho_0 [1 - \alpha(\theta - \theta_0)] \quad (8)$$

$$\varepsilon = \varepsilon_0 [1 - e(\theta - \theta_0)] \quad (9)$$

where  $\alpha$  and  $e$  are usually positive. It is clear that there exists the following steady solutions:

$$\bar{\mathbf{v}} = 0 \quad (10)$$

$$\bar{\theta} = \theta_0 - \beta z \quad (11)$$

$$\bar{\rho} = \rho_0 (1 + \alpha \beta z) \quad (12)$$

$$\bar{\varepsilon} = \varepsilon_0 (1 + e \beta z) \quad (13)$$

$$\bar{E}_x = \bar{E}_y = 0, \bar{E}_z = \frac{E_0}{(1 + e \beta z)} \quad (14)$$

$$\bar{\phi} = -\frac{E_0}{e \beta} \ln(1 + e \beta z) \quad (15)$$

where

$$\beta = \frac{\theta_0 - \theta_1}{d} \quad (16)$$

is the adverse temperature gradient and

$$E_0 = -\frac{e \beta \phi_1}{\ln(1 + e \beta d)} \quad (17)$$

is the root-mean-square value of the electric field at  $z = d$ . If necessary, the modified pressure  $\bar{\Pi}$  can be determined from

$$\nabla \bar{\Pi} = \bar{\rho} \mathbf{g} - \frac{1}{2} \bar{\mathbf{E}}^2 \nabla \bar{\varepsilon} \quad (18)$$

Note that Eq. (14) satisfies the condition that there exists a vertical electric field (i.e.,  $\bar{E}_x = \bar{E}_y = 0$ ), while  $\bar{E}_z$  is derived from Eq. (6) because  $\nabla \cdot (\bar{\varepsilon} \bar{\mathbf{E}}) = \partial(\bar{\varepsilon} \bar{E}_z)/\partial z = 0$  [i.e.,  $\bar{\varepsilon}(\partial \bar{E}_z/\partial z) + (\partial \bar{\varepsilon}/\partial z) \bar{E}_z = 0$ ], which on using Eq. (13) reduces to  $(1 + e \beta z)(\partial \bar{E}_z/\partial z) + e \beta \bar{E}_z = 0$ , and this equation is automatically satisfied by the solution  $\bar{E}_z = E_0/(1 + e \beta z)$  given by Eq. (14). Also, Eq. (15) results from equation (7), since  $\bar{\mathbf{E}} = -\nabla \bar{\phi}$  (i.e.,  $\bar{E}_z = -\partial \bar{\phi}/\partial z$ ), and hence,  $\bar{\phi} = -\int \bar{E}_z dz$ . Finally, Eq. (17) can be obtained directly from Eq. (15) using the condition that  $\bar{\phi} = \phi_1$  at  $z = d$ .

From physical considerations, a basic restriction is imposed on the analysis by neglecting the effect of centrifugal force. If we keep the centrifugal force term in the equation of motion, then Eq. (18) must be modified as (Takashima, 1976)

$$\nabla \bar{\Pi} = \bar{\rho} \mathbf{g} - \frac{1}{2} \bar{\mathbf{E}}^2 \nabla \bar{\varepsilon} + \frac{1}{2} \bar{\rho} \Omega^2 \nabla (x^2 + y^2) \quad (19)$$

However,  $\bar{\Pi}$  cannot be determined from Eq. (19) owing to the  $x$  and  $y$  dependence of the last term of Eq. (19). This means that the solutions given by Eqs. (10)–(17) cannot exist. In other words, the fluid cannot be quiescent when it is observed from the rotating frame of reference. This fact will make the problem exceedingly complicated (for more details, see the arguments given by Namikawa et al., 1970; Chakraborty, 1982; and later by El-Sayed, 2000; Douiebe et al., 2001, for different problems of interest). However, if we restrict our attention to the case when the ratio of the centrifugal force term to the gravitational force term (which is characterized by  $\Omega^2 r^2/gd$ ,  $r$  being the horizontal extent of the fluid layer) is small enough, then Eq. (19) may be reduced to Eq. (18), approximately, and the above-mentioned difficulty is avoided. This is the reason why we have neglected the centrifugal force. It should be noted that the same approximation has been made by many authors in the analyses on the stability of a rotating fluid layer heated from below, and its validity has been experimentally confirmed (see, for example, Chandrasekhar, 1981). It should also be noted that, even if

$\Omega^2 r^2 / gd$  is small, the Taylor number  $T = (2\Omega d^2 / \nu)^2$  (the square of the ratio of the Coriolis force term to the viscous term) can become large to a certain extent. This means that the effect of the Coriolis force is much larger than that of the centrifugal force. Thus, our analysis is valid only when  $\Omega^2 r^2 / gd$  is small.

### 3. LINEARIZATION AND BOUNDARY CONDITIONS

Let the initial steady state described by Eqs. (10)–(18) be slightly perturbed. Following the classical lines of linear stability theory as presented by Chandrasekhar (1981) and applying approximations analogous to the usual Boussinesq approximations, the equations governing small perturbations may be written as (Takashima, 1976; El-Sayed, 2008)

$$\frac{1}{m} \left[ \frac{\partial}{\partial t} - \nu \nabla^2 + \frac{m\nu}{k_1} \right] \nabla^2 w' = \left( \alpha g + \frac{\varepsilon_0 E_0^2 e^2 \beta}{\rho_0} \right) \nabla_H^2 \theta' + \frac{\varepsilon_0 E_0 e \beta}{\rho_0} \nabla_H^2 \left( \frac{\partial \phi'}{\partial z} \right) - \frac{2\Omega}{m} \frac{\partial \zeta'}{\partial z} \quad (20)$$

$$\frac{\partial \theta'}{\partial t} - K \nabla^2 \theta' = \frac{\beta}{m} w' \quad (21)$$

$$\nabla^2 \phi' + E_0 e \frac{\partial \theta'}{\partial z} = 0 \quad (22)$$

and

$$\left[ \frac{\partial}{\partial t} - \nu \nabla^2 + \frac{m\nu}{k_1} \right] \zeta' = 2\Omega \frac{\partial w'}{\partial z} \quad (23)$$

where  $w'$  is the  $z$  component of the velocity,  $\theta'$  is the perturbation of the temperature,  $\phi'$  is the perturbation of the potential,  $\zeta'$  is the  $z$  component of the vorticity,  $\nu = \mu / \rho_0$  is the kinematic viscosity,  $K = k / (c\rho_0)$  is the thermometric conductivity,  $\nabla_H^2 = \nabla^2 - \partial^2 / \partial z^2 = \partial^2 / \partial x^2 + \partial^2 / \partial y^2$  is the horizontal Laplacian, and the prime refers to perturbation quantities. Here, small terms have been neglected using the fact that  $|\alpha\beta z| \ll 1$  and  $|e\beta z| \ll 1$ .

Equations (20)–(23) are first rendered dimensionless by choosing  $d$ ,  $d^2/K$ ,  $K/d$ ,  $K/d^2$ ,  $\beta d$ ,  $d^2$ , and  $E_0 d$  as the units of length, time, velocity, vorticity, temperature, medium permeability, and electric potential, respectively. They are then simplified in the usual manner by decomposing the solution in terms of normal modes, so that

$$\begin{aligned} [w', \theta', \phi', \zeta'] &= [W(z), \Theta(z), \Phi(z), Z(z)] \\ &\times \exp[i(a_x x + a_y y) + \omega t] \end{aligned} \quad (24)$$

where  $\omega$  is the growth rate, which is complex, in general, and  $a_x$  and  $a_y$  are the wavenumbers. Thus, with all variables now made dimensionless, we arrive at

$$\begin{aligned} \frac{1}{m} (D^2 - a^2) \left[ P^{-1} \omega - (D^2 - a^2) + \frac{m}{k_1} \right] W \\ = -(R + L) a^2 \Theta - L_1 a^2 D \Phi - \frac{T^{1/2}}{m} D Z \end{aligned} \quad (25)$$

$$[\omega - (D^2 - a^2)] \Theta = \frac{1}{m} W \quad (26)$$

$$(D^2 - a^2) \Phi + L_2 D \Theta = 0 \quad (27)$$

$$\left[ P^{-1} \omega - (D^2 - a^2) + \frac{m}{k_1} \right] Z = T^{1/2} D W \quad (28)$$

where  $P = \nu / K$  is the Prandtl number,  $R = \alpha \beta g d^4 / (\nu K)$  is the Rayleigh number,  $L = L_1 L_2 = \varepsilon_0 (e \beta E_0 d^2)^2 / (\rho_0 \nu K)$  is the electrical Rayleigh number,  $T = (2\Omega d^2 / \nu)^2$  is the Taylor number,  $L_1 = \varepsilon_0 e \beta E_0^2 d^3 / (\rho_0 \nu K)$ ,  $L_2 = e \beta d$ ,  $D = d/dz$ , and  $a^2 = a_x^2 + a_y^2$ .

In seeking solutions of these equations, we must impose certain boundary conditions at the lower and upper surfaces, i.e.,  $z = 0$  and  $z = 1$ , respectively. The most realistic boundary conditions may be written as

$$W = DW = \Theta = \Phi = Z = 0 \text{ at } z = 0, 1 \quad (29)$$

In this paper, however, we shall use somewhat different boundary conditions given by

$$W = D^2 W = \Theta = D \Phi = D Z = 0 \text{ at } z = 0, 1 \quad (30)$$

This case, although admittedly an artificial one to consider, is of importance because its exact solution is readily obtained. Furthermore, from past experience with problems of this kind (see, for example, Turnbull and Melcher, 1969), one may feel fairly confident that the general features of the physical situation will be disclosed by a discussion of this case equally as well as by a discussion of solutions satisfying less artificial boundary conditions. Consequently, the essential feature of the problem will be unaffected by taking these boundary conditions (30), with the only possible change being expected in numerical values of the parameters.

Equations (25)–(28) and the boundary conditions (30) constitute an eigenvalue system for the present problem.

These equations can be readily combined to yield

$$\left\{ (D^2 - a^2)^2 \left[ (D^2 - a^2) - \frac{\omega}{P} - \frac{m}{k_1} \right]^2 [(D^2 - a^2) - \omega] \right. \\ \left. + a^2 [R(D^2 - a^2) - La^2] \left[ (D^2 - a^2) - \frac{\omega}{P} - \frac{m}{k_1} \right] \right. \\ \left. + TD^2(D^2 - a^2) [(D^2 - a^2) - \omega] \right\} \Theta = 0 \quad (31)$$

together with

$$\Theta = D^2\Theta = 0 \text{ at } z = 0, 1 \quad (32)$$

Examination of Eqs. (31) and (32) indicates that the relevant solution for  $\Theta$  is given by

$$\Theta = \sum_{n=1}^{\infty} A_n \sin n\pi z \quad (33)$$

substitution of this solution in Eq. (31) leads to the required eigenvalue relationship of the form

$$L = \frac{(n^2\pi^2 + a^2)}{a^4} \left\{ (n^2\pi^2 + a^2) [n^2\pi^2 + a^2 + \omega] \right. \\ \times \left[ n^2\pi^2 + a^2 + \frac{\omega}{P} + \frac{m}{k_1} \right] + Tn^2\pi^2 [n^2\pi^2 + a^2 + \omega] \\ \left. \times \left[ n^2\pi^2 + a^2 + \frac{\omega}{P} + \frac{m}{k_1} \right]^{-1} - Ra^2 \right\} \quad (34)$$

#### 4. EXCHANGE OF STABILITIES

If the temporal growth rate  $\omega$ , given in Eq. (34), vanishes, then the principle of exchange of stabilities occurs. In this case, when we put  $\omega = 0$  in Eq. (34), we obtain

$$L = \frac{(n^2\pi^2 + a^2)}{a^4} \left\{ (n^2\pi^2 + a^2)^2 \left[ n^2\pi^2 + a^2 + \frac{m}{k_1} \right] \right. \\ \left. + \frac{Tn^2\pi^2(n^2\pi^2 + a^2)}{[n^2\pi^2 + a^2 + (m/k_1)]} - Ra^2 \right\} \quad (35)$$

which shows that the exchange of stabilities case does not depend on the Prandtl number.

For given  $R$ ,  $a$ ,  $T$ ,  $m$ , and  $k_1$ , the lowest value of  $L$  occurs when  $n = 1$ ; then,

$$L = \frac{(\pi^2 + a^2)}{a^4} \left\{ (\pi^2 + a^2)^2 \left[ \pi^2 + a^2 + \frac{m}{k_1} \right] \right. \\ \left. + \frac{T\pi^2(\pi^2 + a^2)}{[\pi^2 + a^2 + (m/k_1)]} - Ra^2 \right\} \quad (36)$$

In the limiting case of purely fluids (nonporous medium), i.e. when  $k_1 \rightarrow \infty$ , Eq. (36) reduces to the same equation obtained earlier by Takashima (1976), and his results are therefore recovered.

For a fixed value of  $R$ , the lowest point of  $L$  defined by Eq. (36) as a function of  $a$ ,  $T$ ,  $m$ , and  $k_1$ , gives the critical electrical Rayleigh number  $L_c$  as

$$L_c = \frac{(\pi^2 + a^2)}{a^4} \left\{ (\pi^2 + a^2)^2 \left[ \pi^2 + a^2 + \frac{m}{k_1} \right] \right. \\ \left. + \frac{T\pi^2(\pi^2 + a^2)}{[\pi^2 + a^2 + (m/k_1)]} - Ra^2 \right\} \quad (37)$$

and the corresponding critical wavenumber  $a_c$  for the case of exchange of stabilities.

Minimizing Eq. (37) with respect to  $a^2$ , yields the sixth-order equation in  $a^2$  as

$$2k_1^3(a^2)^6 + k_1^2[4m + 8k_1\pi^2 - k_1R](a^2)^5 \\ + 2k_1[m^2 + 6k_1m\pi^2 + 5k_1^2\pi^4 - k_1mR \\ - k_1^2\pi^2R](a^2)^4 + k_1[-2k_1m\pi^2 + 4m^2\pi^2 + 8k_1m\pi^4 \\ - m^2R - 2k_1m\pi^2R - k_1^2\pi^4R + k_1m\pi^2T](a^2)^3 \\ - 2\pi^2[2k_1m^2 + 3k_1^2m\pi^2 + 4k_1^2m\pi^4 + 5k_1^3\pi^6](a^2)^2 \\ - 2\pi^2[m^3 + 4k_1m^2\pi^2 + 3k_1^2m\pi^4 + 2k_1m^2\pi^4 \\ + 6k_1^2m\pi^6 + 4k_1^3\pi^8](a^2) - 2\pi^4[m^3 + 2k_1m^2\pi^2 \\ + k_1^2m\pi^4 + k_1m^2\pi^4 + 2k_1^2m\pi^6 + k_1^3\pi^8] = 0 \quad (38)$$

Solving the Eq. (38) for  $a^2$  gives the critical wavenumber  $a_c^2$ . Furthermore, substituting this critical wavenumber  $a_c^2$  into Eq. (37) yields the critical electrical Rayleigh number  $L_c$  for exchange of stability. In order to plot the neutral stability curves in the  $(R, L_c)$  plane, a numerical search was conducted to seek the lowest point of  $L_c$  as a function of  $a_c$  for various assigned values of  $R$ ,  $m$ ,  $k_1$ , and  $T$ . This lowest point gives the critical electrical Rayleigh number  $L_c = L_c(R, m, k_1, T)$  and the corresponding critical wavenumber  $a_c = a_c(R, m, k_1, T)$ . The required neutral stability curves are given by plotting  $L_c$  against  $R$  for various assigned values of  $m$ ,  $k_1$ , and  $T$ . It should be noted here that when the fluid layer is heated from below,  $R$  is positive, whereas when the fluid layer is heated from above,  $R$  is negative.

The region of exchange of stabilities for different values of the porosity of porous medium  $m$  is shown in Fig. 1. We observe from Fig. 1 that an increase in the value of porosity of porous medium increases the critical electrical Rayleigh number of the stationary mode. Figure 2 illustrates the variation of critical electrical Rayleigh

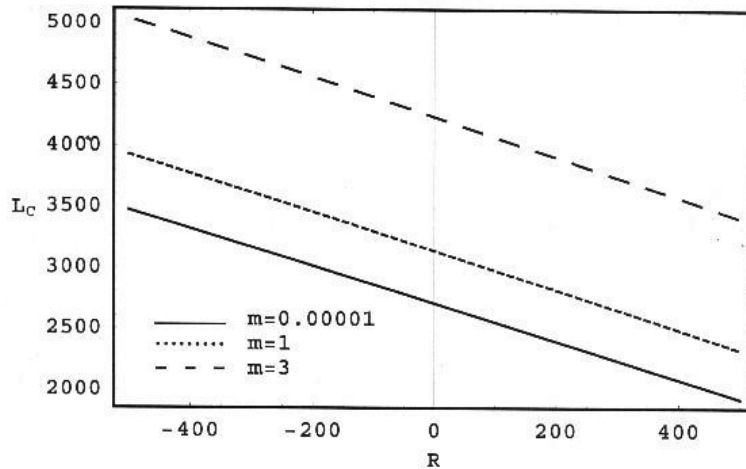


**FIG. 1:** Variation of critical electrical Rayleigh number  $L_c$ , given by Eq. (37), as a function of  $R$  for various values of  $m$  ( $= 0.00001, 1, 5$ ) when  $k_1 = 0.1$  and  $T = 1000$

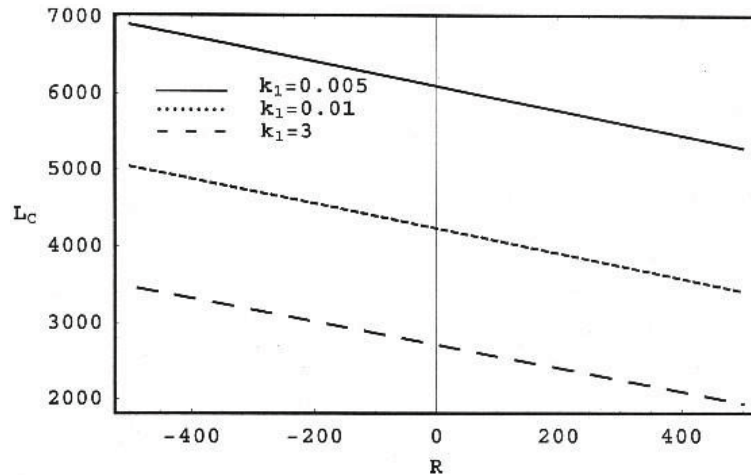


**FIG. 2:** Variation of critical electrical Rayleigh number  $L_c$ , given by Eq. (37), as a function of  $R$  for various values of  $k_1$  ( $= 0, 0.01, 0.05, 3$ ) when  $m = 0.3$  and  $T = 1000$

number  $L_c$  with the Rayleigh number  $R$  for different values medium permeability  $k_1$  for stationary case. We find from Fig. 2 that an increase in the value of medium permeability decreases the critical electrical Rayleigh number and hence increases the region of marginal stability. We see from Figs. 3 and 4 that the Coriolis force has an inhibiting effect on the onset of instability even if both the electrical effect and the presence of porous media are taken into account. Moreover, we see from Figs. 3 and 4 that as  $T$  becomes large, the neutral stability curve becomes closely linear with  $R$ , and the value of  $a_c$  becomes independent of  $R$ . This means that as the speed of rotation

increases, the coupling between the two agencies causing instability (electrical force and buoyancy) becomes tighter. This fact is in marked contrast with the case of convective instability induced by surface tension and buoyancy (Namikawa et al., 1970)

Let  $L_L$  and  $a_L$  denote, respectively, the values of  $L_c$  and  $a_c$  when  $R = 0$ ; and let  $R_R$  and  $a_R$  denote, respectively, the values of  $R$  and  $a_c$  that cause the value of  $L_c$  to be zero. Then  $L_L$  and  $a_L$  represent, respectively, the critical electrical Rayleigh number and the critical wavenumber for the case when electrical force is the sole agency causing instability. On the other hand,  $R_R$  and  $a_R$  rep-

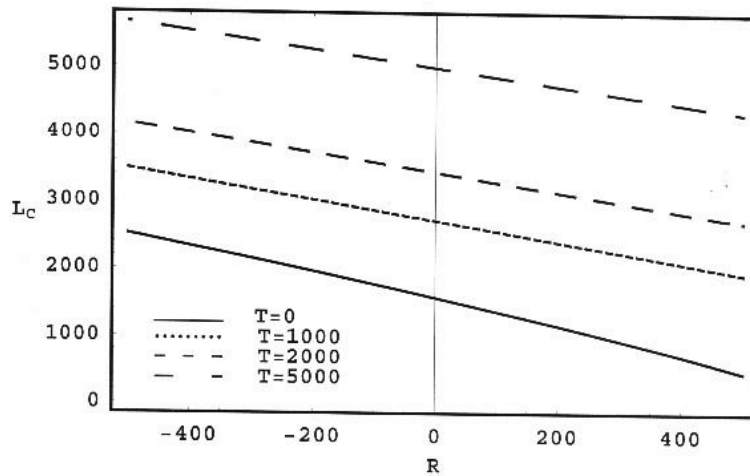


**FIG. 3:** Variation of critical electrical Rayleigh number  $L_c$ , given by Eq. (37), as a function of  $R$  for various values of  $T$  ( $= 0, 1000, 2000, 4000$ ) when  $m = 0.3$  and  $k_1 = 1$

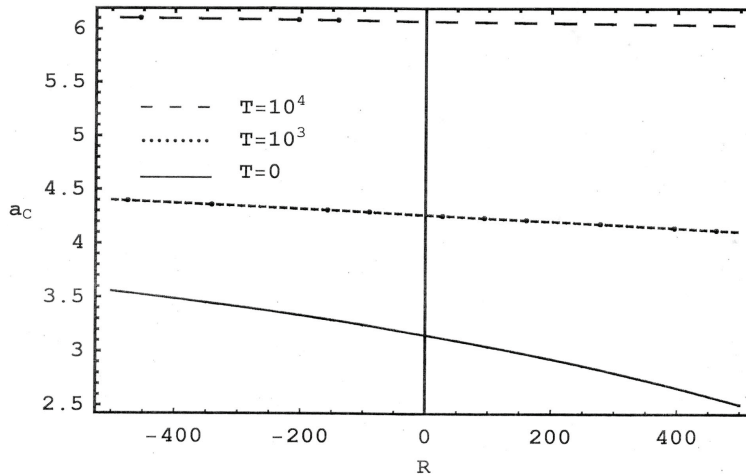


**FIG. 4:** Variation of critical wavenumber  $a_c$ , obtained from the solution of Eq. (38), as a function of  $R$  for various values of  $T$  ( $= 0, 10^4, 10^5$ ) when  $m = 0.3$  and  $k_1 = 1$

resent, respectively, the critical Rayleigh number and the critical wavenumber for the case when buoyancy is the sole agency causing instability. Then, we have

$$L_L = \frac{(\pi^2 + a^2)}{a^4} \left\{ (\pi^2 + a^2)^2 \left[ (\pi^2 + a^2) + \frac{m}{k_1} \right] + \frac{T\pi^2(\pi^2 + a^2)}{[(\pi^2 + a^2) + (m/k_1)]} \right\} \quad (39)$$

where the critical wavenumber  $a_L$  can be obtained from the solution of the following equation:

$$2k_1^3(a^2)^6 + [5k_1^2m + 8k_1^3\pi^2](a^2)^5 + 2[2k_1m^2 + 7k_1^2m\pi^2 + 5k_1^3\pi^4](a^2)^4 + [m^3 + 6k_1m^2\pi^2 + 6k_1^2m\pi^4 + k_1^3\pi^2T](a^2)^3 - 2[3k_1m^2\pi^4 + 8k_1^2m\pi^6 + 5k_1^3\pi^8 + 2k_1^3\pi^4T](a^2)^2 - [3m^3\pi^4 + 14k_1m^2\pi^6 + 19k_1^2m\pi^8 + 8k_1^3\pi^{10} + 2k_1^2m\pi^4T + 5k_1^3\pi^6T](a^2) - 2[m^3\pi^6 + 3k_1m^2\pi^8 + 3k_1^2m\pi^{10} + k_1^3\pi^{12} + k_1^2m\pi^6T + k_1^3\pi^8T] = 0 \quad (40)$$

The values of critical electrical Rayleigh number  $L_L$  and the corresponding critical wavenumber  $a_L$  as func-



tions of the Taylor number  $T$  when  $R = 0$ , given by Eq. (39) and the solution of Eq. (40) for various values of the porosity of porous medium are shown in Figs. 5a and 5b, respectively, for the case of exchange of stabilities. It is clear from Fig. 5a that when  $R = 0$ , the critical electrical Rayleigh number  $L_L$  is always positive, and it increases by increasing both the porosity of porous medium  $m$  and the Taylor number  $T$ . Therefore their effects are stabilizing. It is obvious from Fig. 5b that when  $R = 0$ , the critical wavenumber  $a_L$  is always positive, and it increases by increasing  $m$  for small values of  $T$ , while it decreases by increasing  $m$  for high values of  $T$ . On the other hand, the values of critical Rayleigh number  $R_R$  and the corresponding critical wavenumber  $a_R$  with the Taylor number  $T$  when  $L_c = 0$ , obtained from Eq. (37) and

the solution of Eq. (38) for various values of the porosity of porous medium  $m$  can also be investigated (figures are not given here to save space). It is found that  $m$  has the same effects on  $R_R$  and  $a_R$  as on  $L_L$  and  $a_L$ , respectively.

The effects of the medium permeability  $k_1$  on  $L_L$  and  $a_L$  are shown in Figs. 6a and 6b, respectively. It is clear from Fig. 6a that the critical electrical Rayleigh number  $L_L$  decreases by increasing  $k_1$  for any value of the Taylor number  $T$ , i.e., the medium permeability  $k_1$  has a destabilizing effect on the considered system, while for any value of  $k_1$ , we find that  $L_L$  increases by increasing the Taylor number  $T$ . Figure 6b shows that the critical wavenumber  $a_L$  decreases by increasing  $k_1$  for small values of  $T$ , while it increases by increasing  $k_1$  for high values of  $T$ . Also, the effects of  $k_1$  on both  $R_R$  and  $a_R$ , respectively,

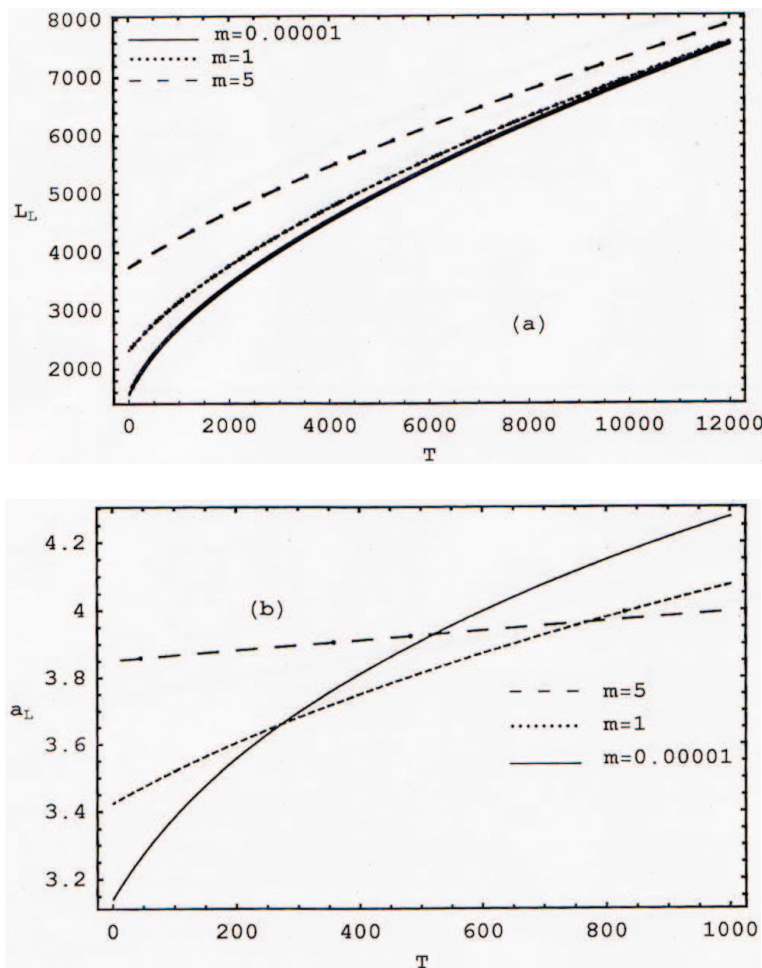


**FIG. 5:** Variation of (a) critical electrical Rayleigh number  $L_L$ , given by Eq. (39), and (b) critical wavenumber  $a_L$  obtained from the solution of Eq. (40), as function of  $T$  for various values of  $m$  ( $= 0.00001, 1, 5$ ) when  $k_1 = 0.1$

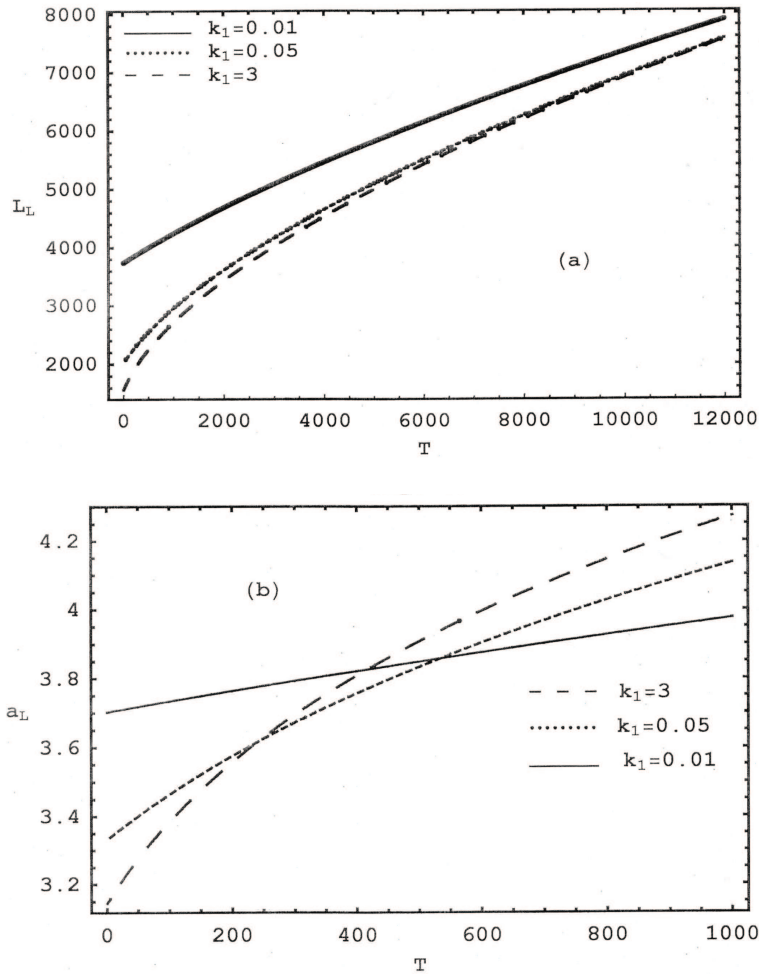


**FIG. 6:** Variation of (a) critical electrical Rayleigh number  $L_L$ , given by Eq. (39), and (b) critical wavenumber  $a_L$  obtained from the solution of Eq. (40), as function of  $T$  for various values of  $k_1$  ( $= 0, 01, 0.05, 3$ ) when  $m = 0.3$

given by Figs. 7a, 7b, 8a, and 8b are found to be similar to its effects on  $L_L$  and  $a_L$  given by Figs. 6a and 6b, respectively.

Figures 5a and 6a show also that both the porosity of the porous medium  $m$  and the medium permeability  $k_1$  have no effects on the stability of the considered system for highly Taylor number  $T$  values, because the obtained curves are coincide in this case. Moreover, Figs. 6a and 6b at which  $R = 0$  in comparison to Figs. 1 and 2 at which  $R \neq 0$  indicate that the Rayleigh number  $R$  has a destabilizing effect on the considered system.

Now, if we define the porous medium parameter  $\kappa$  as  $\kappa = m/k_1$  (which represents the ratio of the porosity of the porous medium to the medium permeability), then Eqs. (39) and (40) can be rewritten in the form

$$L_c = \frac{(\pi^2 + a^2)}{a^4} \left\{ (\pi^2 + a^2)^2 [\pi^2 + a^2 + \kappa] + \frac{T\pi^2(\pi^2 + a^2)}{[\pi^2 + a^2 + \kappa]} - Ra^2 \right\}$$

and

$$2(a^2)^6 + [4\kappa + 8\pi^2 - R](a^2)^5 + 2[\kappa^2 + 6\kappa\pi^2 + 5\pi^4 - \kappa R - \pi^2 R](a^2)^4 + [-2\kappa\pi^2 + 4\kappa^2\pi^2 + 8\kappa\pi^4 - \kappa^2 R - 2\kappa\pi^2 R - \pi^4 R + \kappa\pi^2 T](a^2)^3 - 2\pi^2[2\kappa^2 + 3\kappa\pi^2 + 4\kappa\pi^4 + 5\pi^6](a^2)^2 - 2\pi^2[\kappa^3 + 4\kappa^2\pi^2 + 3\kappa\pi^4 + 2\kappa^2\pi^4 + 6\kappa\pi^6 + 4\pi^8](a^2) - 2\pi^4[\kappa^3 + 2\kappa^2\pi^2 + \kappa\pi^4 + \kappa^2\pi^4 + 2\kappa\pi^6 + \pi^8] = 0$$

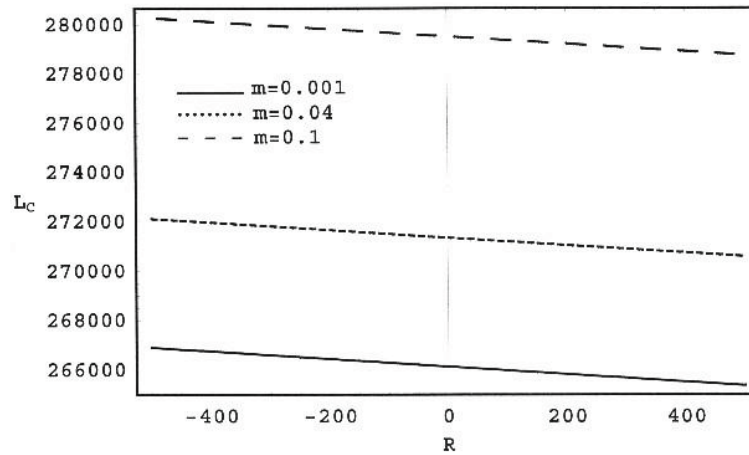


**FIG. 7:** Variation of critical electrical Rayleigh number  $L_c$ , given by Eq. (46), as a function of  $R$  for various values of  $m$  ( $= 0.00001, 0.04, 0.1$ ) when  $k_1 = 1$ ,  $P = 50$ , and  $T = 1000$

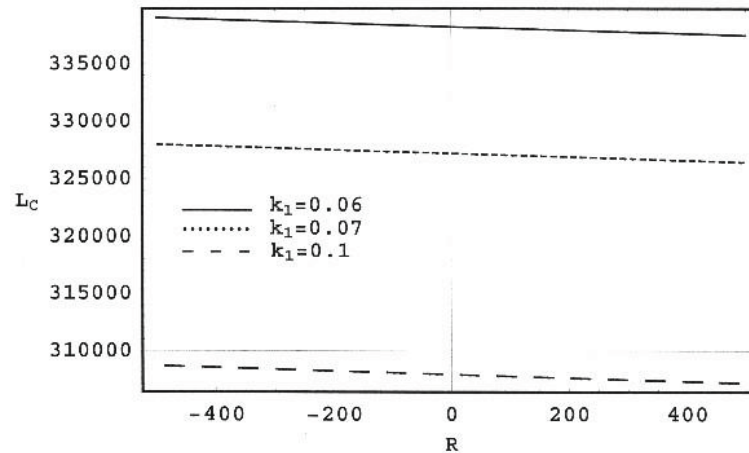


**FIG. 8:** Variation of critical electrical Rayleigh number  $L_c$ , given by Eq. (46), as a function of  $R$  for various values of  $k_1$  ( $= 0.06, 0.07, 0.1$ ) when  $m = 0.3$ ,  $P = 50$ , and  $T = 1000$

In this case, we found that the effect of the porous medium parameter  $\kappa$  on the stability of the considered system is exactly similar to the effect of porosity of the porous medium  $m$  (at any constant value of medium permeability) on the system shown in Fig. 1, but the corresponding figure is not given here to avoid repetition.

## 5. PRINCIPLE OF OVERSTABILITY

Because the temporal growth rate  $\omega$ , given in Eq. (24) can be rewritten as  $\omega = \omega_r + i\omega_i$ , then for  $\omega_r < 0$ , the system is always stable. On the other hand, for  $\omega_r > 0$ , the system becomes unstable. When  $\omega = 0$ , the sys-

tem is marginally stable under the principle of exchange of stabilities as shown in the previous section. In particular, when  $\omega_r = 0$  and  $\omega_i \neq 0$ , the overstability of periodic motion is possible and oscillatory motion occurs (Hennenberg et al., 1997). The minimum value of the electrical Rayleigh number at the marginal condition of  $\omega_i \neq 0$  is regarded as the critical value to make the onset of convection. However, in addition to the exchange of stabilities, it is of most interest here to investigate overstability [i.e., the condition for a stable state to transit into an unstable state (or vice versa)] is not  $\omega = 0$ , but  $\omega = i\omega_i$  with  $\omega_i$  is a real number (Payne and Straughan, 1998). In this case, substituting  $\omega = i\omega_i$  and

$n = 1$  into Eq. (34) and imposing the condition  $\omega_i^2 > 0$ , which is necessary to get oscillatory instability, we obtain two algebraic equations by equating both the real and imaginary parts on both sides of Eq. (34), separately. This gives the electrical Rayleigh number  $L$ , and the frequency  $\omega_i$  of the oscillations at marginal stability of the form

$$L \left[ \pi^2 + a^2 + \frac{m}{k_1} \right] = \frac{(\pi^2 + a^2)}{a^4} \left\{ (\pi^2 + a^2)^2 \right. \quad (41)$$

$$\times \left[ \left( \pi^2 + a^2 + \frac{m}{k_1} \right)^2 - \frac{\omega_i^2}{P^2} \right] - \frac{2\omega_i^2}{P} (\pi^2 + a^2)$$

$$\left. \times \left[ \pi^2 + a^2 + \frac{m}{k_1} \right] + TP\pi^2(\pi^2 + a^2) - Ra^2 \left[ \pi^2 + a^2 + \frac{m}{k_1} \right] \right\}$$

and

$$\omega_i^2 = \frac{P}{(\pi^2 + a^2)} \left\{ -\frac{La^4}{(\pi^2 + a^2)} + 2(\pi^2 + a^2)^2 \right.$$

$$\times \left[ \pi^2 + a^2 + \frac{m}{k_1} \right] + P(\pi^2 + a^2) \left[ \pi^2 + a^2 + \frac{m}{k_1} \right]^2$$

$$\left. + TP\pi^2 - Ra^2 \right\} \quad (42)$$

where the physical meaning of  $L$  requires it to be real. The condition  $\omega_i^2 > 0$  implies that

$$\left[ \frac{La^4}{(\pi^2 + a^2)} + Ra^2 \right] < (\pi^2 + a^2) \left\{ 2(\pi^2 + a^2) \right.$$

$$\times \left[ \pi^2 + a^2 + \frac{m}{k_1} \right] + P \left[ \pi^2 + a^2 + \frac{m}{k_1} \right]^2$$

$$\left. + \frac{TP\pi^2}{(\pi^2 + a^2)} \right\} \quad (43)$$

It is evident that oscillatory instability cannot be established if the condition (43) is not satisfied, because this implies  $\omega_i^2 < 0$ . Note also that the condition (43) can be satisfied for small values of the Rayleigh number  $R$  and electrical Rayleigh number  $L$ , or for large values of the Prandtl number  $P$  and Taylor number  $T$ , respectively.

Eliminating  $\omega_i$  between Eqs. (41) and (42), then the electrical Rayleigh number can be expressed in the form

$$L = \frac{(\pi^2 + a^2)}{a^4} \left[ \frac{(\pi^2 + a^2)(1 + P)}{P} + \frac{m}{k_1} \right]^{-1}$$

$$\times \left\{ -(\pi^2 + a^2)^2 \left[ \pi^2 + a^2 + \frac{m}{k_1} \right]^2 \right.$$

$$+ \left[ \frac{(\pi^2 + a^2)(1 + 2P)}{P} + \frac{2m}{k_1} \right] \left[ 2(\pi^2 + a^2) \left( \pi^2 + a^2 + \frac{m}{k_1} \right) \right.$$

$$+ P(\pi^2 + a^2) \left( \pi^2 + a^2 + \frac{m}{k_1} \right) + TP\pi^2 - Ra^2 \left. \right]$$

$$\left. - T\pi^2(\pi^2 + a^2) + Ra^2 \left[ \pi^2 + a^2 + \frac{m}{k_1} \right] \right\} \quad (44)$$

The critical electrical Rayleigh number  $L_c$  for the overstability is obtained by minimizing Eq. (44) with respect to  $a$ . Although the minimization can be done by letting  $\partial L / \partial a = 0$  for nonzero porous term ( $m/k_1$ ), it is not analytically tractable. From Eq. (44), we can find that unlike the exchange of stabilities, the overstability is dependent on the Prandtl number. In this case, the critical wavenumber  $a_c$  can be obtained from the solution of the following equation

$$-4k_1^4 P^2 (1 + P) (a^2)^6 - 2k_1^3 [3mP^2 (1 + 2P)$$

$$+ k_1 (1 + P) (1 + 2P + 8P^2 \pi^2)] (a^2)^5 - 4k_1^2 [mP$$

$$+ k_1 \pi^2 (1 + P)] \{ 3mP^2 + k_1 [1 + P(2 + 5P\pi^2)] \} (a^2)^4$$

$$+ k_1 (2m^3 P^2 (1 - 2P) + 2k_1 m^2 P [1 - 2P - 6P\pi^2$$

$$\times (P - 1)] + 4k_1^2 m \pi^2 \{ 1 + P[3 + P\pi^2(3 - 2P)] \}$$

$$+ k_1^3 \pi^2 (1 + P) [\pi^2 (4 + 8P) - R(1 + P) + 2P^2 T])$$

$$\times (a^2)^3 + 2k_1 \pi^2 (1 + P) \{ 4m^3 P^2 + 2k_1 m^2 P$$

$$\times (4 + 9P\pi^2) + k_1^3 \pi^2 [8\pi^2 (1 + 2P) + 10P^2 \pi^4$$

$$- R(1 + P) + 4P^2 T] + k_1^2 m [6\pi^2 (1 + 4P) + 24P^2 \pi^4$$

$$+ P(2PT - R)] \} (a^2)^2 + \pi^2 (4m^4 P^3 + 2k_1 m^3 P^2$$

$$\times [4 + \pi^2 (5 + 14P)] + k_1^4 \pi^4 (1 + P) [14\pi^2 (1 + 2P)$$

$$+ 16P^2 \pi^4 - R(1 + P) + 10P^2 T] + k_1^2 m^2 P$$

$$\times [\pi^2 (26 + 44P) + 12P\pi^4 (3 + 5P) + P(2PT - R)]$$

$$+ 2k_1^3 m \pi^2 \{ \pi^2 (6 + 34P + 32P^2) + P^2 \pi^4 (21 + 26P)$$

$$+ P[-R(1 + P) + 2PT(2 + 3P)] \} (a^2) + 4\pi^4$$

$$\times (m + k_1 \pi^2) [mP + k_1 \pi^2 (1 + P)] [m^2 P^2 + 2k_1 mP$$

$$\times (1 + P\pi^2) + k_1^2 (\pi^2 + 2P\pi^2 + P^2 \pi^4 + P^2 T)] = 0 \quad (45)$$

We solve Eq. (45) for  $a^2$ , which gives the critical wavenumber  $a_c^2$ , and substituting this critical wavenumber into Eq. (44) yields the critical electrical Rayleigh

number  $L_c$  for the oscillatory instability. Substituting the critical wavenumber and critical electrical Rayleigh number of oscillatory instability into the Eq. (42) gives the critical frequency of oscillatory case.

The region of overstability for different values of the porosity of a porous medium  $m$  is shown in Fig. 7. We observe from this figure that an increase in the value of porosity of porous medium  $m$  increases the critical electrical Rayleigh number of the overstability mode. Figure 8 illustrates the variation of critical electrical Rayleigh number  $L_c$  with the Rayleigh number  $R$  for different values medium permeability  $k_1$  for overstability case. We

note from Fig. 8 that an increase in the value of medium permeability  $k_1$  decreases the critical electrical Rayleigh number and hence decreases the region of marginal stability. Figures 7 and 8 show also that the above-mentioned effects of  $m$  and  $k_1$  occur if the liquid layer is heated from below or above (i.e., when  $R \geq 0$ ), respectively, and that for any value of  $m$  or  $k_1$ , the critical electrical Rayleigh numbers  $L_c$  decreases linearly with the Rayleigh number  $R$ .

Figures 9 and 10 show the variations of critical electrical Rayleigh number  $L_c$  with the Rayleigh number  $R$  for various values of the Taylor number  $T$  and the Prandtl

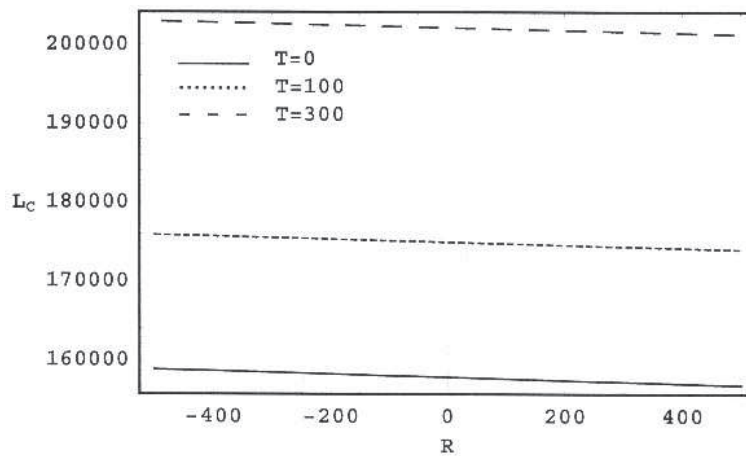


**FIG. 9:** Variation of critical electrical Rayleigh number  $L_c$ , given by Eq. (46), as a function of  $R$  for various values of  $T$  ( $= 0, 100, 300$ ) when  $m = 0.3, k_1 = 1, P = 50$ , and  $T = 1000$

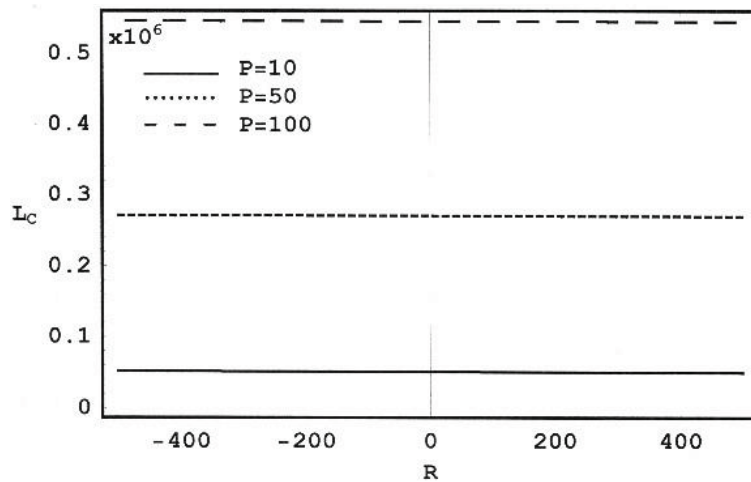


**FIG. 10:** Variation of critical electrical Rayleigh number  $L_c$ , given by Eq. (46), as a function of  $R$  for various values of  $P$  ( $= 30, 50, 100$ ) when  $m = 0.3, k_1 = 1$ , and  $T = 1000$

number  $P$ , respectively. It can be seen from Figs. 9 and 10 that an increase in the values of  $T$  or  $P$  increases the critical electrical Rayleigh number  $L_c$  of the overstability state irrespective of the the Rayleigh number  $R$  is positive or negative. Figures 9 and 10 indicate also that for any value of the Taylor number  $T$ , the critical electrical Rayleigh number  $L_c$  slightly decreases linearly by increasing the Rayleigh number  $R$ , while for any value of the Prandtl number  $P$ , the critical electrical Rayleigh number  $L_c$  does not depend on the Rayleigh number  $R$  values. Note that the effect of porous medium parameter  $\kappa = m/k_1$  on the stability of the considered system, in this case of overstability convection, has been found also similar to the effect of porosity of porous medium discussed in Fig. 7 as shown in the exchange of stabilities case.

## 6. CONCLUSIONS

In the present study, we have employed a linear theory analysis for the problem of the onset of electrohydrodynamic instability in a horizontal layer of viscous rotating dielectric fluid through a Brinkman porous medium under the simultaneous action of a vertical ac electric field and a vertical temperature gradient. Our analysis is performed by neglecting the centrifugal force because the effect of the Coriolis force is found to be much larger than that of the centrifugal force. Analytical expressions have found for the onset of exchange of stability (in the presence or absence of Rayleigh number and/or electrical Rayleigh number), overstability and oscillatory frequency, which depend on the porosity of porous medium, the medium permeability, the Taylor number, the Prandtl number, as well as the Rayleigh number. The critical wavenumbers corresponding to these cases are also found to depend on these quantities.

**Case I:** In the exchange of stability case, we found the following:

1. The porosity of porous medium and the Coriolis force have stabilizing effects.
2. The medium permeability and the Rayleigh number values have destabilizing effects.
3. The effects of porosity of porous medium, Taylor number, and medium permeability on the stability of the considered system occur for any positive or negative value of the Rayleigh number.
4. For high Taylor number values, the critical electrical Rayleigh number and the corresponding critical

wavenumbers are independent of the Rayleigh number.

5. In absence of Rayleigh number, the Taylor number has a stabilizing effect (for fixed values of porosity of porous medium and medium permeability), while porosity of porous medium and medium permeability have stabilizing and destabilizing effects, respectively (for fixed value of Taylor number), but they have no effect on the stability of the considered system (for high Taylor number values).
6. The critical wavenumber decreases or increases by increasing the porosity of porous medium or medium permeability, respectively (for small Taylor number values), while it increases or decreases by increasing the porosity of porous medium or medium permeability, respectively (for high Taylor number values).

**Case II:** In the overstability case (in which the frequency of the oscillations at marginal stability  $\omega_i^2$  is positive), we found the following:

1. The porosity of porous medium and Taylor number have stabilizing effects, while the medium permeability and Rayleigh number have destabilizing effects and the critical electrical Rayleigh number decreases linearly with the Rayleigh number.
2. The Prandtl number has a stabilizing effect, while for any value of Prandtl number, the critical electrical Rayleigh number does not depend on the Rayleigh number.
3. The previous results in this case occur if the liquid layer is heated from below or above.

Finally, it should be noted that the stability or instability effects of various physical parameters included in the analysis occur faster in the case of exchange of stability than their effects in the case of overstability, because the corresponding values of critical electrical Rayleigh numbers in the exchange of stability case are smaller than their values in the overstability case. Note also that the effect of a porous medium parameter on the instability of the considered system is found to be similar to the effect of a porous medium in both the cases of stationary and oscillatory convections, respectively.

## ACKNOWLEDGMENTS

The author thanks Prof. N. T. M. Eldabe, Ain Shams University, Egypt, for his critical reading of this paper and

also thanks both reviewers for their valuable comments and suggestions that improved the original version of the paper.

## REFERENCES

- Busse, F. H. and Heikes, K. E., Convection in a rotating layer: A simple case of turbulence, *Science*, vol. 208, pp. 173–175, 1980.
- Cebeci, T. and Bradshaw, P., *Physical and Computational Aspects of Convective Heat Transfer*, Springer, New York, 1984.
- Chakraborty, B. B., Hydromagnetic Rayleigh-Taylor instability of a rotating stratified fluid, *Phys. Fluids*, vol. 25, pp. 743–747, 1982.
- Chandrasekhar, S., *Hydrodynamic and Hydromagnetic Stability*, Dover Publications, New York, 1981.
- Clever, R. M. and Busse, F. H., Convection in a low Prandtl number fluid layer rotating about a vertical axis, *Eur. J. Mech. B*, vol. 19, pp. 213–227, 2000.
- Cross, M. C. and Kim, L., Linear instability and codimension-2 region in binary fluid convection between rigid impermeable boundaries, *Phys. Rev. A*, vol. 37, pp. 3909–3920, 1988.
- Douiebe, A., Hannaoui, M., Lebon, G., Benaboud, A., and Khmou, A., Effects of a.c. electric field and rotation on Bénard-Marangoni convection, *Flow, Turbulence Combust.*, vol. 67, pp. 185–204, 2001.
- El-Sayed, M. F., Electrohydrodynamic interfacial stability conditions in the presence of heat and mass transfer and oblique electric fields, *Z. Naturforsch. A*, vol. 54, pp. 470–476, 1999.
- El-Sayed, M. F., Effect of a variable magnetic field on the instability of a stratified rotating fluid layer in porous medium, *Czech. J. Phys.*, vol. 50, pp. 607–614, 2000.
- El-Sayed, M. F., Onset of electroconvective instability of Oldroydian viscoelastic liquid layer in Brinkman porous medium, *Arch. Appl. Mech.*, vol. 78, pp. 211–224, 2008.
- Hennenberg, H., Saghir, M. Z., Rednikov, A., and Legros, J. C., Porous media and the Bénard-Marangoni problem, *Transp. Porous Media*, vol. 27, pp. 327–355, 1997.
- Hsu, C. T. and Cheng, P., The Brinkman model for the natural convection about a semi-infinite vertical flat plate in a porous medium, *Int. J. Heat Mass Transfer*, vol. 28, pp. 683–697, 1985.
- Ingham, D. B. and Pop, I. (Eds.), *Transport Phenomena in Porous Media*, Pergamon, Oxford, 1998.
- Kelly, R. E. and Pal, D., Thermal convection with spatially periodic boundary conditions: resonant wavelength excitation, *J. Fluid Mech.*, vol. 86, pp. 433–456, 1978.
- Khiri, R., Coriolis effect on convection for a low Prandtl number fluid, *Int. J. Non-Linear Mech.*, vol. 39, pp. 593–604, 2004.
- Landau, L. D. and Lifshitz, E. M., *Electrodynamics of Continuous Media*, Pergamon Press, New York, 1960.
- Lapwood, E. R., Convection of a fluid in a porous medium, *Proc. Cambridge Philos. Soc.*, vol. 44, pp. 508–521, 1948.
- Malashetty, M. S. and Gaikwad, S. M., Onset of convective instabilities in a binary liquid mixtures with fast chemical reactions in a porous medium, *Heat Mass Transfer*, vol. 39, pp. 415–420, 2003.
- Malkus, W. V. R. and Veronis, G., Finite amplitude cellular convection, *J. Fluid Mech.*, vol. 4, pp. 225–260, 1958.
- Melcher, J. R., *Continuum Electromechanics*, MIT Press, Cambridge, MA, 1981.
- Namikawa, T., Takashima, M., and Matsushita, S., The effect of rotation on convective instability induced by surface tension and buoyancy, *J. Phys. Soc. Jpn.*, vol. 28, pp. 1340–1349, 1970.
- Nazzar, R., Amin, N., Filip, D., and Pop, I., The Brinkman model for the mixed convection boundary layer flow past a horizontal circular cylinder in a porous medium, *Int. J. Heat Mass Transfer*, vol. 46, pp. 3167–3178, 2003.
- Nepomnyashchy, A. A., Simaanovskii, I. B., and Legros, J. C., *Interfacial Convection in Multilayer Systems*, Springer-Verlag, New York, 2006.
- Nield, D. A., Convection in porous medium with inclined temperature gradient, *Int. J. Heat Mass Transfer*, vol. 34, pp. 87–92, 1991.
- Nield, D. A., Convection in porous medium with inclined temperature gradient: additional results, *Int. J. Heat Mass Transfer*, vol. 37, pp. 3021–3025, 1994.
- Nield, D. A., Convection in porous medium with inclined temperature gradient and vertical throughflow, *Int. J. Heat Mass Transfer*, vol. 41, pp. 241–243, 1998.
- Nield, D. A. and Bejan, A., *Convection in Porous Media*, 2nd ed., Springer-Verlag, New York, 1999.
- Payne, L. E. and Straughan, B., Structural stability for the Darcy equations of flow in porous media, *Proc. R. Soc. London A*, vol. 454, pp. 1691–1698, 1998.
- Pop, I. and Ingham, D. B., *Convective Heat Transfer: Mathematical and Computational Modelling of Viscous Fluids and Porous Media*, Pergamon, Oxford, 2001.
- Rudraiah, N. and Kaloni, P. N., Marangoni electroconvection in the presence of an electric field in a fluid heated from above, *Acta Mech.*, vol. 166, pp. 217–229, 2003.
- Rudraiah, N., Masuoka, T., and Nair, P., Effect of combined Brinkman-electric boundary layer on the onset of Marangoni electroconvection in a poorly conducting fluid-

- saturated porous layer cooled from below in the presence of an electric field, *J. Porous Media*, vol. 10, pp. 421–434, 2007.
- Siddheshwar, P. G. and Srikrishna, C. V., Rayleigh-Bénard convection in a viscoelastic fluid filled high porosity medium with non-uniform basic temperature gradient, *Int. J. Math. Math. Sci.*, vol. 25, pp. 609–619, 2001.
- Takashima, M., The effect of rotation on electrohydrodynamic instability, *Can. J. Phys.*, vol. 54, pp. 342–347, 1976.
- Tan, W. and Masuoka, T., Stability analysis of a Maxwell fluid in a porous medium heated from below, *Phys. Lett. A*, vol. 360, pp. 454–460, 2007.
- Turnbull, R. J., Electrohydrodynamic instability with a stabilizing temperature gradient. I. Theory, *Phys. Fluids*, vol. 11, pp. 2588–2596, 1968a.
- Turnbull, R. J., Electrohydrodynamic instability with a stabilizing temperature gradient. II. Experimental results, *Phys. Fluids*, vol. 11, pp. 2597–2603, 1968b.
- Turnbull, R. J. and Melcher, J. R., Electrohydrodynamic Rayleigh-Taylor bulk instability, *Phys. Fluids*, vol. 12, pp. 1160–1166, 1969.
- Turnbull, R. J., Thermal diffusion effects on the electrohydrodynamic Rayleigh-Taylor bulk instability, *Phys. Fluids*, vol. 13, pp. 2615–2616, 1970.
- Vadasz, P., Coriolis effect on gravity-driven convection in a rotating porous layer heated from below, *J. Fluid Mech.*, vol. 376, pp. 351–375, 1998.
- Vafai, K. (Ed.), *Handbook of Porous Media*, Marcel Dekker, New York, 2000.
- Weber, J. E., Convection in porous medium with horizontal and vertical temperature gradients, *Int. J. Heat Mass Transfer*, vol. 17, pp. 241–248, 1974.



## STUDY ON THE LONGITUDINAL GAS PERMEABILITY OF JUVENILE WOOD AND MATURE WOOD

Hamid Reza Taghiyari,<sup>1,\*</sup> Ali-Naghi Karimi,<sup>2</sup> Davoud Parsapajouh,<sup>2</sup> & Kambiz Pourtahmasi<sup>2</sup>

<sup>1</sup>Wood Industries Departments, Faculty of Civil Engineering, Shahid Rajaei Teacher Training University, PO Box 13185-1898, Tehran, Iran

<sup>2</sup>Wood and Paper Science and Technology Department, Faculty of Natural Resources, The University of Tehran, Tehran, Iran

\*Address all correspondence to H. R. Taghiyari E-mail: htaghiyari@srttu.edu

Original Manuscript Submitted: 4/13/2009; Final Draft Received: 7/14/2009

The present study is aimed at longitudinal gas permeability measurement of juvenile wood and mature wood of the two most important poplar clones in Iran. Longitudinal gas permeability for juvenile wood of *P.deltoides* was  $1.50 \times 10^{-13}$ , and for its mature wood was  $28.18 \times 10^{-13} (m^3 m^{-1})$ . As for *P.euroamericana*, values were  $0.16 \times 10^{-13}$  and  $13.74 \times 10^{-13} (m^3 m^{-1})$  for juvenile and mature woods, respectively. The higher extractive content in juvenile wood in comparison with mature wood varies significantly among different clones; the maximum extractive content was measured to be 3.4% in juvenile wood of *P.euroamericana*, while the minimum (0.3%) was observed in mature wood of *P.deltoides*. A negative relationship is obvious between gas permeability values and extractive content. Vessel diameter in juvenile woods of both species tends to be lower than mature woods; maximum and minimum vessel diameters were observed in mature wood (67.3  $\mu m$ ) and juvenile wood (54.5  $\mu m$ ) of *P.deltoides*. Although vessel diameter has a great impact in gas permeability, in the present study no clear relationship was found between them. Therefore, the low permeability in the mature wood of *P.euroamericana* may be rooted in the intense settlement of extractives in the heartwood

**KEY WORDS:** extractive content, juvenile wood, longitudinal gas permeability, mature wood, poplar, porous materials, vessel diameter

### 1. INTRODUCTION

Poplar belongs to the Salicaceae family. Apart from natural species we can take benefit of special capabilities of poplar hybrids and clones. In the meantime, the world of wood industries faced a new problem having used fast-growing trees because in their first years of growth, the trees produce juvenile wood, a zone of wood extending outward from the pith. During this early growth period, the characteristics of the wood produced from year to year in each successive growth ring change markedly. During a “transition” period from 5 to 20 years of age, character-

istics of the wood produced gradually improve until they become relatively constant. This material is known as mature wood. All trees have juvenile wood, but it had little significance when the timber supply was primarily old-growth trees grown in natural forest conditions. In these trees, the juvenile wood core was small because early growth was suppressed by competition from surrounding trees. Additionally, the percentage of juvenile wood in the total volume was small because larger trees were harvested. Now, improved trees grown on intensively managed plantations reach saw-timber size and are harvested at a younger age (Dickmann, 2006). Because

diameter growth is generally greatest during the years juvenile wood is produced, the juvenile wood core may be a very significant part of the harvest.

As to the fact that many characteristics of juvenile wood differ from mature wood (Anon., 1998), the question may arise as to what extent they may differ. If the difference is statistically nonsignificant and can only be considered as a trend, that would cause no problem. But in most cases, there is a significant difference between specific characteristics in juvenile and mature woods. Since permeability is one of the most important characteristics of wood, having great impact on its utilization in different industries (such as wood preservation, wood drying, pulp, and paper), the present study is aimed at the permeability measurement of juvenile wood and mature wood of two of the most important poplar clones in Iran that have shown great compatibility with climate variability and are cultivated vastly all over Iran. It is to be noted that these two clones show suitable growth rates and have the capability to be used in different industries (Anon., 2008).

Heartwood has less extractive content, and extractive content increases with tree height (Woo et al., 2005). Permeability is different in sapwood and heartwood, as well as in different tree heights, and shows significant correlation with extractive content. Decrease in permeability toward the crown is probably due to an increase in extractive content. Koch (1996), Flynn (1995), and Rice and D'Onofrio (1996) also reported that a decrease in permeability is generally due to a more extractive content as well as blockage of vessel perforations (vessel openings) and pits. It has been proved that extractive content and pitch deposits block the way through which fluid passes along wood. Furthermore, concentration of extractive content and pitch deposits is not the same in different parts of trees. Ward (1986) reported  $230 \times 10^{-13}$  for mature wood and  $1.9 \times 10^{-13}$  ( $\text{m}^3 \text{m}^{-1}$ ) for juvenile wood of poplar. Perng et al. (1985) reported  $3.9 \times 10^{-13}$  for mature wood and  $0.28 \times 10^{-13}$  ( $\text{m}^3 \text{m}^{-1}$ ) for juvenile wood of poplar. Avramidis and Mansfield (2005) also reported an average permeability of  $22,940 \times 10^{-13}$  for mature wood and  $1,950 \times 10^{-13}$  ( $\text{m}^3 \text{m}^{-1}$ ) for juvenile wood of six poplar clones.

## 2. MATERIALS AND METHODS

### 2.1 Specimen Procurement

Disks at breast height from five trees of *Populus deltoides* (69/55) and five trees of *Populus × euroamericana* (cv. I-214) were harvested from the research site belong-

ing to the Forestry and Watershed Organization of Gilan province. It is to be noted that these clones have shown great compatibility with climate variability and are cultivated vastly in Iran. All trees were 22 years old. Geographical specifications of the region are as follows: the altitude is 10 meters below sea level and 15 meters above Caspian sea level; and  $49^\circ$  and  $57'$  eastern longitude and  $37^\circ 19'$  northern latitude. The soil was comprised of alluvial settlements and silty loam having a neutral pH to somewhat alkaline. The average annual precipitation is 1.186 mm, and the average annual temperature is  $17.5^\circ\text{C}$ ; averages for maximum and minimum temperatures are  $26.6$  and  $8.6^\circ\text{C}$ , respectively. The distinction of juvenile wood from mature wood was based on fiber length fluctuations from pith to bark. Transition from juvenile to mature wood took place at the age of 10–12 years (Taghiyari et al., 2008).

### 2.2 Gas Permeability Specimen

The longitudinal gas permeability measurement was done by an apparatus designed and built by the authors based on the microstructure porosity of wood. All gas permeability specimens were cylindrical, 18 mm in diameter and 50 mm in length. They were free from any knots, checks, and splits. The specimens were kept in a conditioning chamber to reach an MC level of 12%. Both ends of each specimen were trimmed using sharp cutter blades. Furthermore, all around each specimen was covered by silicon adhesive to prevent airflow through the radial and tangential directions. Ten specimens were cut randomly at scattered locations (five from juvenile and five from mature wood, Fig. 1). Measurements were made using the falling water displacement volume method per the instructions of Siau (1995). The connection between the specimen and holder of the apparatus was made fully airtight.

Three measurements were taken for each specimen. A superficial permeability coefficient was then calculated using Siau's equations (Siau, 1995) [Eqs. (1) and (2)]. The superficial permeability coefficients were then multiplied by the viscosity of air ( $\mu = 1.81 \times 10^{-5}$  Pa s) for the calculation of their specific permeability ( $K = k_g \mu$ ).

$$K_g = \frac{V_d C L (P_{\text{atm}} - 0.074 \bar{Z})}{t A (0.074 \bar{Z}) (P_{\text{atm}} - 0.037 \bar{Z})} \times \frac{0.760 \text{ mHg}}{1.013 \times 10^6 \text{ Pa}} \quad (1)$$

$$C = 1 + \frac{V_r (0.074 \Delta Z)}{V_d (P_{\text{atm}} - 0.074 \bar{Z})} \quad (2)$$

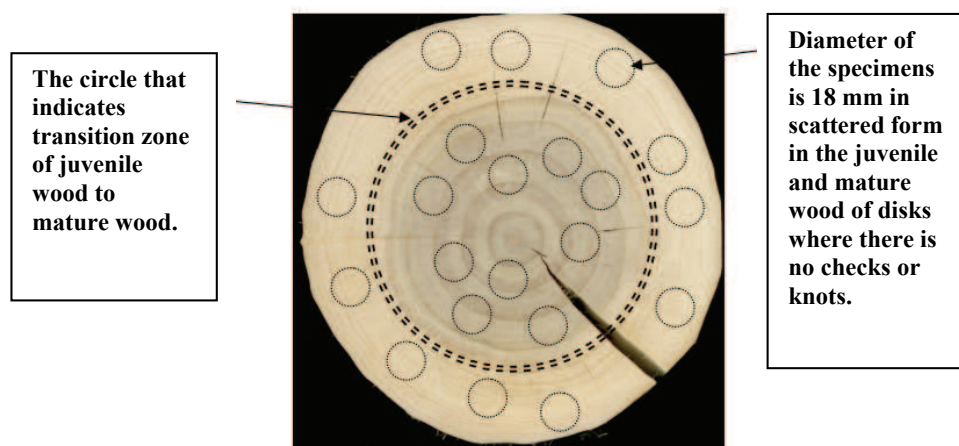


FIG. 1: Position of juvenile wood and mature wood in the disk and location of sampling

where:

$k_g$  = longitudinal specific permeability,  $m^3/m$

$V_d = \pi r^2 \Delta z$  [ $r$  = radius of measuring tube (m)],  $m^3$

$C$  = correction factor for gas expansion as a result of change in static head and viscosity of water

$L$  = length of wood specimen, m

$P_{atm}$  = atmospheric pressure, m Hg

$\bar{z}$  = average height of water over surface of reservoir during period of measurement, m

$t$  = time, s

$A$  = cross-sectional area of wood specimen,  $m^2$

$\Delta z$  = change in height of water during time  $t$ , m

$V_r$  = total volume of apparatus above point 1 (including volume of hoses),  $m^3$

### 2.3 Extractive Content

The extractive content was determined according to the standard T 280 pm-99 (TAPPI, 1999). First, juvenile wood and mature wood of each disk were separated and then ground in a Palmann mill to pass through screens of 40 mesh and 60 mesh. The ground wood was then Soxhlet extracted with acetone for 8 h. The total weight of extractable components was determined gravimetrically and expressed as a percentage of the original weight of the wood specimen.

### 2.4 Vessel Diameter

For the vessel diameter, five blocks of  $2 \times 2 \times 2$  cm from juvenile wood and five from mature wood of each tree were taken and kept in distilled water for 48 h. Transverse sections of 20–25  $\mu m$  in thickness were cut by a Jung Heidelberg slicing microtome. The sections were stained with safranin and then dehydrated in a graded series of ethanol (50%, 75%, and 96%), and then in xylol to make them ready to be mounted on microscopic slides. The measuring procedure covered all vessels from spring wood to summer wood. Each vessel was measured in the radial as well as tangential directions (Fig. 2).

### 2.5 Statistical Analysis

A statistical analysis was conducted using SAS software program, version 9.1. A two-way analysis of variance (ANOVA) was performed to conclude the significant difference at a 99% confidence level.

## 3. RESULTS

### 3.1 Longitudinal Gas Permeability

The average longitudinal specific gas permeability of *Populus deltoids* (69-55) is  $1.50 \times 10^{-13}$  ( $m^3 m^{-1}$ ) for juvenile wood and  $28.18 \times 10^{-13}$  ( $m^3 m^{-1}$ ) for mature wood; whereas the averages for *Populus x euroamericana* (cv. I-214) show  $0.17 \times 10^{-13}$  ( $m^3 m^{-1}$ ) for juvenile wood and  $13.75 \times 10^{-13}$  ( $m^3 m^{-1}$ ) for mature wood. The statistical analysis shows a significant difference between the permeability of juvenile and mature wood of

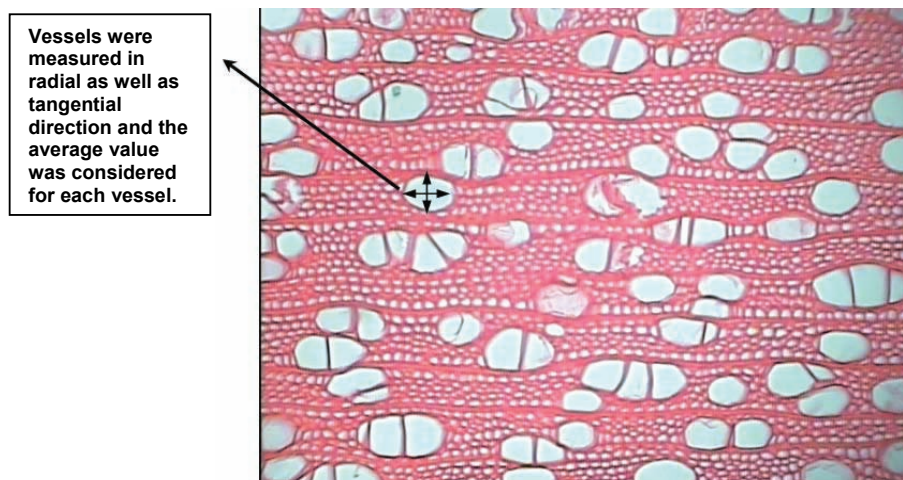


**FIG. 2:** Value for each vessel was obtained through tangential and radial measurements of the vessel

these two clones, as well as these two clones with each other. Figure 3 shows the permeability amount in juvenile and mature wood of the two clones measured in the present study.

### 3.2 Extractive Content

The results of the extractive analysis are shown in Fig. 4. The statistical analysis show a significant difference at an  $\alpha$  level of 1% between juvenile wood and mature wood of these two clones. Furthermore, there is also a significant

difference at an  $\alpha$  level of 1% between juvenile wood of *P. deltooides* and *P. × euroamericana*, as well as between mature wood of *P. deltooides* and *P. × euroamericana*. The extractive content of the juvenile wood in *P. × euroamericana* was the greatest (3.4%), whereas in the mature wood of *P. deltooides* was the lowest (0.3%) (Table 1).

### 3.3 Vessel Diameter

The results of vessel diameter are shown in Fig. 5. Statistical analysis shows a significant difference between juve-

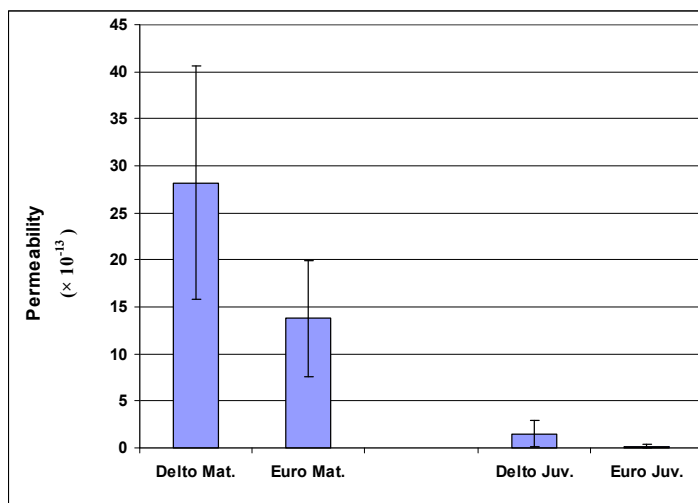


**FIG. 3:** Permeability values ( $\times 10^{-13} \text{ m}^3 \text{ m}^{-1}$ ) for juvenile wood and mature wood in *P. deltooides* and *P. × euroamericana*

**TABLE 1:** Comparison between different variables measured in the present study: permeability ( $\times 10^{-13} \text{ m}^3 \text{ m}^{-1}$ ), extractive content (%), vessel diameter ( $\mu\text{m}$ )

Kind of wood	Permeability ( $\times 10^{-13} \text{ m}^3 \text{ m}^{-1}$ )	Extractive content (%)	Vessel diameter*** ( $\mu\text{m}$ )
<i>P*. deltoides</i> mature**	28.18	0.3	67.3
<i>P. ×euroamericana</i> mature	13.75	0.35	61.6
<i>P. deltoides</i> juvenile	1.5	0.75	54.5
<i>P. ×euroamericana</i> juvenile	0.17	3.4	57.4

\**Populus*

\*\*Wood

\*\*\*Diameter

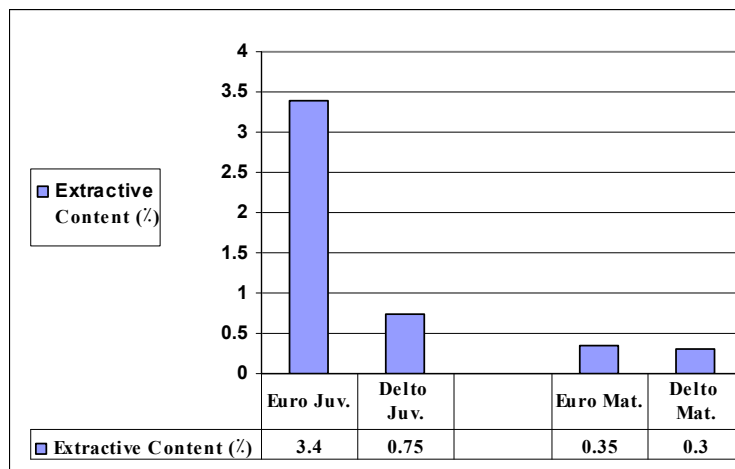


**FIG. 4:** Extractive content (%) of juvenile wood and mature wood for *P. deltoides* (69/55) and *Populus × euroamericana* (cv. I-214)

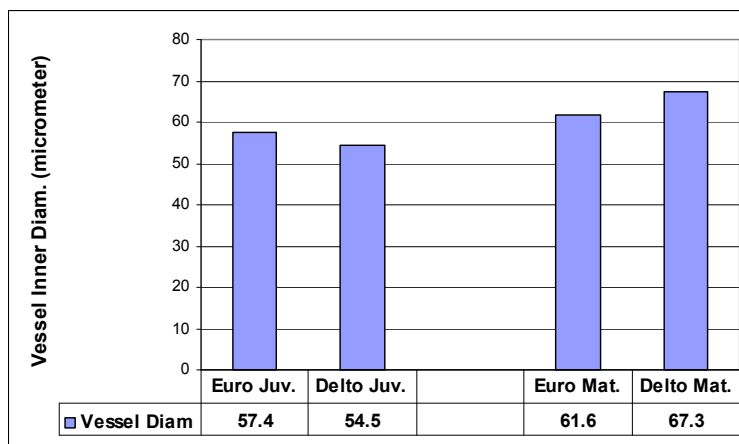


**FIG. 5:** Vessel diameter ( $\mu\text{m}$ ) of juvenile wood and mature wood for *P. deltoides* (69/55) and *Populus × euroamericana* (cv. I-214)

nile wood and mature wood in both clones; but no significant difference was observed between *P. deltooides* (69/55) and *P. × euroamericana* (cv. I-214). Vessel diameter in mature wood of *P. deltooides* was the highest (67.3  $\mu\text{m}$ ) and in juvenile wood of *P. deltooides* was the lowest (54.5  $\mu\text{m}$ ) (Table 1). No significant difference was seen between the two clones.

A summary of the three variables measured in the present study is shown in Table 1.

#### 4. DISCUSSION

In all cases, the permeability of juvenile wood is far below that of mature wood; causes can be rooted in more extractive content, tyloses, and pitch deposits that may block the pits and vessel perforations (Woo et al., 2005; Koch, 1996; Flynn, 1995; Rice and D'Onofrio, 1996; Ward, 1986). Extractives have a significant impact on the permeability of wood, although they make up only a small percentage of the total chemical composition of it. Ward (1986) indicated that the blockage of pits and openings is due to extractives and tyloses on the way of fluid transfer. Vologdin et al. (1979) also noticed that permeability increased progressively with the removal of extractives (phenolics). Furthermore, Perre and Karimi (2002) reported that permeability increases significantly as the length of specimens is shortened. Error bars in Fig. 3 imply that the concentration of extractives varies in different parts of a tree and therefore permeability values would also vary significantly. Putting permeability values and extractive contents of juvenile wood and mature

wood of these two clones in one single figure can show us the reverse relationship between them (Fig. 6).

Comparison between the extractive content of the present study for 22-year-old trees with those of previous studies at the age of 18 that were cut and cultivated from the same site but four years earlier (Mahdavi Feizabadi, 2003) shows that in *P. deltooides*, not much difference in extractive content was made during the four last years of growth. But in *P. × euroamericana*, a comparison with previous studies that was done on 18-year-old trees of the same inhabitant (Rasooli Garmaroudi, 2002) shows a great difference. This difference is most probably made by the process of changing sapwood to heartwood. Therefore, if the end utilization needs to have high permeability or low extractive content, trees of *P. × euroamericana* should be cut before the age of about 18 years.

Statistical analysis showed a significant difference between the vessel diameter of juvenile wood and mature wood in both clones. However, no significant difference was found between vessel diameters of juvenile woods or mature woods of the two clones. Poiseuille's law of viscous flow, which applies to gases through hardwood vessels, proves there is a positive relationship between the permeability value and the fourth exponent of the radius of capillary (radius of vessels) [Eq. (3)] (Siau, 1971).

$$k_L = \frac{n\pi R^4}{8\eta} \times 1.013 \times 10^6 \quad (3)$$

where

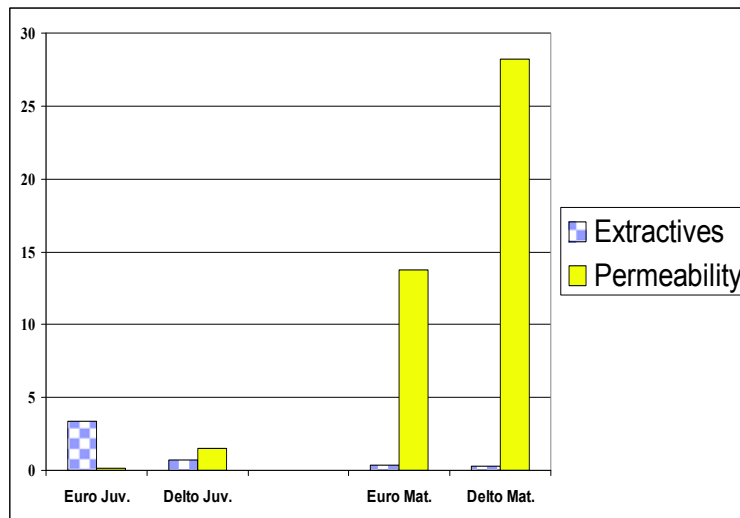


**FIG. 6:** Reverse relationship between longitudinal gas permeability ( $\times 10^{-13} \text{m}^3 \text{m}^{-1}$ ) and extractive content (%)

$k_L$  = longitudinal permeability,  $\text{cm}^3$  (fluid)  $\text{cm}^{-1}$   $\text{atm}^{-1} \text{s}^{-1}$

1 atm =  $1.013 \times 10^6$  dyne  $\text{cm}^{-2}$

$R$  = radius of vessels, cm

$n = N/A$  = number of vessels per  $\text{cm}^2$  of cross section

$\eta$  = viscosity of fluid, (dyne sec)  $\text{cm}^{-2}$

The fourth exponent of the radius implies that a slight increase or decrease in the value of the vessel radius may have a high impact on the value of permeability, although statistical methods do not show a significant difference. Putting all this information together, we may conclude that theoretically the juvenile wood of both clones should have nearly the same permeability values based on an insignificant difference between their vessel diameter; but practical measurement showed a great difference. Therefore, we can come to the conclusion that the extractive content between these two plays a more important role in the value of longitudinal gas permeability. Figure 7 shows all three factors of longitudinal gas permeability, extractive content, and vessel diameter together.

### 5. CONCLUSION AND FUTURE WORK

The permeability of juvenile wood is always less than that of mature wood in sound wood. The reasons for this may be rooted in several factors such as blockage of vessels

by more extractive content, tyloses, and pitch deposits in juvenile wood, as well as less vessel diameter in juvenile wood. Regarding the insignificant difference between vessel diameter in the juvenile wood of *P. deltoides* and *P. × euroamericana*, the high difference between the permeabilities of these two may be traced to their difference in extractive content.

Juvenile wood of *P. × euroamericana*, especially in its older ages, tends to have an extra amount of extractives and therefore is prone to have very low permeability. Consequently, it is not recommended for industries where permeability is important.

Due to the smallness of the specimens, it was not possible to measure the extractive content in each single one. Still, the corresponding author is working on the extractive measurement in every single specimen to find out the regression equation between gas permeability and extractive content.

### ACKNOWLEDGMENT

The authors are grateful to The Center of Excellence of Applied Management of Fast-Growing Wood Species for preparing the budget for the present study.

### REFERENCES

Anon., Properties of Juvenile Wood, U.S. Department of Agriculture, Forest Service, Forest Products Laboratory, VI-7, 09, 1998.

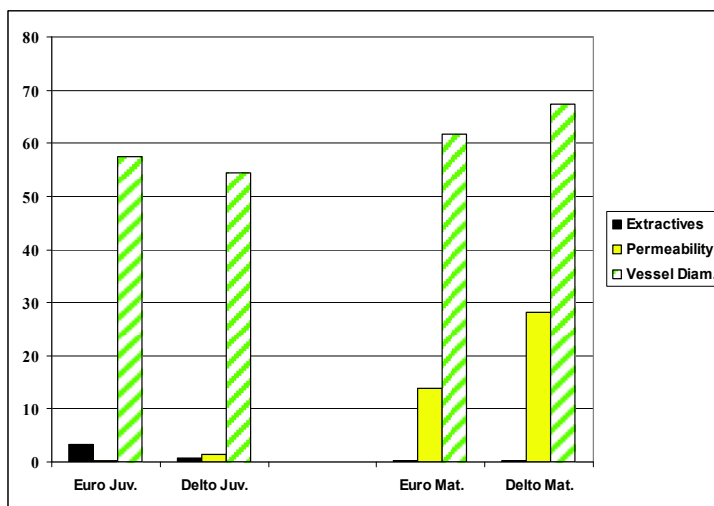


**FIG. 7:** Comparison among permeability ( $\times 10^{-13} \text{ m}^3 \text{ m}^{-1}$ ), extractive content (%), and vessel diameter ( $\mu\text{m}$ ) in juvenile wood and mature wood of *P. deltoides* and *P. × euroamericana*

- Anon., Annual Report, The Forestry and Watershed Organization of Iran, Gilan Province, 2008.
- Avramidis, S. and Mansfield, S. D., On physical properties of six aspen clones, *Holzforschung*, vol. 59, pp. 54–58, 2005.
- Dickmann, D. I., Silviculture and biology of short-rotation woody crops in temperate regions: Then and now, Department of Forestry, Michigan State University, E. Lansing, 2006.
- Flynn, K., A review of the permeability, fluid flow, and anatomy of spruce (*Picea* spp.), *Wood Fiber Sci.*, vol. 27, no. 3, pp. 278–284, 1995.
- Koch, P., *Lodgepole Pine in North America* Madison, Wisconsin, Forest Products Society; pp. 35–45, 213–318, 667–695, 927–940, 1029–1041, 1996.
- Mahdavi Feizabadi, S., Investigation on utilization of *Populus deltoides* and *Eucalyptus camaldulensis* for newsprint and printing paper, PhD Thesis, Faculty of Natural Resources, The University of Tehran, 2003.
- Perng, W. R., Brebner, K. T., and Schneider, M. H., Aspen wood anatomy and fluid transport, *Wood Fiber Sci.*, vol. 17, no. 2, pp. 281–289, 1985.
- Perre, P. and Karimi, A., Fluid migration in two species of beech (*Fagus silvatica* and *Fagus orientalis*): A percolation model able to account for macroscopic measurements and anatomical observations, *Maderas, Ciencia Tecnol.*, vol. 4, no. 1, pp. 50–68, 2002.
- Rasooli Garmaroudi, I., Study on the possibility to use poplar instead of beech mixed with blue beech for chemical-mechanical newspaper pulping, MS Thesis, Faculty of Natural Resources, Tarbiat Moddares University, 2002.
- Rice, R. W. and D’Onofrio, M., Longitudinal gas permeability measurements from eastern white pine, red spruce, and balsam fir, *Wood Fiber Sci.*, vol. 28, no. 3, pp. 301–308, 1996.
- Siau, J. F., *Flow in Wood*, Syracuse University Press, New York, 1971.
- Siau, J. F., Wood: Influence of moisture on physical properties, Dept. of Wood Science and Forest Products, Virginian Polytechnic Institute and State University, Blacksburg, 1995.
- Taghiyari, H. R., Parsapajouh, D., Karimi, A. N., and Pourtahmasi, K., Evaluation of fiber characteristics in the juvenile wood and mature wood of *Populus deltoides* (69) and *Populus × euroamericana* (214), Grown in Gilan Province, Iran, *Iran. J. Natural Resour.*, vol. 61, no. 3, pp. 713–722, 2008.
- TAPPI standard, T 280 pm-99, Acetone Extractives of Wood and Pulp, 1999.
- Vologdin, A. I., Razumova A. F., and Charuk, E. V., Importance of extractives for permeability of pine and spruce woods, *Holztechnologie*, vol. 20, no. 2, pp. 67–69, 1979.
- Ward, J. C., The effect of wetwood on lumber drying times and rates: An explanatory evaluation with longitudinal gas permeability, *Wood Fiber Sci.*, vol. 18, no. 2, pp. 288–307, 1986.
- Woo, K. L., Watson, P., and Mansfield, S. D., The effects of mountain pine beetle attack on lodgepole pine wood morphology and chemistry: Implications for wood and fiber quality, *Wood Fiber Sci.*, vol. 37, pp. 112–126, 2005.



## WETTABILITY EFFECTS IN GAS GRAVITY—ASSISTED FLOW AS RELATED TO DISPLACEMENT INSTABILITY

B. Rostami,<sup>1,2</sup> R. Kharrat,<sup>1</sup> V. Alipour Tabrizy,<sup>1</sup> M. Khosravi,<sup>3</sup>  
& C. Ghotbi<sup>2</sup>

<sup>1</sup>Petroleum University of Technology, Tehran Research Center, Ghasemi Zadian St.—Satarkhan St., Tehran 1453953111, Iran

<sup>2</sup> Sharif University of Technology, Azadi Avenue, Tehran 1458889694, Iran

<sup>3</sup> EOR Research Institute of NIOC, No. 22, Negar Valley, Valiasr St.- Tehran 19698113771, Iran

\*Address all correspondence to B. Rostami E-mail: Rostami@che.sharif.ir

Original Manuscript Submitted: 3/3/2009; Final Draft Received: 6/24/2009

*The drainage of oil under gravity forces is an efficient method because it can farther reduce the remaining oil saturation to below that obtained after water flooding. This paper describes a series of visual experiments under forced gas invasion with special attention to the effects of wettability. From oil production history and image analysis, we examine a threshold criterion for displacement stability that is consistent with the results of gradient percolation theory. The effect of the destabilized front velocity on oil recovery and residual saturation is investigated for both wettability conditions. Different recovery rates occur with different fluid morphologies, which depend on the matrix wettability and the balance between gravity and viscous and capillary forces. The dimensionless capillary and gravity numbers are used in analyzing the results. It has been shown that oil production decreases with displacement instability; however, this behavior would extremely depend on the wetting state. In addition, results indicated that the oil recovery depends linearly on the ratio of the gravity to viscous forces; however, the slope of this relationship in oil-wet porous media is more than twice of the water-wet system.*

**KEY WORDS:** *wettability, gravity forces, capillary forces, viscous forces, dimensionless numbers, displacement stability*

### 1. INTRODUCTION

Immiscible displacement of fluids in porous media occurs in a wide range of flow regimes that reflect the interactions between capillary, gravity, and viscous forces. Experiments performed on artificial porous media (Fourar et al., 1993; Persoff and Pruess, 1995) as well as pore network simulations (Hughes and Blunt, 2000; Singh and Mohanty, 2003; Tsakiroglou et al., 2005; Theodoropoulou et al., 2008) have revealed that the transient and steady-state two-phase flow patterns depend not only on

the specific characteristics of the pore space morphology, but also on a variety of dimensionless parameters such as the capillary number, viscosity ratio, and wettability state. In this study, we have focused on the relationship between wettability and displacement instability (in terms of capillary number) during the gas gravity–assisted flow in porous media.

Several studies have focused on the effects of wettability in gravity drainage (Oren and Pinczewski, 1994; Vizika and Lombard, 1996; Grattoni et al., 2001; Pedrera et al., 2002; Shahidzadeh et al., 2004). Some stud-

ies demonstrate that in drainage experiments, saturation of the retained liquid decreases with increasing the contact angle (Kewen and Firoozabadi, 2000; Morrow and MacCaffery, 1978), whereas other researchers show the importance of a hydraulic continuity for achievement of maximum recovery (Oren and Pineczewski, 1994; Blunt et al., 1995; Vizika and Lombard, 1996; Zhou and Blunt 1998). Surprising data are also reported by Pedrera et al. (2002) and Caubit et al. (2004). They claimed that residual oil saturation decreases when the cores become more oil wet. In contrast, other authors (e.g., Vizika and Lombard, 1996) showed that for positive spreading, residual oil increases when the wettability index decreases. While the majority of the researches have been focused on the wetting behavior under stabilized gravity drainage (in the absence of viscous instability), the relationship of wettability and macroscale hydrodynamics has not been reviewed.

For gas-oil gravity drainage with high viscosity contrast, where the interplay between capillary, gravity, and viscous forces controls the invasion front movement, identification of the relationship between fluid-solid interactions (wettability) and prevailing forces is necessary. Investigations based on gradient percolation theory (Wilkinson, 1986; Xu et al., 1998; Meheust et al., 2002; Lovoll et al., 2005) suggest the importance of the invasion front instability during the fluid flowing in porous media. They showed that when the viscosity of the injected fluid is less than that of the displaced phase, viscous fingering dominates and the oil trapping and bypassing will be occurred.

In addition, a number of investigations have been carried out to correlate dynamic transport functions and fluid distribution with flow regime conditions. Skauge et al. (1997) conducted a series of centrifuge and gas flood experiments and found a more dispersed gas front and lower recovery efficiency at higher gas flow rates. Edwards et al. (1998) showed differences between oil recovery by processes where gravity controls the flood front and by those where the gravitational forces play a less significant role in the ultimate fluid distribution.

In this paper, experimental results are obtained in vertical long core and synthetic porous media under different wettability states. In each media, transitions from stabilized and destabilized flow configurations were studied. In order to check under which circumstance the stabilization occurs, the evolution of the front instability is investigated and compared to the gravity invasion percolation theory. Then, the influence of the displacement instability on oil recovery is compared for different wettability con-

ditions. In addition, the impacts of capillary and gravity numbers on oil production history have been reviewed.

## 2. EXPERIMENTAL DESCRIPTIONS

### 2.1 Porous media and Fluids

Forced gravity drainage experiments have been performed in synthetic porous media (glass beads with average grain size of 150  $\mu\text{m}$ ). The average porosity was around 37% and the absolute permeability ranged between 7 and 10 Darcy. These unconsolidated packs provide a simplistic representation of the main flow characteristics of reservoir rock, and have the additional merit of being transparent, so that the movement of the fluid can be detected. Moreover, experiments were performed under a reasonable ranges of dimensionless numbers; thus, the conclusions could be independent of high values of porosity and permeability.

The glass beads are initially water wet, but the wettability is changed to oil wet by treating them with three methylchloro-silane. The wettability changes when a thin film of this water-repellent solution coats the glass beads surface. The effects of silanization on glass beads and wettability alteration have been observed by several investigators (Vizika and Lombard, 1996; Grattoni et al., 2001; Shahidzadeh et al., 2004). The porous media characteristics for each experiment are given in Table 1.

Fluids properties were measured using standard techniques and are given in Table 2. The gas phase was pure nitrogen. The aqueous phase, always referred as the water phase, was distilled water, and the oil phase was normal decane. A small amount of hydrocarbon-soluble dye was added to the oil phase in order to distinguish the wetting phase and nonwetting phase during the experiments.

### 2.2 Experimental Apparatus and Procedure

A schematic drawing of the equipments used in the laboratory is shown in Fig. 1. The complete experimental setup includes the long cylindrical visual model, the fluid injection system, a differential gauge pressure, the effluent collection system, a gas cylinder, a digital camera, and the data acquisition system.

A cylindrical plate made up of Plexiglas was used in this study. The Plexiglas physical model was easy to design and it is a relatively more transparent material for visual observations. The differential gauge pressure was fitted to the inlet port. High-precision pumps were used to inject liquids. A mass flow controller (MFC) was used to inject gas at the specific flow rates. A two-phase separator

**TABLE: 1** Summary of experiments properties

Wettability state	Water wet			Oil wet		
	1	2	3	1	2	3
Experiment number	1	2	3	1	2	3
Length (cm)	60	60	60	60	60	60
Cross-sectional area (cm <sup>2</sup> )	7.07	7.07	7.07	7.07	7.07	7.07
Porosity (fraction)	0.382	0.39	0.395	0.377	0.357	0.39
Absolute permeability (Darcy)	9.3	9.8	9.2	8.5	7.95	7.75
Oil in place (cm <sup>3</sup> )	140	144	145	150	138	155
Irreducible (Irred) water saturation (%PV)	0.137	0.128	0.134	0.07	0.092	0.06
Oil permeability at Irreducible water saturation (Swi) (Darcy)	4.6	5.5	4.8	4.1	3	3.3
Injection rate (cm <sup>3</sup> /min)	1.85	3.4	5.8	2.3	3.3	6.25

**TABLE: 2** Properties of fluids used (at 25°C)

Fluid system	Mass density (Kg/m <sup>3</sup> )	Viscosity (cP)
Nitrogen	1	0.02
Normal decane	740	0.85
Distilled water	1000	1

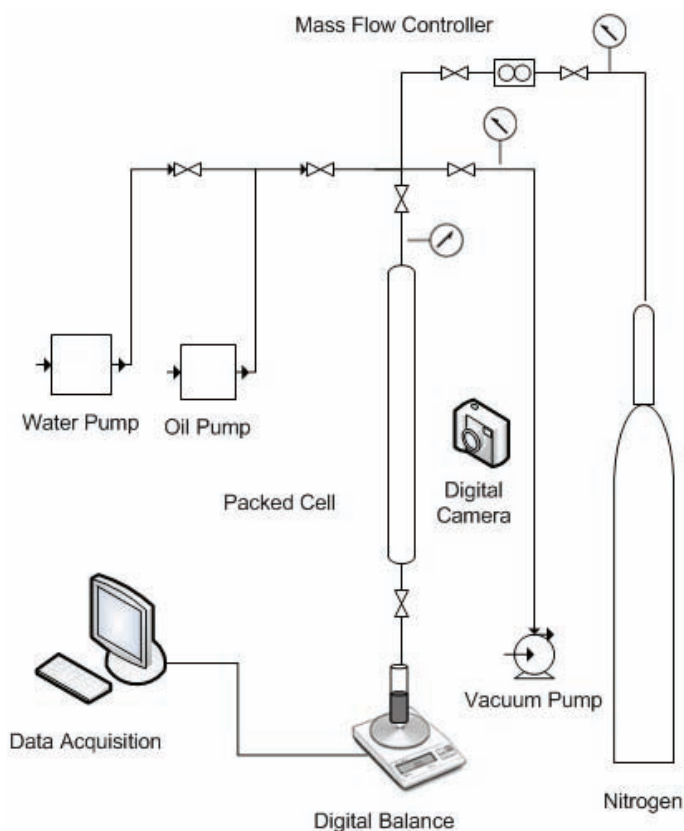


**FIG. 1:** Schematic drawing of the laboratory experimental setup

was located at the production end. An incremental weight measurement method using a digital computer-controlled balance was used to measure the effluent production data. Displacement structures were recorded at regular intervals during the experiments using a digital camera. These raw pictures were filtered in order to clearly separate the wetting phase from the nonwetting phase. Successive steps of the filtering process are shown in Fig. 2.

The experiments were conducted under ambient laboratory pressure and temperature. For each experiment, the model was placed in a vertical gravity stable position and a leak test was performed. Then, the sintered packed column was first evacuated and then fully saturated with water. Thereafter, the porosity and absolute permeability were measured. The porous media was then flooded with oil to irreducible water saturation and the effective permeability was measured. Thereafter, gas was injected into the model from the top and oil was produced from the bottom.

### 3. RESULTS AND DISCUSSION

Two groups of displacement experiments with different wettability characteristic were performed at the ambient conditions. Injection rates were varied in each group. The major parameters and results from the experiments are summarized in Table 3.

#### 3.1 Invasion under Gravity Forces

In order to check under which circumstances stabilization occurs, the evolution of the displacement front in the flow direction is investigated. In the gas gravity drainage experiments, when gravity forces dominate viscous forces, the invasion of a nonwetting phase into a wetting liquid

is stable. This could be understood by using a combination of Darcy's law and a mapping to percolation theory (Lovoll et al., 2005).

For top-down drainage with high viscosity contrast between gas and oil, a number of investigations carried out in laboratories (e.g., Hagoort, 1980) suggest the following criterion for the displacement under a stabilized condition:

$$v_c > v \quad (1)$$

where  $v_c$  is the critical gravity drainage velocity defined by Blackwell and Terry (1959) and Dumore (1964),

$$v_c = \frac{k\Delta\rho g}{\Delta\mu} \quad (2)$$

where  $\Delta\rho$  and  $\Delta\mu$  are the density and viscosity differences between two fluids, respectively, and  $k$  is the effective permeability.

This criterion represents the situation in which the negative effects of viscous forces are overcome by gravity forces. This definition is also in line with the theoretical argument based on percolation theory (Wilkinson, 1984; Stauffer and Aharony, 1991) in a stabilizing gradient. This theory predicts the following scaling law for the displacement under gravity (Xu et al., 1998; Meheust et al., 2002):

$$w \approx (N_B - N_c)^{-(\alpha/1+\alpha)} \quad (3)$$

where  $w$  is the invasion front width and  $\alpha$  is the correlation length exponent in percolation theory. Meheust et al. (2002) and Lovoll et al. (2005) described the generalized Bond number,  $N_B^* = N_B - N_c$ , and showed that when  $N_B^* \rightarrow 0$ , the front width  $w$  in Eq. (3) diverges. Hence, the following criterion was proposed for interface stabilization:

$$N_B - N_c = N_B^* > 0 \quad (4)$$

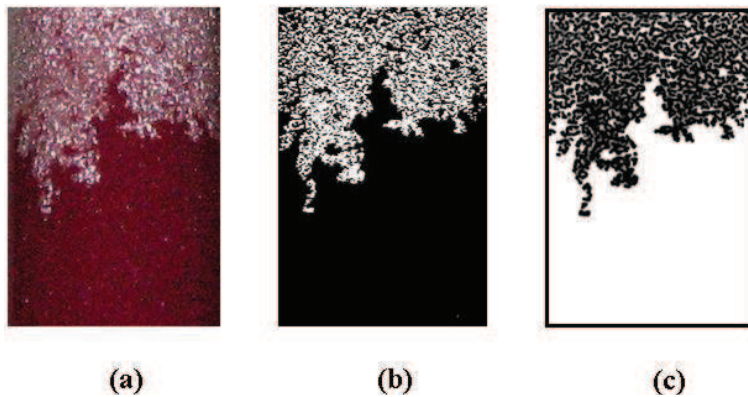


FIG. 2: Image filtering process: a) the raw image; b) black-and-white image; c) image in reverse color

**TABLE: 3** Summary of key results from displacement experiments

Wettability state	Water wet			Oil wet		
	1	2	3	1	2	3
Experiment number	1	2	3	1	2	3
Capillary number ( $10^{-6}$ )	1.68	3.1	5.3	2.3	3	5.7
Gravity number ( $10^{-6}$ )	0.9	0.55	0.3	0.55	0.33	0.19
Breakthrough time (min)	33.5	12.5	8	29	12.5	6.5
Oil recovery at breakthrough time (%OIP)	48.5	41.2	33.5	47.8	30.5	23.8
Oil recovery at two pore volume injection (%OIP)	68.2	62.5	57.2	68.5	55.0	52.2
Oil recovery at four pore volume injection (%OIP)	74.1	69.3	63.8	72.3	62.2	58.6
Final oil recovery (%OIP)	85.6	84.2	81.8	84.5	81.2	76.5

After substitutions and rearrangements, the classical criterion was achieved as

$$\Delta\rho gk/\mu_o > v \quad (5)$$

This relation is the same as Eq. (1). The validity of the above criterion [Eq. (1) or (5)] can be confirmed using the visual observations of gas invasion shown in Fig. 3. In this figure, *a* and *b* correspond to displacement velocities that are approximately 1.1 and 3.3 times higher than the critical velocity. According to Fig. 3, when the above criterion is reached, the displacement front has a more stable form. In contrast, when the displacing velocity exceeds the critical velocity, the displacement front diverges.

### 3.2 Displacement Instability

Different displacement velocities significantly control the fluid flow morphologies for the three-phase system, depending on the fluid-solid interaction (wettability) and viscosity ratio. In this section, the results from stabilized and destabilized displacement experiments are investigated for both wettability conditions.

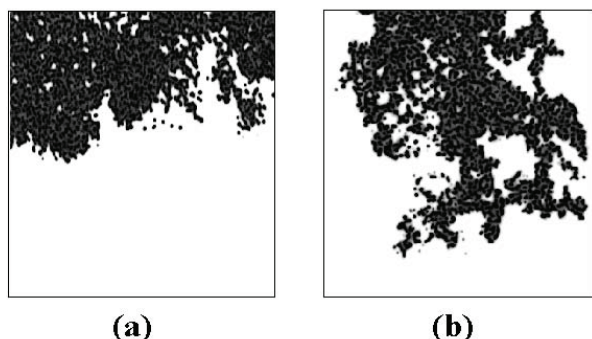


**FIG. 3:** Front stability analysis from displacement structures for configuration of **a**) slow displacement and **b**) viscous fingering under gravity

Figure 4 shows the results from displacement experiments for wettability conditions at different steps of production life. The plots correspond to the quantity of drained oil as a function of injected pore volume. Results indicate that the dependency of the oil recovery on displacement velocity decreases by increasing the production life. A sharp reduction is related to the oil recovery at breakthrough time due to the high front movement, discontinuity in the oil phase, and viscous fingering. Obviously, both water-wet (Fig. 4a) and oil-wet (Fig. 4b) systems exhibited a similar response to increasing gas injection velocity, i.e., early gas breakthrough time and a considerable tail production of oil, but lower total oil recovery. Figure 4 also indicates that the oil recovery from an oil-wet system is much more sensitive to increasing of the injection rate.

It is found that under forced gas invasion, the velocity and shape of the gas front are controlled by gravity, capillary, and viscous forces. During the first stage of oil production, corresponding to a bulk flow, gas invades the larger pores, resulting in a small capillary force; hence, the oil production is mostly controlled by the balance between gravity and viscous forces. This period is short and most of the oil in place could be produced if the flow is gravity dominated. At the second stage, corresponding to a film flow, the capillary pressure dominates the process at very low wetting phase saturation. This stage has a very long tail that lasts several hours or days, with very low oil production rate. For both wettability conditions, as the injection rate increases, the amount of additional oil recovery after breakthrough time becomes an important fraction of the total oil recovery.

In water-wet porous media, the continuity of oil is maintained along the porous media because it is spreading. Water is not mobilized but wets the pore walls and it is also continuous. In an oil-wet porous media, water is the nonwetting phase and occupies the center of pores in the

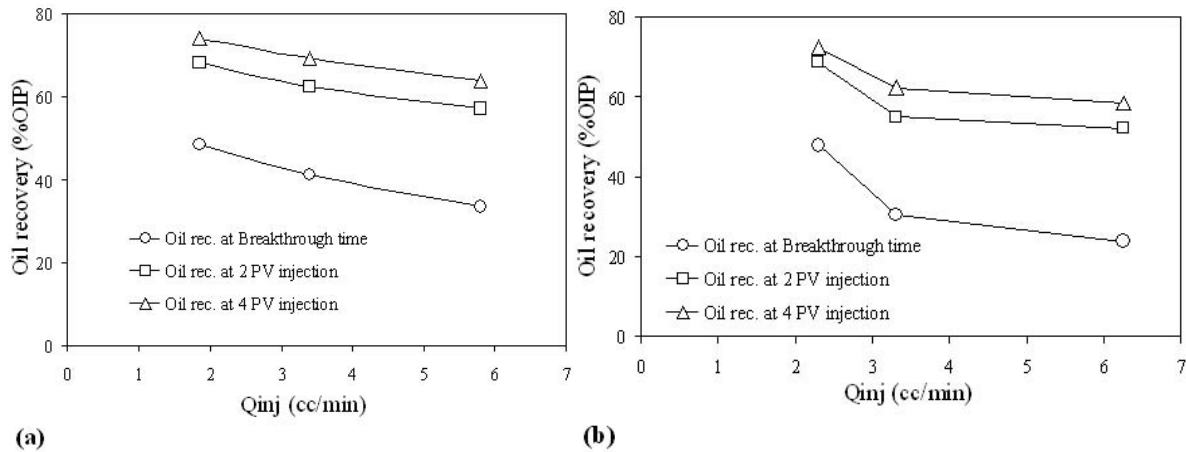


FIG. 4: Dependency of the displaced oil recovery on the injection flow rate for a) water wet and b) oil wet

form of discontinuous droplets, while oil is the wetting phase and occupies the corners of the media. During the flowing in oil-wet media, oil flows through wetting films, gas flows principally as continuous nonwetting filaments, and water flows in the form of isolated ganglia.

### 3.3 Dimensional Analysis

Scaling of miscible and immiscible displacement in porous media using dimensionless groups not only reduces the number of parameters to be studied, but also facilitates in effectively capturing the multiphase mechanisms and fluid dynamics operative in these processes (Shook et al., 1992). In forced gravity drainage flow, the type of displacement not only depends on the relative magnitude of viscous and gravity forces, but also on their relative magnitude with respect to the heterogeneous capillary forces. In the following, dimensionless capillary and gravity numbers are proposed to quantify the relative magnitudes of the prevailing forces.

*Capillary number:* In fluid dynamics, the capillary number represents the relative effect of viscous forces versus surface tension acting across an interface between two immiscible fluids. It is defined as

$$N_c = \frac{\mu_w v}{\sigma} \quad (6)$$

where  $\mu_w$  is the wetting phase viscosity,  $v$  is a characteristic velocity, and  $\sigma$  is the surface or interfacial tension between the two fluid phases. For low capillary numbers (a rule of thumb says less than  $10^{-5}$ ), flow in porous media is dominated by capillary forces.

In any gas injection process, the mobility ratio is typically unfavorable and the development of unstable fingers during gas displacement is imperative. High rate gas injection may result in unstable front movement and oil bypassing.

Figure 5 shows the relationship between capillary number and oil recovery for different wettabilities after two pore volumes of gas injection. Increasing in capillary number has a negative effect on the remaining oil saturation, which results in poor sweep efficiency. This behavior is mostly pronounced at early times (e.g. breakthrough time) because the hydraulic connectivity in the oil phase is lost and oil bypassing and trapping events occur quickly in high rapid flow experiments. In later times, part of the bypassed oil could be recovered by injecting a

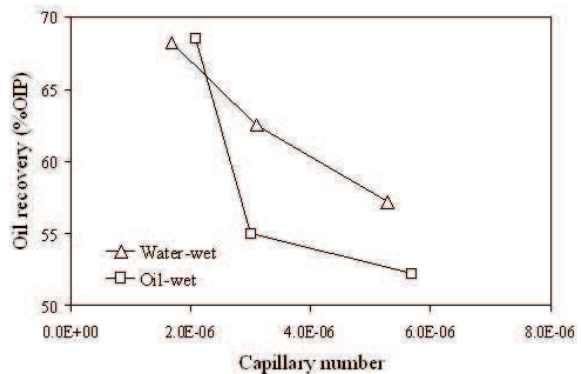


FIG. 5: Oil recoveries at two pore volumes of injection against capillary number at various wettability states

high amount of gas; however, it may not be economically feasible to recover that oil.

Figure 6 shows the distribution of the gas and oil recorded at regular intervals during the experiments at two different gas injection rates in water-wet porous media. At the lower injection rate (Fig 6a) the flood front is quite stable, while at the higher rate (Fig. 6b) considerable bypassed oil is left behind the gas front. This observation is consistent with threshold criterion for displacement stability. In the following, analyses of the experimental results are continued in terms of gravity number.

*Gravity number:* The gravity number represents the balance between viscous and gravity forces. This group accounts for the ratio of the critical gravity drainage velocity to the gas displacement velocity,

$$N_g = \frac{v_c}{v_{inj}} = \frac{k_o \Delta \rho_{og} g}{v \mu_o} \quad (7)$$

where  $\mu_o$  is the oil phase viscosity,  $v$  is a displacement velocity,  $\Delta \rho_{og}$  is the density differences between the two fluid phases, and  $k_o$  is the effective permeability to oil.

Figure 7 shows the relationship between gravity number and oil recovery for different wettabilities. Results in Fig. 7a indicate that the oil recovery at breakthrough time is higher for an oil-wet system when the gravity number is large (higher displacement efficiency and lower injection rate). This confirms that the existence of a strong conductive film of oil through the pore walls in oil-wet porous media. However, as the time passes and recovery increases, differences in oil production are reduced between various porous media. This shows that the oil production in an oil-wet system is reduced when the film flow is dominant (Fig. 7b). At a later time, the capillary force dominates other forces, and the film flow controls the success of the process. In a completely water-wet pore, water as the wetting phase occupies the corners; gas as the most nonwetting phase occupies the center; oil as the intermediate wetting phase stays between the gas and water as a conductive film; and the high oil recovery could be achieved from this film. For an oil-wet pore, oil is the wetting phase and occupies the corners. Oil recovery from the corners of pores is certainly lower than the oil

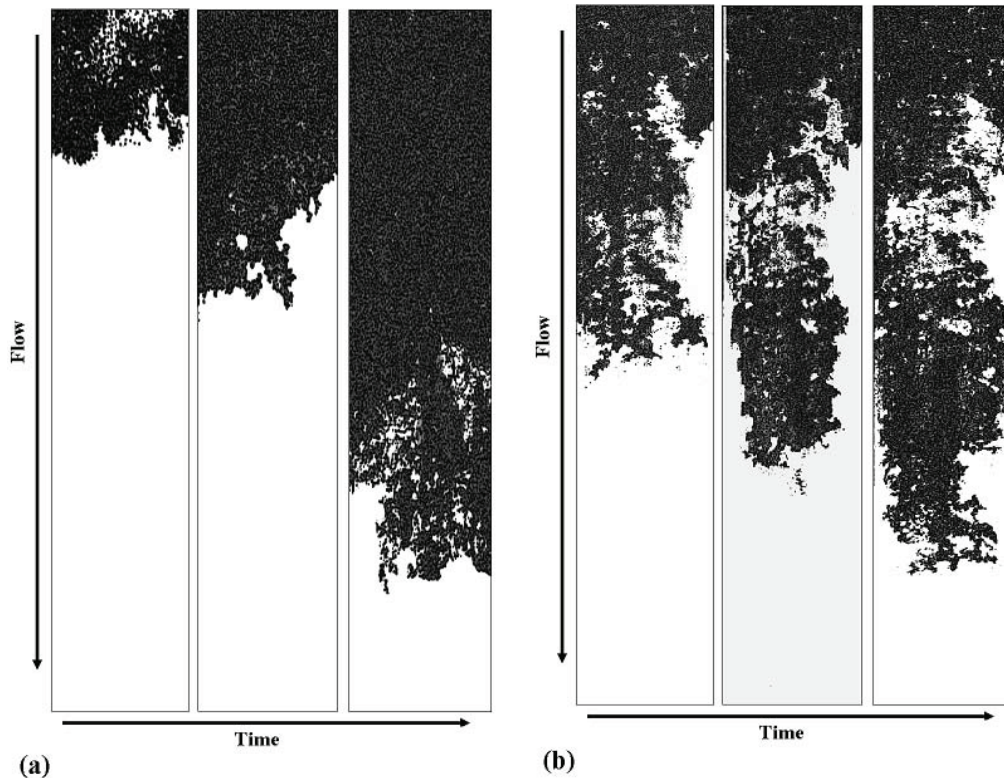


**FIG. 6:** Displacement structure of the invading wetting fluid observed in our experiments for configurations of **a)** slow displacement  $v_c/v = 0.9$  and **b)** viscous fingering under gravity  $v_c/v = 0.3$

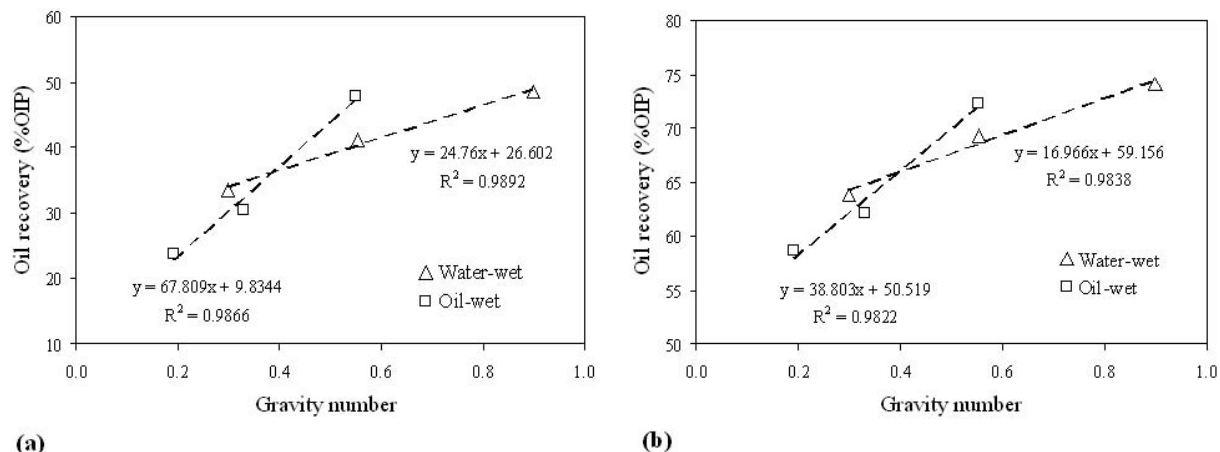


**FIG. 7:** Oil recoveries versus ratio of gravity to viscous forces (gravity number) **a)** at breakthrough time and **b)** at four pore volumes of injection

film flow occurring in a water-wet system due to higher capillary retention. This results in very low oil production in oil-wet pores at the later time. When the gravity number decreases, the plot of oil recovery against gravity number in an oil-wet system falls below the water-wet media. This sharp reduction in oil production indicates that the oil-wet porous media is much more sensitive to change in the ratio of gravity to viscous forces.

In addition, oil recovery has a linear trend with the ratio of gravity to viscous forces. In oil-wet systems, the slope of this linear trend is more than two times larger than the one obtained for the water-wet cases. This can be justified due to the blocking effect of irreducible water located at the center of the pores.

#### 4. CONCLUSIONS

Forced gravity drainage experiments during immiscible displacement of a wetting phase (synthetic oil) by a non-wetting phase (nitrogen) were performed on a synthetic porous media (bead pack), under a constant viscosity ratio and varying values of displacement rate. Structural analysis of the fluid distribution in porous media enabled the analysis of the invasion front stability by gradient percolation theory. The experimental results were also analyzed using dimensionless numbers. According to the experimental studies and the theoretical analysis presented in this paper, the following conclusions can be drawn.

- Critical gravity drainage rate for front instability shows a good agreement with investigations based

on percolation theory. The experimental results are consistent with stabilization criterion [Eq. (1)].

- Observed fluid displacement structures also confirmed that under stabilized gravity drainage criterion, slow front displacement would lead to the highest oil recovery.
- In stabilized gravity drainage experiments, the oil recovery at breakthrough time was higher for oil-wet systems. However, as the experiments continued, the oil production histories were consistent among different wettability states.
- As the viscous forces become more dominant (the capillary number increases), the recovery from oil-wet porous media decreases more compared to a water-wet system.
- Oil recovery has a linear relationship with the ratio of gravity to viscous forces. Results indicate that in an oil-wet system, the slope of oil production against gravity number is more than two times larger than the one obtained for the water-wet case.

#### ACKNOWLEDGMENT

The authors gratefully acknowledge Dr. M. Pooladi-Darvish for his unconditional availability for technical comments during this study. Acknowledgement is also extended to the laboratory assistance of PUT research center, H. Salimi, for his kind assistance during laboratory work. Authors' acknowledgement is also extended



to the Research and Technology Institute of NIOC for the financial support.

## REFERENCES

- Blackwell, J. T. and Terry, M. W., Factors influencing the efficiency of miscible displacement, *Trans AIME.*, vol. 216, pp. 1–8, 1959.
- Blunt, M., Zhou D., and Fenwick, D., Three-phase flow and gravity drainage in porous media, *J. Trans. Porous Media.*, vol. 20, pp. 77–103, 1995.
- Caubit, C., Bertin, H., and Hamon, G., Three-phase flow in porous media: wettability effect and residual saturations during gravity drainage and tertiary water flood, SPE Annual Technical Conference and Exhibition Houston, Paper No. SPE 90099, 2004.
- Dumore, J. M., Stability consideration in downward miscible displacement, *SPEJ*, vol. 4, pp. 356–362, 1964.
- Edwards, J. T., Honarpour, M. M., Hazlet, R. D., Cohen, M., Membere, A., Pebdani, F., Clayton, C., Al-Hussainy, R., Validation of gravity-dominated relative permeability and residual saturation in a giant oil reservoir, SPE Annual Technical Conference and Exhibition New Orleans, Paper No. SPE 49316, 1998.
- Fourar, M., S. Bories, R. Lenormand, and Persoff, P., Two-Phase flow in smooth and rough fractures: measurement and correlation by porous-medium and pipe flow models, *Water Resource. Res.*, vol. 29, pp. 3699–3708, 1993.
- Grattoni, C. A., Jing, X. D, and Dawe, R. A., Dimensionless groups for three-phase gravity drainage flow in porous media, *J. Petrol. Sci. Eng.*, vol. 29, pp. 53–65, 2001.
- Hagoort, J., Oil recovery by gravity drainage, *SPE J.*, vol. 20, no. 3, pp. 139–150, 1980.
- Hughes, R. G. and Blunt, M. J., Pore scale modeling of rate effects in imbibition, *J. Transp. Porous Media.*, vol. 40, pp. 295–322, 2000.
- Kewen, L. and Firoozabadi, A., Experimental study of wettability alteration to preferential gas-wetting in porous media and its effects, *SPE Reservoir Eval.*, vol. 3, no. 2, pp. 139–149, 2000.
- Lovoll G., Meheust Y., Maloy K. J., and Aker E., Competition of gravity, capillary and viscous forces during drainage in a two-dimensional porous medium, a pore scale study, *Energy J.*, vol. 30, no. 6, pp. 861–872, 2005.
- Meheust, Y., Lovoll, G., Maloy, K. J., and Schmittbuhl, J., Interface scaling in a 2d porous medium under combined viscous, gravity and capillary effects, *Phys. Rev. E*, vol. 66, pp. 51603–15, 2002.
- Morrow, N. R. and MacCaffrey, F. G., *Displacement Studies in Uniformly Wetted Porous Media, Wetting Spreading and Adhesion*, Academic Press, New York, pp. 289–319, 1978.
- Persoff, P. and Pruess, K., Two-phase flow visualization and relative permeability measurement in natural rough-walled rock fractures, *Water Resource. Res.*, vol. 31, pp. 1175–1995, 1995.
- Oren, P. E. and Pinczewski, W. V., Effect of wettability and spreading on recovery of water flood residual oil by immiscible gas flooding, *SPE Formation Eval.*, vol. 9, no 2, pp. 149–156, 1994.
- Pedraza, B., Betin, H., Hamon, G., and Augustine, A., Wettability effect on relative permeability during gravity drainage, Paper No. SPE 77542, Tulsa, OK, 2002.
- Shahidzadeh, N., Tournié, A., Bichon S., Vié, P., Rodts S., Faure P., Bertrand, F., and Azouni, A., Effect of wetting phase on gravity drainage in porous media, *J. Transp. Porous Media.*, vol. 56, pp. 209–224, 2004.
- Singh, M. and Mohanty, K. K., Dynamic modeling of drainage through three-dimensional porous materials, *Chem. Eng. Sci.*, vol. 58, pp. 1–18, 2003.
- Skauge, A., Haskjold, G., Thorsen, T, T., and Aarra, M., Accuracy of gas-oil relative permeability from two-phase flow experiments, International Symposium of the Society of Core Analysis, Calgary, Canada, Paper No. SCA 9707, 1997.
- Stauffer, D. and Aharony, A., *Introduction to Percolation Theory*, 2nd ed., Taylor & Francis, 1991.
- Theodoropoulou, M. A., Sygouni, V., Karoutsos, V., and Tsakiroglou, C. D., Relative permeability and capillary pressure functions of porous media as related to the displacement growth pattern, *Int. J. Multiphase Flow.*, vol. 31, pp. 1155–1180, 2008.
- Tsakiroglou, C. D., Theodoropoulou, M. A., Karoutsos, V., and Papanicolaou, D., Determination of the effective transport coefficients of pore networks from transient immiscible and miscible displacement experiments, *Water Resource Res. J.*, vol. 41, no. 2, W02014, 2005.
- Vizika, O. and Lombard, J. M., Wettability and spreading: Two key parameters in oil recovery with three-phase gravity drainage, *SPE Reservoir Eval.*, vol. 11, pp. 54–58, 1996.
- Wilkinson, D., Percolation effects in immiscible displacement, *Phys. Rev. A.*, vol. 34, pp. 1380–1391, 1986.
- Xu, B., Salin, D., and Yortsos, Y. C., Invasion percolation with viscous forces, *Phys. Rev. E.*, vol. 57, pp. 739–751, 1998.
- Zhou, D. and Blunt, M., Wettability effects in three-phase gravity drainage, *J. Pet. Sci. Eng.*, vol. 20, pp. 203–211, 1998.

# THEORY, METHOD, AND APPLICATION OF A NUMERICAL SIMULATION IN AN OIL RESOURCES BASIN METHODS OF NUMERICAL SOLUTIONS OF AERODYNAMIC PROBLEMS

Yi-Rang Yuan,<sup>1,\*</sup> Wen-Qia Wang,<sup>1</sup> & Yu-Ji Han<sup>2</sup>

<sup>1</sup>Institute of Mathematics, Shandong University, Jinan 250100, PRC

<sup>2</sup>Physical Exploration Institute of Shengli Petroleum Administration, Dongying 257022, PRC

\*Address all correspondence to Y. Yuan E-mail: yryuan@sdu.edu.cn

Original Manuscript Submitted: 2/24/2009; Final Draft Received: 5/11/2009

*This paper considers the theory, method, and application of a numerical simulation of an oil-gas basin. From geological science, geochemistry, permeation fluid mechanics, and computer technology, it puts forward the mechanical model, mathematical model, careful parallel upwind fractional steps implicit iterative finite difference scheme, parallel arithmetic program, parallel arithmetic information, and alternating direction mesh subdivision. Our work has realized a highly accurate numerical simulation in hundreds of meters with millions of nodes and during an extra long period of time. It has produced a first-at-home-and-abroad software system of resources evaluation and multilayer oil resources migration and accumulation. This system has successfully been applied in oil-gas resources evaluation in Jiyang Dongying Hollow, Huimin Hollow, Tanhai Region, and Yangxin Hollow, and has gotten good practical results. Thus, an important problem on oil resources is solved.*

**KEY WORDS:** *three-dimensional oil-gas basin, resources evaluation, migration-accumulation of permeation fluid mechanics, model and numerical simulation, actual application and analysis*

## 1. INTRODUCTION

The three-dimensional numerical simulation is intended to reproduce, with the application of geological science, geochemistry, permeation fluid mechanics, and computer technology, the dynamics of stratigraphic paleotemperature and pressure in a space-time concept, to further study oil-gas production, migration and accumulation, and distribution laws and ranges, and then to predict a basin, its deposit quantity, and location. All this is of great importance in both theory and practice for oil-gas resources evaluation, and for oil field exploration and development.

The simulation software of basin resources consists of five modules, namely, (i) a geochromic module, (ii) a heatchromic module, (iii) a module of hydrocarbons formation history, (iv) a module of hydrocarbons discharge history, and (v) a module of migration and accumulation history. The function of the first module is to rebuild the

history of basin sedimentation and structure. The function of the second module is to rebuild the history of paleoheat flow and paleotemperature. The third module rebuilds the history of hydrocarbons maturation and their growth in quantity. The fourth module rebuilds hydrocarbons discharge in an oil-gas basin, which is also called the history of first oil-gas migration (see Fig. 1). It prepares conditions for the last module. The fifth module rebuilds the migration and accumulation history of an oil-gas basin, or the secondary migration of oil and gas. It is the most challenging part in basin simulation, and it provides valuable information for the evaluation and location of a deposit.

Numerical simulation of the evolutionary history of a three-dimensional oil and gas bearing basin is to use modern computers and calculating techniques to repeat the process of a basin, which is an important basis for evaluating the quantity of oil and gas generation; moreover, researching the distribution and law of petroleum accumu-

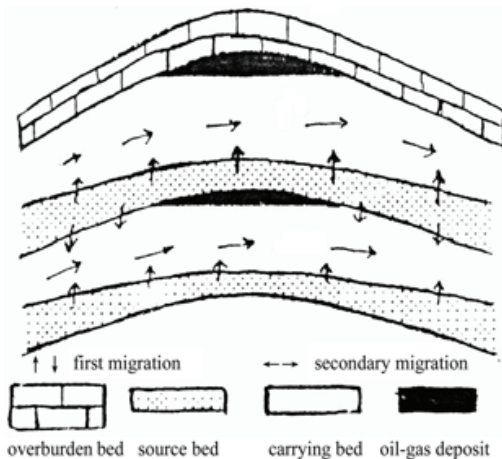


**FIG. 1:** Sketch map of first and secondary oil-gas migration

lation and migration (Li, 1989; Welte and Yukler, 1981; Yukler et al., 1978; Han et al., 1988).

Oil-gas migration is a process when an oil-gas mixture migrates from an oil-producing layer of a low number of holes and low permeability to the carrying layer of a high number of holes and high permeability. Finally, the oil-gas mixture collects in the accumulation layer. The first migration refers to the migration from the oil-producing layer to the layer of high holes and high permeability. Its greatest distance might be several kilometers. The secondary migration represents the migration from the carrying layer and along faults, cracks, passageways, and unconformity faces. When the structure is suitable, an oil-gas deposit is formed, and its greatest migration distance might be as great as tens of kilometers (Ewing, 1983; Ungerer et al., 1987; Ungerer, 1990; Walte, 1987; Allen et al., 1995; Wang and Guan, 1999).

The function of our numerical simulation is to rebuild the migration-accumulation history of oil-gas basins. It is the most difficult part in basin simulation and plays a very valuable role in locating oil deposits and finding new oil fields. Therefore, it is a very challenging problem in petroleum geology, even for the major industrial countries in the world.

From 1989 to 1997, the Institute of Mathematics of Shandong University and the Physical Exploration Institute of Shengli Petroleum Administration jointly undertook the key research projects: "Study on three-dimensional basin simulation system" and "Study on the second quantitative simulation for migration-accumulation" (Inst. Math, Shandong Univ., 1993, 1997).

From 1998 to 2004, the Institute of Mathematics of Shandong University and the Physical Exploration Institute of Shengli Petroleum Administration jointly undertook the key research projects: "Quantitative numerical simulation of multi-layer oil resources migration-accumulation" and "Careful parallel regional numerical simulation of secondary oil migration-accumulation." We studied the quantitative numerical simulation techniques of multilayer (with faults and passageways) oil-gas migration and accumulation. As a result, we proposed a new numerical model. This model creatively built a new careful parallel operator splitting up implicit iterative scheme, parallel computation process, information transmission of parallel computation, and alternating-direction one-dimensional strip decomposition computation, thus successfully realizing the highly accurate numerical simulation in hundreds of meters with millions of nodes and during as long as  $3.0 \times 10^7$  years. Our theoretical analysis has solved a difficult problem in petroleum geology, permeability dynamics, and computation technology (Allen et al., 1995; Wang and Guan, 1999; Zhang, 1995; Cha, 1997; Zeng and Jin, 2000; Shi, 1994). Thus, we are the first in China to have developed a software system of multilayer oil migration and accumulation. This system has been used in the oil-gas evaluation in Huimin Hollow, Dongying Hollow, and the Tanhai Region of Shengli Oilfield, and has gotten desirable simulation results (Inst. Math, Shandong Univ., 2001, 2004).

From 2004 to 2005, the Institute of Mathematics of Shandong University and Exploration Institute of Shengli Petroleum Administration jointly undertook the key research project: "Numerical simulation of oil migration-accumulation passageway" (Inst Math., Shandong Univ., 2005). This system has been used in the oil resources evaluation in Yangxin Hollow.

Ungerer et al. (1987) and Ungerer (1990) developed a two-dimensional model. BMW system of Beijing Exploration Research Institute studied one-dimensional hydrocarbons formation and two-dimensional migration Shi (1994). The Research Center of Marine Petroleum Company has introduced a specialist system into basin simulation and trap evaluation. In references available, we have not found reports on the numerical simulation of multilayer oil migration and accumulation (Ewing, 2000).

## 2. NUMERICAL SIMULATION AND ANALYSIS OF RESOURCES EVALUATION

With the development and application of the geological science, geochemistry, computer, and calculating tech-

nique, methods of resources evaluation have been advancing from qualitative analysis to quantification. Numerical simulation for the evolutionary history of a three-dimensional oil and gas bearing basin is to use modern computers and calculating techniques to repeat the process of basin evolution, especially for dynamic processes of paleotemperature and abnormal pressure of sedimentary basin, which is an important basis for evaluating the quantity of oil and gas generation, and moreover, researching the distribution and law of petroleum accumulation and migration. The mathematical model of basin simulation is an initial boundary value problem of a system of coupled nonlinear partial differential equations. Usually, a basin has an evolutionary history of several millions, even hundreds of millions, of years and a very large area and thickness. Furthermore, its boundary has varied with the sedimentary process. This has resulted in difficulties for numerical simulation. The model repeats the geological evolution of the basin, densification of sediments, the geosphere temperature, and the history of geosphere pressure changes. It computes the quantity of hydrocarbons of kerogen heat decomposition. Thus, it can give a quite scientific evaluation of the oil resources potential of the basin.

The mathematical model of the basin evolution is an initial boundary value problem of a system of parabolic partial differential equations, in which the first one on abnormal pressure  $p$  and the second one on paleotemperature  $T$  are parabolic, and the third one on porosity  $\phi$  is a first-order ordinary differential equation (Welte and Yukler, 1981; Yukler et al., 1978; Han et al., 1988; Ewing, 1983).

$$\nabla \cdot \left( \frac{K}{\mu} \nabla p \right) = \varphi \frac{\partial p}{\partial t} - f \frac{\partial S}{\partial t} + \varphi \frac{\partial P_n}{\partial t}$$

$$X = (x, y, z)^T \in \Omega_1, t \in J = (0, \bar{T}] \quad (1a)$$

$$p \equiv 0, \quad X \in \Omega_2$$

$$t \in J \text{ (abnormal pressure equation)} \quad (1b)$$

$$\nabla \cdot (K_s \nabla T) - c_w \rho_w \nabla \cdot (VT) + Q = c_s \rho_s \frac{\partial T}{\partial t}$$

$$X \in \Omega, \quad t \in J \text{ (heat flow equation)} \quad (2)$$

$$\frac{\partial \phi}{\partial t} = -f \left( \frac{\partial S}{\partial t} - \frac{\partial p}{\partial t} - \frac{\partial P_n}{\partial t} \right), \quad X \in \Omega$$

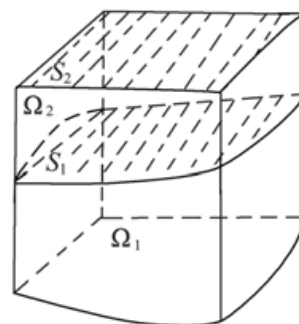
$$t \in J \text{ (porosity equation)} \quad (3)$$

Figure 2a illustrates the definite domain  $\Omega, \Omega = \Omega_1 \cup \Omega_2$ , where  $\Omega_1$  is an abnormal pressure region and  $\Omega_2$  is a normal pressure region.  $\bar{T}$  is the total simulation time. Equation (1a) holds in  $\Omega_1$  and  $p \equiv 0$  in  $\Omega_2$ . The paleotemperature  $T$  is defined in  $\Omega$ , where  $\nabla = (\partial/\partial x, \partial/\partial y, \partial/\partial z)^T$ , and  $\phi = \phi(X, t)$  is the porosity.  $S$  denotes the overburden on the rock load.  $P_n$  denotes the rest water depth pressure, where  $P_n = \rho_w g D$ , and  $D$  is the water depth.  $\varphi = \alpha(1 - \phi) + \beta\phi$ ,  $f = \alpha(1 - \phi)$ , and  $\alpha$  and  $\beta$  are the compressibility of rock and flow in porous media;  $\mu$  is the fluid viscosity,  $K$  is permeability,  $V = -K/\mu \nabla(p - \rho_w g D)$  is the Darcy velocity, and  $K_s, \rho_s$ , and  $c_s$  are the thermal conductivity, density, and specific heat of the sediment, respectively.  $c_w$  and  $\rho_w$  are the specific heat and density of flow, and  $Q$  is the thermal sink or source term; it is a known function.

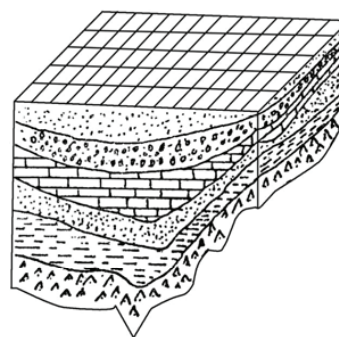
The boundary conditions are

$$p = 0, (X, t) \in S_1 \times J, \nabla p \cdot \vec{\gamma} = 0, (X, t) \in (\partial\Omega_1 \setminus S_1) \times J$$

$$T = T_0, (X, t) \in S_2 \times J, \nabla T \cdot \vec{\gamma} = 0, (X, t) \in (\partial\Omega \setminus S_2) \times J$$



(a)



(b)

**FIG. 2:** a) Sketch map of definite domain; b) A sketch of the simulating basin

where  $\vec{\gamma}$  is the outer normal to  $\partial\Omega_1$  and  $\partial\Omega$ ,  $\nabla p \cdot \vec{\gamma}$  denotes an impermeable boundary condition, and  $\nabla T \cdot \vec{\gamma}$  denotes an adiabatic boundary condition.

The initial conditions are

$$p(X, 0) = p^0(X), \quad T(X, 0) = T^0(X), \quad X \in \Omega$$

We used a mesh region  $\Omega_h$  to replace  $\Omega$ , and let  $X_{ijk} = (x_i, y_j, z_k)^T = (ih_x, jh_y, kh_z)^T$ ,  $X_{ijk} \in \Omega_h$ ,  $t^n = n\Delta t$ , and  $W_{ijk}^n = W(X_{ijk}, t^n)$ . Replacing  $\partial p / \partial t$  with  $(p^{n+1} - p^n) / \Delta t$  in Eq. (1a), we obtain

$$\nabla \cdot (K_\mu \nabla p^{n+1}) = \varphi \frac{p^{n+1} - p^n}{\Delta t} - f \frac{\partial S}{\partial t} + \varphi \frac{\partial P_n}{\partial t} \quad (4)$$

We rewrite Eq. (4) in a splitting form as follows:

$$\begin{aligned} & \left[ 1 - \Delta t \varphi^{-1} \frac{\partial}{\partial z} \left( K_\mu \frac{\partial}{\partial z} \right) \right] \left[ 1 - \Delta t \varphi^{-1} \frac{\partial}{\partial x} \left( K_\mu \frac{\partial}{\partial x} \right) \right] \\ & \times \left[ 1 - \Delta t \varphi^{-1} \frac{\partial}{\partial y} \left( K_\mu \frac{\partial}{\partial y} \right) \right] p^{n+1} = p^n \\ & + \Delta t \varphi^{-1} f \frac{\partial S}{\partial t} - \Delta t \frac{\partial P_n}{\partial t} \end{aligned} \quad (5)$$

where

$$K_{\mu,ijk} = \left( \frac{K}{\mu} \right)_{ijk}$$

Let  $K_{\mu,i+1/2,jk} = 2K_{\mu,i+1,jk}K_{\mu,ijk}h_yh_z\Delta t / [(K_{\mu,i+1,jk} + K_{\mu,ijk})h_x]$ ,  $E_{ijk} = \varphi_{ijk}h_xh_yh_z$ , and  $F_{ijk} = f_{ijk}h_xh_yh_z$ . Let  $P_k$  and  $T_k$  be the difference solutions,  $\delta_x(K_\mu \delta_{\bar{x}} P_h^n)_{ijk} = K_{\mu,i+1/2,jk}(P_{h,i+1,jk}^n - P_{h,ijk}^n) - K_{\mu,i-1/2,jk}(P_{h,ijk}^n - P_{h,i-1,jk}^n)$ , and  $\delta_y(K_\mu \delta_{\bar{y}} P_h^n)_{ijk}$ ,  $\delta_z(K_\mu \delta_{\bar{z}} P_h^n)_{ijk}$  be similar. From the known  $P_h^n$  we can obtain the solution  $P_h^{n+1}$  as follows:

$$\begin{aligned} \delta_z(K_\mu \delta_{\bar{z}} P_h^{n+1/3})_{ijk} &= E_{ijk} (P_{h,ijk}^{n+1/3} - P_{h,ijk}^n) \\ &- F_{ijk} (S_{ijk}^{n+1} - S_{ijk}^n) + E_{ijk} (P_{n,ijk}^{n+1} - P_{n,ijk}^n) \end{aligned} \quad (6a)$$

$$\delta_x(K_\mu \delta_{\bar{x}} P_h^{n+2/3})_{ijk} = E_{ijk} (P_{h,ijk}^{n+2/3} - P_{h,ijk}^{n+1/3}) \quad (6b)$$

$$\delta_y(K_\mu \delta_{\bar{y}} P_h^{n+1})_{ijk} = E_{ijk} (P_{h,ijk}^{n+1} - P_{h,ijk}^{n+2/3}) \quad (6c)$$

Let  $\delta_x(V_x T_h^n)_{ijk} = V_{x,i+1/2,jk} [(T_{h,i+1,jk}^n + T_{h,ijk}^n) / 2] - V_{x,i-1/2,jk} [(T_{h,i-1,jk}^n + T_{h,ijk}^n) / 2]$ ,  $(R_{xy})_{ijk} = (c_w \rho_w)_{ijk} h_x h_y$ ,  $(R_s)_{ijk} = (c_s \rho_s)_{ijk} h_x h_y h_z$ ,  $\delta_y(V_y T_h^n)_{ijk}$ ,  $\delta_z(V_z T_h^n)_{ijk}$ ,  $(R_{xz})_{ijk}$ ,  $(R_{yz})_{ijk}$  be similar.

Similarly to the discretizing process of the abnormal pressure equation, we can define the finite difference scheme of heat flow equation by

$$\begin{aligned} \delta_z(K_s \delta_{\bar{z}} T_h^{n+1/3})_{ijk} - (R_{xy})_{ijk} \delta_z(V_z T_h^{n+1/3})_{ijk} \\ + Q h_x h_y \Delta t = (R_s)_{ijk} (T_{h,ijk}^{n+1/3} - T_{h,ijk}^n) \end{aligned} \quad (7a)$$

$$\begin{aligned} \delta_x(K_s \delta_{\bar{x}} T_h^{n+2/3})_{ijk} - (R_{yz})_{ijk} \delta_x(V_x T_h^{n+2/3})_{ijk} \\ = (R_s)_{ijk} (T_{h,ijk}^{n+2/3} - T_{h,ijk}^{n+1/3}), \end{aligned} \quad (7b)$$

$$\begin{aligned} \delta_y(K_s \delta_{\bar{y}} T_h^{n+1})_{ijk} - (R_{xz})_{ijk} \delta_y(V_y T_h^{n+1})_{ijk} \\ = (R_s)_{ijk} (T_{h,ijk}^{n+1} - T_{h,ijk}^{n+2/3}) \end{aligned} \quad (7c)$$

where  $V = (V_x, V_y, V_z)$  is Darcy's velocity.

For Eq. (7a), we must add the heat sink or source terms  $Q h_x h_y \Delta t$  to the right sides of equations defined at nodes lying on the bottom of the basin. According to Arrhenius Law (Welte and Yukler, 1981; Yukler et al., 1978; Han et al., 1988), temperature and time are the main factors of the heat decomposition of kerogen into oil, in linear relation with time and in index number relation with temperature. The quantity of the produced hydrocarbons by kerogen heat decomposition can be computed, and a scientific evaluation of the basin oil resources potential can be made.

For the porosity Eq. (3), the governing equation of rock mechanics, we can directly find out the approximate solution by use of direct integration after the abnormal pressure  $P^{n+1}$  at  $t^{n+1}$  has been obtained.

## 2.1 Numerical Actual Example

By using the numerical method described, we calculate a practical problem provided by Shengli Petroleum Administration (Table 1). Figure 2b illustrates the basin simulated. There are  $15 \times 6$  nodes on the plane. Fifteen stratums, different from each other, are numbered from bottom to top of the basin. We take a very large time step size of 5 million years to calculate. The space step sizes along the  $x$  and  $y$  directions and along the  $z$  direction are 1.5 km and 20 m, respectively. The numerical result shows that the approximate abnormal pressure and paleotemperature display physical characteristics quite in accordance with the practical problem, and the thickness of the stratum obtained by simulation fits with the practical geological data as well.

Take geological time at which the basin begins to deposit as zero time. Figures 3a and 3c illustrate the

**TABLE 1:** Geological parameter table

Name and signs	Numerical value and formula
Viscosity $\mu$	$(5.3 + 3.8AT - 0.26AT^3)^{-t}$ , $AT = (T - 150)/100$
Density (flow) $\rho_w$	$\rho_{w0} [1 + \beta_T(T - T_0)]$ , $\beta_T = -0.5 \times e^{-3}$
Density (sediment) $\rho_S$	$\phi\rho_w + (1 - \phi)\rho_S$
Time step $\Delta t$	$50 \times 10^4$ years
Step ( $x, y$ directions) $h_x, h_y$	$1.5 \times 10^3$ cm
Step ( $z$ direction) $h_z$	$2.0 \times 10^3$ cm

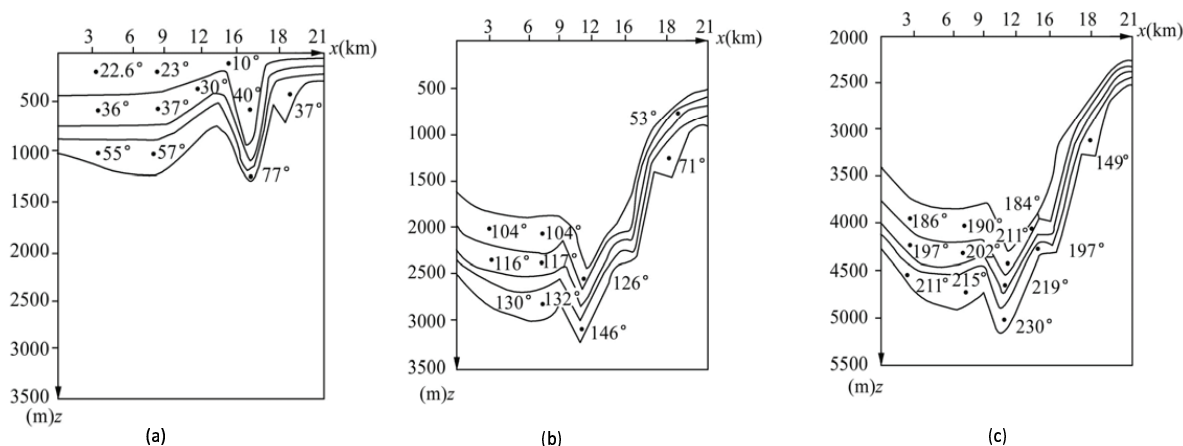


**FIG. 3:** **a)** Distribution of temperature on layers from 1 to 4 after basin deposited for 40 million years; **b)** distribution of temperature on layers from 1 to 4 after basin deposited for 110 million years; **c)** Distribution of temperature on layers from 1 to 4 after basin deposited for 410 million years

distribution of paleotemperature on the section plane  $j = 2$  of layers from 1 to 4 at different geological times, which agree with the physical characteristics of practical problems very well. We obtain a numerical variable process of many important geological parameters such as porosity  $\phi$ , permeability  $\kappa$ , and fluid viscosity  $\mu$ .

### 2.2 Actual Application

Applying this kind of numerical method, we have developed the software “simulation system of three-dimensional oil resources basin.” It has been used successfully in many numerical simulation projects of the depressions and peripheral locality in Jiyang Depression, Shengli Oilfield, which offers a basis for exploration policy and brings many actual advantages. As more geological reserves can be founded, the success rate of exploration is increased and as few exploratory wells as possible are used.

Figures 4a and 4b illustrate the Jiyang Depression Sand Third Lower source intensity isogram figure and Sand Third Lower gas intensity isogram figure.

### 3. THE THREE-DIMENSIONAL NUMERICAL SIMULATION OF SINGLE-LAYER MIGRATION ACCUMULATION

The numerical simulation of the evolutionary history of the basin is conducted according to the mechanism of petroleum geology and mechanics of the fluid in porous media to simulate the process of basin evolution, hydrocarbon generation, migration, and accumulation of oil by using modern computers. This thesis discusses the numerical simulation of the secondary migration and accumulation, the most difficult part in basin simulation and important in rational evaluation of oil resources exploration and oil deposit location.

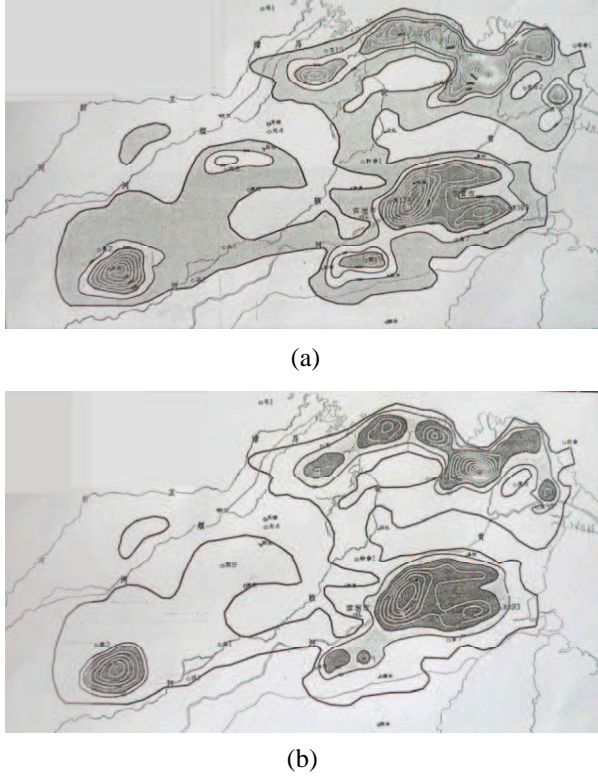


**FIG. 4:** **a)** Jiyang Depression Sand Third Lower source intensity isogram; **b)** Jiyang Depression Sand Third Lower gas intensity isogram

The fluid dynamics model of secondary migration and accumulation has strong hyperbolic characteristics. Therefore, the numerical method is very difficult in mathematics and mechanics (Ungerer et al., 1987; Ungerer, 1990; Walte, 1987; Allen et al., 1995; Wang and Guan, 1999; Zhang, 1995; Cha, 1997; Zeng and Jin, 2000; Shi, 1994).

Up to the present, there have been only a few preliminary numerical results for the two-dimensional cut plan problems, but the three-dimensional problems have not been touched yet (Ungerer, 1990; Walte, 1987; Allen et al., 1995; Shi, 1994). This thesis, from the actual conditions and the consideration of the above characteristics, puts forward a kind of modified method of second-order splitting-up implicit iterative scheme. For the famous hydraulic experiment (Hubbert, 1953; Dembicki, 1989; Catalan, 1992) with the secondary migration and accumulation conducted by Hubbert, Dembicki, and Calalan, we have done the numerical simulation test and gotten the identical computational and experimental results. For

the actual problem of Dongying Hollow (single layer) and Huimin Hollow (multilayer) in Shengli Petroleum Oil Field, our numerical simulation test is basically coincident with the actual conditions. Thus the well-known problem has been thoroughly solved.

The migration of oil and water in the stratum is mainly a process of immiscible flow. Oil and water potential controls the direction of the immiscible flow and magnitude of the flow force.

The mechanics model of the problem is the following nonlinear partial differential equations with the initial-boundary problem:

$$\nabla \cdot \left( K \frac{k_{ro}}{\mu_o} \nabla \psi_o \right) + B_o q = -\Phi s' \left( \frac{\partial \psi_o}{\partial t} - \frac{\partial \psi_w}{\partial t} \right)$$

$$X = (x, y, z)^T \in \Omega, t \in J = (0, T] \quad (8)$$

$$\nabla \cdot \left( K \frac{k_{rw}}{\mu_w} \nabla \psi_w \right) + B_w q = \Phi s' \left( \frac{\partial \psi_o}{\partial t} - \frac{\partial \psi_w}{\partial t} \right)$$

$$X \in \Omega, t \in J \quad (9)$$

where  $\psi_o$  and  $\psi_w$  are the potential functions,  $k_{ro}$  and  $k_{rw}$  are the relative permeabilities for the oil and water phases, respectively.  $K$  is the absolute permeability,  $\Phi$  is the porosity, and  $s' = ds/dp_c$ , where  $s$  is the concentrations for the water phase.  $p_c(s)$  is the capillary pressure function,  $B_o = (k_{ro}/\mu_o)(k_{ro}/\mu_o + k_{rw}/\mu_w)^{-1}$ ,  $B_w = (k_{rw}/\mu_w)(k_{ro}/\mu_o + k_{rw}/\mu_w)^{-1}$  are flow coefficients, and  $q$  is the source (sink) function.

Let  $\Delta x$ ,  $\Delta y$ ,  $\Delta z$ , and  $\Delta t$  be steps of the  $x$ ,  $y$ ,  $z$ ,  $t$  directions, respectively. Let  $M_{ijk} = (i\Delta x, j\Delta y, k\Delta z)^T$ , and  $t^m = m\Delta t$ . Assume that the approximate solution  $\{\psi_w^m, \psi_o^m, s^m\}$  at time  $t^m$  is known. We should find out  $\{\psi_w^{m+1}, \psi_o^{m+1}, s^{m+1}\}$  at time  $t^{m+1}$ . Let

$$\Delta(A\Delta\psi) = \Delta_{\bar{x}}(A_x\Delta_x\psi) + \Delta_{\bar{y}}(A_y\Delta_y\psi) + \Delta_{\bar{z}}(A_z\Delta_z\psi) \quad (10)$$

where  $\Delta_{\bar{x}}(A_x\Delta_x\psi^{m+1}) = A_{x,i+1/2,jk}(\psi_{i+1,jk} - \psi_{ijk})^{m+1} - A_{x,i-1/2,jk}(\psi_{ijk} - \psi_{i-1,jk})^{m+1}$ , and  $A_{x,i+1/2,jk} = \{K(\Delta y\Delta z/\Delta x)(k_{rw}/\mu_w)\}_{i+1/2,jk}$ . Take the value of  $k_r$ , according to the partial upper reaches principle, and other terms can be defined similarly.

Suppose we can find out  $\{\psi_w^{m+1}, \psi_o^{m+1}\}$  at  $t^{m+1}$ , then the concentration of water can be attained by using the following formula:

$$s^{m+1} = s^m + s'(\psi_o^{m+1} - \psi_o^m - \psi_w^{m+1} + \psi_w^m) \quad (11)$$

### 3.1 The Modified Method of Second-Order Splitting-Up Implicit Iterative Scheme of the Three-Dimensional Problem

In the  $z$  direction,

$$\begin{aligned} & \frac{1}{2}\Delta_{\bar{z}}(A_{zw}\Delta_z\psi_w^*) + \frac{1}{2}\Delta_{\bar{z}}(A_{zw}\Delta_z\psi_w^{(l)}) \\ & + \Delta_{\bar{y}}(A_{yw}\Delta_y\psi_w^{(l)}) + \Delta_{\bar{x}}(A_{xw}\Delta_x\psi_w^{(l)}) - G\psi_w^* \\ & + G\psi_w^* = H_{l+1} \left( \sum A_w \right) (\psi_w^* - \psi_w^{(l)}) - B_w^m q^{m+1} \\ & - G\psi_w^m + G\psi_w^m \end{aligned} \quad (12a)$$

$$\begin{aligned} & \frac{1}{2}\Delta_{\bar{z}}(A_{zo}\Delta_z\psi_o^*) + \frac{1}{2}\Delta_{\bar{z}}(A_{zo}\Delta_z\psi_o^{(l)}) \\ & + \Delta_{\bar{y}}(A_{yo}\Delta_y\psi_o^{(l)}) + \Delta_{\bar{x}}(A_{xo}\Delta_x\psi_o^{(l)}) + G\psi_o^* \\ & - G\psi_o^* = H_{l+1} \left( \sum A_o \right) (\psi_o^* - \psi_o^{(l)}) - B_o^m q^{m+1} \\ & + G\psi_o^m - G\psi_o^m \end{aligned} \quad (12b)$$

In the  $y$  direction,

$$\begin{aligned} & \frac{1}{2}\Delta_{\bar{y}}(A_{yw}\Delta_y\psi_w^{**}) - \frac{1}{2}\Delta_{\bar{y}}(A_{yw}\Delta_y\psi_w^{(l)}) - G\psi_w^{**} \\ & + G\psi_w^{**} = H_{l+1} \left( \sum A_w \right) (\psi_w^{**} - \psi_w^*) \\ & - G\psi_w^* + G\psi_w^* \end{aligned} \quad (12c)$$

$$\begin{aligned} & \frac{1}{2}\Delta_{\bar{y}}(A_{yo}\Delta_y\psi_o^{**}) - \frac{1}{2}\Delta_{\bar{y}}(A_{yo}\Delta_y\psi_o^{(l)}) + G\psi_o^{**} \\ & - G\psi_o^{**} = H_{l+1} \left( \sum A_o \right) (\psi_o^{**} - \psi_o^*) \\ & + G\psi_o^* - G\psi_o^* \end{aligned} \quad (12d)$$

In the  $x$  direction,

$$\begin{aligned} & \frac{1}{2}\Delta_{\bar{x}}(A_{xw}\Delta_x\psi_w^{(l+1)}) - \frac{1}{2}\Delta_{\bar{x}}(A_{xw}\Delta_x\psi_w^{(l)}) - G\psi_w^{(l+1)} \\ & + G\psi_w^{(l+1)} = H_{l+1} \left( \sum A_w \right) (\psi_w^{(l+1)} - \psi_w^{**}) \\ & - G\psi_w^{**} + G\psi_w^{**} \end{aligned} \quad (12e)$$

$$\begin{aligned} & \frac{1}{2}\Delta_{\bar{x}}(A_{xo}\Delta_x\psi_o^{(l+1)}) - \frac{1}{2}\Delta_{\bar{x}}(A_{xo}\Delta_x\psi_o^{(l)}) + G\psi_o^{(l+1)} \\ & - G\psi_o^{(l+1)} = H_{l+1} \left( \sum A_o \right) (\psi_o^{(l+1)} - \psi_o^{**}) \\ & + G\psi_o^{**} - G\psi_o^{**} \end{aligned} \quad (12f)$$

where  $G = -\Delta x \Delta y \Delta z \Phi \cdot s' / \Delta t$ ,  $H_{l+1}$  is the iterative factor,  $\sum A_w = A_{w,i+1/2,jk} + A_{w,i-1/2,jk} + \dots +$

$A_{w,ij,k-1/2}$ , and  $\sum A_o = A_{o,i+1/2,jk} + A_{o,i-1/2,jk} + \dots + A_{o,ij,k-1/2}$ . In practical computation, we take  $B_w^m = B_w(s^m)$ ,  $B_o^m = B_o(s^m)$ ,  $G = G(s^m)$ ,  $A_w = A_w(s^m)$ , and  $A_o = A_o(s^m)$ . They are all known.

For high accuracy purposes, we introduce the residual computational value,

$$P_z = \psi_w^* - \psi_w^{(l)}, P_y = \psi_w^{**} - \psi_w^*, P_x = \psi_w^{(l+1)} - \psi_w^{**} \quad (13a)$$

$$R_z = \psi_o^* - \psi_o^{(l)}, R_y = \psi_w^{**} - \psi_w^*, R_x = \psi_o^{(l+1)} - \psi_o^{**} \quad (13b)$$

Finally, we put forward the modified method of the second-order splitting-up implicit iterative scheme as follows.

In the  $z$  direction,

$$\begin{aligned} & \frac{1}{2}\Delta_{\bar{z}}(A_{zw}\Delta_z P_z) - \left( G + H_{l+1} \sum A_w \right) P_z + GR_z \\ & = - \left[ \Delta(A_w \Delta \psi_w^{(l)}) + B_w^m q^{m+1} - G(\psi_w^{(l)} - \psi_w^m) \right. \\ & \left. + G(\psi_o^{(l)} - \psi_o^m) \right] \end{aligned} \quad (14a)$$

$$\begin{aligned} & \frac{1}{2}\Delta_{\bar{z}}(A_{zo}\Delta_z R_z) - \left( G + H_{l+1} \sum A_o \right) R_z + GP_z \\ & = - \left[ \Delta(A_o \Delta \psi_o^{(l)}) + B_o^m q^{m+1} + G(\psi_w^{(l)} - \psi_w^m) \right. \\ & \left. - G(\psi_o^{(l)} - \psi_o^m) \right] \end{aligned} \quad (14b)$$

In the  $y$  direction,

$$\begin{aligned} & \frac{1}{2}\Delta_{\bar{y}}(A_{yw}\Delta_y P_y) - \left( G + H_{l+1} \sum A_w \right) P_y + GR_y \\ & = - \frac{1}{2}\Delta_{\bar{y}}(A_{yw}\Delta_y P_z) \end{aligned} \quad (14c)$$

$$\begin{aligned} & \frac{1}{2}\Delta_{\bar{y}}(A_{yo}\Delta_y R_y) - \left( G + H_{l+1} \sum A_o \right) R_y + GP_y \\ & = - \frac{1}{2}\Delta_{\bar{y}}(A_{yo}\Delta_y R_z) \end{aligned} \quad (14d)$$

In the  $x$  direction,

$$\begin{aligned} & \frac{1}{2}\Delta_{\bar{x}}(A_{xw}\Delta_x P_x) - \left( G + H_{l+1} \sum A_w \right) P_x + GR_x \\ & = - \frac{1}{2}\Delta_{\bar{x}}[A_{xw}\Delta_x(P_y + P_z)] \end{aligned} \quad (14e)$$

$$\begin{aligned} & \frac{1}{2}\Delta_{\bar{x}}(A_{xo}\Delta_x P_x) - \left( G + H_{l+1} \sum A_o \right) R_x + GP_x \\ & = - \frac{1}{2}\Delta_{\bar{x}}[A_{xo}\Delta_x(R_y + R_z)] \end{aligned} \quad (14f)$$



When the iterative error reaches our accuracy index, the iterative values  $\psi_o^{(l+1)}$ ,  $\psi_w^{(l+1)}$  are regarded as  $\psi_o^{m+1}$ ,  $\psi_w^{m+1}$ . Again, by Eq. (11), we find out  $s^{m+1}$ .

If the actual thickness of the carrying bed is much smaller than the size of the horizontal simulation area, we propose the solution by reducing it to a two-dimensional problem in the following way so it can also be called a quasi-three-dimensional problem. Owing to a relatively small  $\Delta z$ , we suppose that  $k_{ro}/\mu_o$ ,  $k_{rw}/\mu_w$ ,  $B_o$ , and  $B_w$  change very little in the  $z$  direction. By integrating  $z$  with Eqs. (8) and (9), the average results are approximately

$$\nabla \cdot \left( \bar{K} \frac{\Delta z k_{ro}}{\mu_o} \nabla \psi_o \right) + B_o \bar{q} \Delta z = -\bar{\Phi} s' \Delta z \left( \frac{\partial \psi_o}{\partial t} - \frac{\partial \psi_w}{\partial t} \right) \quad (15)$$

$$\nabla \cdot \left( \bar{K} \Delta z \frac{k_{rw}}{\mu_w} \nabla \psi_w \right) + B_w \bar{q} \Delta z = \bar{\Phi} s' \Delta z \left( \frac{\partial \psi_o}{\partial t} - \frac{\partial \psi_w}{\partial t} \right) \quad (16)$$

where  $\Delta z$  is the thickness of the carrying bed.

$$\bar{K} = \frac{1}{\Delta z} \int_{h_1(x,y)}^{h_2(x,y)} K(x,y,z) dz$$

$$\bar{\Phi} = \frac{1}{\Delta z} \int_{h_1(x,y)}^{h_2(x,y)} \Phi(x,y,z) dz$$

$$\bar{q} = \frac{1}{\Delta z} \int_{h_1(x,y)}^{h_2(x,y)} q(x,y,z) dz$$

where  $h_1(x,y)$  and  $h_2(x,y)$  are the depths of the carrying bed for the upper boundary and lower boundary, respectively.

Since the actual thickness of the carrying bed is much smaller than the size of horizontal simulation area, we can transform the three-dimensional problems (8) and (9) by reducing them to the two-dimensional problems, so it is called a quasi-three-dimensional problem. For a quasi-three-dimensional problem, we similarly put forward a kind of modified method of second-order splitting-up implicit iterative scheme.

In the  $x$  direction,

$$\begin{aligned} & \Delta_{\bar{x}}(A_{xw} \Delta_x \psi_w^*) + \Delta_{\bar{y}}(A_{yw} \Delta_y \psi_w^{(l)}) - G \psi_w^* + G \psi_o^* \\ & = H_{l+1} \left( \sum A_w \right) (\psi_w^* - \psi_w^{(l)}) - B_w^m q^{m+1} \\ & - G \psi_w^m + G \psi_o^m \end{aligned} \quad (17a)$$

$$\begin{aligned} & \Delta_{\bar{x}}(A_{xo} \Delta_x \psi_o^*) + \Delta_{\bar{y}}(A_{yo} \Delta_y \psi_o^{(l)}) + G \psi_w^* - G \psi_o^* \\ & = H_{l+1} \left( \sum A_o \right) (\psi_o^* - \psi_o^{(l)}) - B_o^m q^{m+1} \\ & + G \psi_w^m - G \psi_o^m \end{aligned} \quad (17b)$$

In the  $y$  direction,

$$\begin{aligned} & \Delta_{\bar{x}}(A_{xw} \Delta_x \psi_w^*) + \Delta_{\bar{y}}(A_{yw} \Delta_y \psi_w^{(l+1)}) - G \psi_w^{(l+1)} \\ & + G \psi_o^{(l+1)} = H_{l+1} \left( \sum A_w \right) (\psi_w^{(l+1)} - \psi_w^*) \\ & - B_w^m q^{m+1} - G \psi_w^m + G \psi_o^m \end{aligned} \quad (18a)$$

$$\begin{aligned} & \Delta_{\bar{x}}(A_{xo} \Delta_x \psi_o^*) + \Delta_{\bar{y}}(A_{yo} \Delta_y \psi_o^{(l+1)}) + G \psi_w^{(l+1)} \\ & - G \psi_o^{(l+1)} = H_{l+1} \left( \sum A_o \right) (\psi_o^{(l+1)} - \psi_o^*) \\ & - B_o^m q^{m+1} + G \psi_w^m - G \psi_o^m \end{aligned} \quad (18b)$$

where  $G = -V_p \Phi s' / \Delta t$ ,  $V_p = \Delta x \Delta y$ ,  $H_{l+1}$  is the iterative factor, and  $\sum A_w = A_{w,i+1/2,j} + A_{w,i-1/2,j} + \dots + A_{w,i,j-1/2}$ ,  $\sum A_o = \dots$ . The amount of practical calculation can be reduced. Similar to the three-dimensional problem, when the approximate solution  $\{\psi_w^m, \psi_o^m, s^m\}$  at time  $t^m$  is known, we need find out the approximate solution  $\{\psi_w^{m+1}, \psi_o^{m+1}, s^{m+1}\}$  at time  $t^{m+1}$ .

### 3.2 Numerical Simulation and Analysis of Dongying Hollow

As for the practical situation of Dongying Hollow of Shengli Oil Field, we did quasi-three-dimensional numerical simulation tests. Dongying Hollow is a main oil-bearing region. It is also a typical representative of oil- and gas-bearing regions in the eastern land fault. Up to now, the quantitative simulation and evaluation of the oil and gas deposits in this area have been made twice, yet there still has not been enough systematic study about or quantitative simulation of the secondary migration of the oil and gas in this area, and its kinetics in particular. Therefore, it is of practical value to take Dongying Hollow as the study target (Wang and Guan, 1999; Cha, 1997).

*Simulation region:* Dongying Hollow region, earth coordinate (m) (20593246.00, 4119110.00) and (20639246.00, 4159110.00). Mesh step = 2000 m.

*Geological parameters:* The geological parameters, offered by Shengli Oil Field, include absolute permeability, porosity, water displacement, oil displacement, etc.

*Numerical simulation result and analysis:* Time step =  $10^3$  years and total simulation time =  $2.5 \times 10^7$  years. Simulation result includes potential function for the oil and water phase (Figs. 5a and 5b) and concentration (Fig. 6).

According to the numerical simulation results, the oil deposits in the Dongying Hollow region were mainly accumulated during the latter five million years. Before

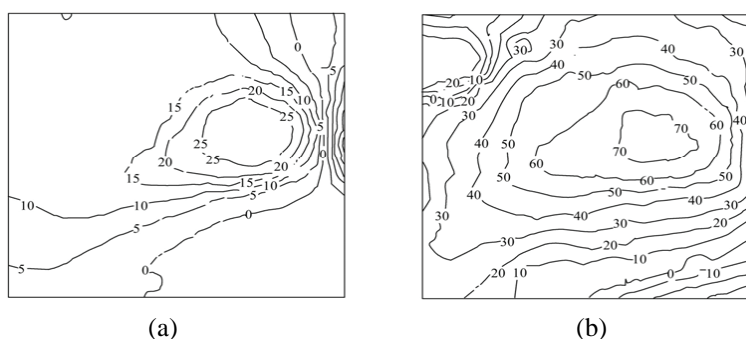


FIG. 5: a)  $2.5 \times 10^7$  year's water potential isograms; b)  $2.5 \times 10^7$  year's oil potential isograms

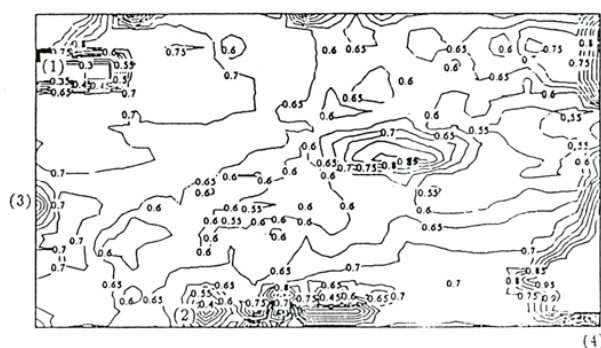


FIG. 6:  $2.5 \times 10^7$  year's water saturation isogram: (1) Shanyiasi oil field, (2) Chunhua oil field, (3) Qiaozhuang oil field, (4) Baminanhe oil field

that, there was only water flow, i.e., the flow of oil didn't from. Numerical results agree with the physical mechanics characteristics of oil-water migration and accumulation. Oil migrates from a higher potential to a lower one, and finally accumulates in an area of low oil potential, verifying the stability and reliability of the numerical simulation method. Oil deposits (1), (2), (3), and (4) determined by numerical simulation tally basically with Shanyiasi, Chunhua, Qiaozhuang, and Baminanhe oil fields, respectively, which illustrates the accuracy of the numerical simulation method.

Let us choose the whole Dongying Hollow sand four upper region to conduct the three-dimensional numerical simulation of migration and accumulation. The characteristics are (i) the simulation area is large at  $142 \times 84$  km, (ii) here the generation and displacement amount of hydrocarbon is great, (iii) and the migration-accumulation time is as long as over 30 million years.

Thus, this choice has particular significance. Namely, it can examine the adaptability of this software to large-scale numerical simulation and the stability of this software during tens of millions of years. The final simulation results will provide petrogeologists with a scientific basis for their rational evaluation of the oil-bearing potential and oil distribution in this area.

The simulation region was the Dongying Hollow region, earth coordinate (m) (20 552 246.00, 20 694 246.00) and (4 090 110.00, 4 174 110.00), horizontal scale =  $142,000 \times 84,000$  m, vertical span = 1,863 m, total simulation time =  $3.0 \times 10^7$  years, time step = 100 years, and horizontal mesh number =  $71 \times 42$ . We divide the sand layer into five layers from above to below, mesh steps:  $\Delta x = \Delta y = 2,000$  m,  $\Delta z = 100$  m.

In order for the calculation to be adaptable to the differences in hydrocarbon and the fluid displacement in different geologic periods, instead of the exchanging time step technique, we have adopted a time step of  $\sim 200$ – $1000$  years. Here are isograms of water saturation in different beds of sand four upper during simulation time  $3.25 \times 10^7$  years (Figs. 7a–7c).

The results of numerical simulation indicate the following.

1. Three-dimensional numerical simulation of immiscible flow mechanics demonstrates the whole process of secondary migration and accumulation in the actual three-dimensional sphere. Simulation results agree with immiscible flow mechanics features of oil-water migration and accumulation. When oil reaches a certain degree of saturation, it, under the joint actions of oil and water potentials, migrates from a higher potential to a lower one in the three-dimensional sphere, accumulates in an area with low



oil potential, and forms deposits. The longer the time, the larger the amount of hydrocarbon displacement, and the more oil accumulates. Finally, oil accumulates in areas with low oil potential and forms deposits.

2. When the numerical simulation results are compared with the actual locations of oil fields in Dongying Hollow, it can be found out that they tally basically with each other, and so do the reserve amount and the simulation results.
3. The duration of successful numerical simulation, which is up to tens of millions of years long, proves the high stability, accuracy, and efficiency of this numerical simulation method.

#### 4. THE LARGE-SCALE ACCURATE PARALLEL NUMERICAL SIMULATION OF MIGRATION AND ACCUMULATION

We, from the actual conditions in production, studied large-scale accurate parallel numerical simulation of multilayer oil migration and accumulation. We put forward a mathematical model and a careful parallel operator splitting-up implicit iterative scheme, parallel arithmetic program, parallel arithmetic information transmission, and alternating-direction mesh subdivision. It has produced a first at-home and abroad software system of resources evaluation and multilayer oil resources migration and accumulation. This system has successfully been applied in oil resources evaluation in Huimin Hollow (two layers), Dongying Hollow (four layers), Tanhai Region (three layers), and Yangxin Hollow (four layers).

For the numerical simulation of secondary multilayer oil migration in porous media, the flow in the first and third layers is considered as horizontal, and in the one between them as vertical. After careful analysis of the model and the scientific numerical tests, we propose a creative and rational numerical model. For the mathematical model of multilayer migration accumulation (Fig. 8),

$$\begin{aligned} & \nabla \cdot \left( K_1 \frac{k_{ro}}{\mu_o} \nabla \psi_o \right) + B_o q - \left( K_3 \frac{k_{ro}}{\mu_o} \frac{\partial \psi_o}{\partial z} \right)_{z=H_1} \\ & = -\Phi \dot{s} \left( \frac{\partial \psi_o}{\partial t} - \frac{\partial \psi_w}{\partial t} \right), X = (x, y)^T \in \Omega_1 \\ & t \in J = (0, T] \end{aligned} \tag{19a}$$

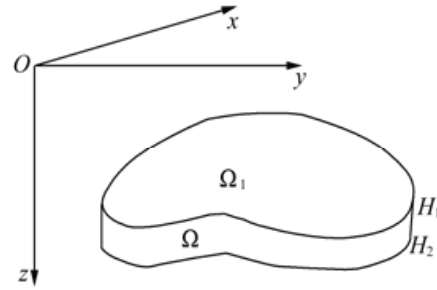


FIG. 8: Two-layer sketch map of regions  $\Omega_1, \Omega$

$$\begin{aligned} & \nabla \cdot \left( K_1 \frac{k_{rw}}{\mu_w} \nabla \psi_w \right) + B_w q - \left( K_3 \frac{k_{rw}}{\mu_w} \frac{\partial \psi_w}{\partial z} \right)_{z=H_1} \\ & = \Phi \dot{s} \left( \frac{\partial \psi_o}{\partial t} - \frac{\partial \psi_w}{\partial t} \right), X \in \Omega_1 \\ & t \in J \end{aligned} \tag{19b}$$

$$\begin{aligned} & \frac{\partial}{\partial z} \left( K_3 \frac{k_{ro}}{\mu_o} \frac{\partial \psi_o}{\partial z} \right) = -\Phi \dot{s} \left( \frac{\partial \psi_o}{\partial t} - \frac{\partial \psi_w}{\partial t} \right) \\ & X = (x, y, z)^T \in \Omega, t \in J \end{aligned} \tag{20a}$$

$$\begin{aligned} & \frac{\partial}{\partial z} \left( K_3 \frac{k_{rw}}{\mu_w} \frac{\partial \psi_w}{\partial z} \right) = \Phi \dot{s} \left( \frac{\partial \psi_o}{\partial t} - \frac{\partial \psi_w}{\partial t} \right) \\ & X \in \Omega, t \in J \end{aligned} \tag{20b}$$

$$\begin{aligned} & \nabla \cdot \left( K_2 \frac{k_{ro}}{\mu_o} \nabla \psi_o \right) + B_o q + \left( K_3 \frac{k_{ro}}{\mu_o} \frac{\partial \psi_o}{\partial z} \right)_{z=H_2} \\ & = -\Phi \dot{s} \left( \frac{\partial \psi_o}{\partial t} - \frac{\partial \psi_w}{\partial t} \right), X = (x, y)^T \in \Omega_1 \\ & t \in J \end{aligned} \tag{21a}$$

$$\begin{aligned} & \nabla \cdot \left( K_2 \frac{k_{rw}}{\mu_w} \nabla \psi_w \right) + B_w q + \left( K_3 \frac{k_{rw}}{\mu_w} \frac{\partial \psi_w}{\partial z} \right)_{z=H_2} \\ & = \Phi \dot{s} \left( \frac{\partial \psi_o}{\partial t} - \frac{\partial \psi_w}{\partial t} \right), X \in \Omega_1 \\ & t \in J \end{aligned} \tag{21b}$$

where  $\psi_o$  and  $\psi_w$  are the potential functions, and  $k_{ro}$  and  $k_{rw}$  are the relative permeabilities for the oil and water phases, respectively.  $K_1, K_2,$  and  $K_3$  are the absolute permeabilities in respective layers.  $\mu_o$  and  $\mu_w$  are the viscosities for the oil and water phases.  $\dot{s} = ds/dp_c$ , where  $s$

is the water concentration and  $p_c$  is the capillary pressure.  $B_o$  and  $B_w$  are the flow coefficients,

$$B_o = \frac{k_{ro}}{\mu_o} \left( \frac{k_{ro}}{\mu_o} + \frac{k_{rw}}{\mu_w} \right)^{-1}, \quad B_w = \frac{k_{rw}}{\mu_w} \left( \frac{k_{ro}}{\mu_o} + \frac{k_{rw}}{\mu_w} \right)^{-1}$$

$q(x, t)$  are the source (sink) functions.

By Darcy's law,  $-K_3(k_{ro}/\mu_o)(\partial\psi_o/\partial z) = q_{h,o}$ ,  $-K_3(k_{rw}/\mu_w)(\partial\psi_w/\partial z) = q_{h,w}$ . And the initial conditions and boundary conditions are given.

The following quasi-three-dimensional numerical schemes can be used to do numerical computation.

The first layer scheme:

$$\begin{aligned} & \nabla \cdot \left( \bar{K}_1 \Delta z_1 \frac{k_{ro}}{\mu_o} \nabla \psi_o \right) + B_o \bar{q} \Delta z_1 + q_{h,o}^1 \\ & = -\Phi \dot{s} \left( \frac{\partial \psi_o}{\partial t} - \frac{\partial \psi_w}{\partial t} \right), \quad X \in \Omega_1 \\ & t \in J \end{aligned} \quad (22a)$$

$$\begin{aligned} & \nabla \cdot \left( \bar{K}_1 \Delta z_1 \frac{k_{rw}}{\mu_w} \nabla \psi_w \right) + B_w \bar{q} \Delta z_1 + q_{h,w}^1 \\ & = \Phi \dot{s} \left( \frac{\partial \psi_o}{\partial t} - \frac{\partial \psi_w}{\partial t} \right), \quad X \in \Omega_1 \\ & t \in J \end{aligned} \quad (22b)$$

where  $\bar{K}_1 = (1/\Delta z_1) \int_{h_1^1(x,y)}^{h_2^1(x,y)} K_1(x, y, z) dz$ ,  $\bar{\Phi} = (1/\Delta z_1) \int_{h_1^1(x,y)}^{h_2^1(x,y)} \Phi(x, y, z) dz$ ,  $\bar{q} = (1/\Delta z_1) \int_{h_1^1(x,y)}^{h_2^1(x,y)} q(x, y, z) dz$ .

The second layer scheme:

$$\begin{aligned} & \nabla \cdot \left( \bar{K}_2 \Delta z_2 \frac{k_{ro}}{\mu_o} \nabla \psi_o \right) + B_o \bar{q} \Delta z_2 - q_{h,o}^2 \\ & = -\Phi \dot{s} \left( \frac{\partial \psi_o}{\partial t} - \frac{\partial \psi_w}{\partial t} \right), \quad X \in \Omega_1 \\ & t \in J \end{aligned} \quad (23a)$$

$$\begin{aligned} & \nabla \cdot \left( \bar{K}_2 \Delta z_2 \frac{k_{rw}}{\mu_w} \nabla \psi_w \right) + B_w \bar{q} \Delta z_2 - q_{h,w}^2 \\ & = \Phi \dot{s} \left( \frac{\partial \psi_o}{\partial t} - \frac{\partial \psi_w}{\partial t} \right), \quad X \in \Omega_1 \\ & t \in J \end{aligned} \quad (23b)$$

where  $\bar{K}_2 = (1/\Delta z_2) \int_{h_1^2(x,y)}^{h_2^2(x,y)} K_2(x, y, z) dz, \dots, q_{h,o}^1 \approx q_{h,o}^2$ ,  $q_{h,w}^1 \approx q_{h,w}^2$ . Numerical schemes (22) and (23) are

combined by applying Darcy's law. Compute Eqs. (22) and (23), respectively, by the scheme proposed by the quasi-three-dimensional problem in Section 3. The two layers between them are coupled by Darcy's law as

$$\begin{aligned} q_{h,o}^1 = q_{h,o}^2 = & \frac{-1}{2} \left\{ \bar{K}_1 \left( \frac{k_{ro}}{\mu_o} \right)_1 + \bar{K}_2 \left( \frac{k_{ro}}{\mu_o} \right)_2 \right\} \\ & \times \frac{(\psi_{o,2} - \psi_{o,1})}{\Delta z} \end{aligned} \quad (24a)$$

$$\begin{aligned} q_{h,w}^1 = q_{h,w}^2 = & -\frac{1}{2} \left\{ \bar{K}_1 \left( \frac{k_{rw}}{\mu_w} \right)_1 + \bar{K}_2 \left( \frac{k_{rw}}{\mu_w} \right)_2 \right\} \\ & \times \frac{(\psi_{w,2} - \psi_{w,1})}{\Delta z} \end{aligned} \quad (24b)$$

The arithmetic program of the numerical simulation of secondary multilayer oil migration in porous media for a time step is as follows. Assuming that the approximate solution  $\{\psi_w^m, \psi_o^m, s^m\}$  at time  $t = t^m$  is known, one needs to find out the approximate solution  $\{\psi_w^{m+1}, \psi_o^{m+1}, s^{m+1}\}$  at time  $t = t^{m+1}$ . First, we propose the solution of Eqs. (19) and (21) by reducing them to the quasi-three-dimensional problems of (22) and (23). In this time, the coefficient of the equations takes knowing functions at  $t^m$ ,  $B_o^m = B_o(s^m)$ ,  $B_w^m = B_w(s^m), \dots$ . Because the vertical flow layer is very thin, we can apply Darcy's law (24) instead Eq. (2), and take

$$\begin{aligned} q_{h,o}^1 = q_{h,o}^2 = & -\frac{1}{2} \left\{ \bar{K}_1 \left[ \frac{k_{ro}}{\mu_o}(s^m) \right]_1 \right. \\ & \left. + \bar{K}_2 \left[ \frac{k_{ro}}{\mu_o}(s^m) \right]_2 \right\} (\psi_{o,2}^m - \psi_{o,1}^m) / \Delta z \\ q_{h,w}^1 = q_{h,w}^2 = & -\frac{1}{2} \left\{ \bar{K}_1 \left[ \frac{k_{rw}}{\mu_w}(s^m) \right]_1 \right. \\ & \left. + \bar{K}_2 \left[ \frac{k_{rw}}{\mu_w}(s^m) \right]_2 \right\} (\psi_{w,2}^m - \psi_{w,1}^m) / \Delta z \end{aligned}$$

At this time, the modified method of second-order splitting-up implicit iterative schemes (17) and (18) in Section 3 can be used in parallel to compute two quasi-three-dimensional problems, Eqs. (22) and (23). At last, we can obtain the approximate solution  $\{\psi_w^{m+1}, \psi_o^{m+1}, s^{m+1}\}$ .

Thus, this important problem can be successfully solved. This method can be used in solving multilayer problems.

#### 4.1 Parallel Arithmetic Method and Program

Since the end of the twentieth century, parallel computation techniques have been rapidly developed in the world. This provides very good hardware and software conditions for our study on the careful quantitative simulation of oil secondary migration and parallel computation techniques. We use high-performance computer groups and an MPI information transmission programming system, which is composed of the existing 32 nodes and SCI ultramicro service units (eight CPUs of four nodes) and is based on a Turbolinux and REDHat 7.4 Scal operation system. In parallel computation, a new careful parallel alternating direction implicit iterative method is adopted. There are three kinds of information transmission treatment. Actual geological parameters of Tanhai Region, Shengli Oilfield are put to use. Parallel computation is conducted for different node combinations and mesh divisions. The results tally with the actual situations.

Our study, based on existing hardware and software, aims at designing parallel computation, raising computation efficiency, and increasing industrial production with the following features.

- (1) The configuration of computer groups of 32 nodes: Each node: cpu: intel P3 800MHz, mem: 512MB, HD: 55GB. Two service units: Service Unit: cpu: intol P3 700MHz, mem: 1GB, IID: 00GB. Service Unit: cpu: intel P3 700MHz, mem: 1GB, HD: 90GB. Disk exhibition cabinet 800GB. Two Switches (3COM 3900) 1000MB×6. Operation system: Turbolinux 7.0. Parallel programming of information transmission: MPICH2.24.
- (2) SCI ultramicro-service units: 4 nodes, double cpu: P41.8G, mem: 512MB, HD: 30GB×2.

The structure of the procedure module is illustrated in Fig. 9 and the meaning of each step is shown as follows.

1. From the result files of the “3D basin simulation system,” take the layer top, depth of burying, and the quantities of liquids and hydrocarbons discharge of the layer in geological age.
2. With the keyboard or digital equipment, put in the burying depth of sand top of the simulation layer, the thickness of the sand layer, the porosity, permeability, and so on.
3. From the exploration database, take out the burying depth of sand top of the simulation layer, the thickness of the sand layer, the porosity, permeability, and so on.

4. Check the comprehensive data.
5. Simulation computation.
6. Serial monolayer simulation computation.
7. Serial 3D simulation computation.
8. Serial multilayer simulation computation.
9. Choose parallel computation.
10. Parallel monolayer simulation computation.
11. Parallel 3D simulation computation.
12. Parallel multilayer simulation computation.
13. Processing simulation results.
14. Geoanalysis and interpretation.
15. 3-D visible diagram.

#### 4.2 Validity Analysis of Carefully Parallel Arithmetic of Tanhai Region

We adopt the geology parameters of the Tanhai Region. Simulation region: Tanhai Region, earth coordinate (m) (20611700.00, 4169000.00) and (2071700.00, 4253000.00), horizontal scale, 8845.2 km<sup>2</sup>. The simulation includes two layers, that is, Sand Third Upper Section and Sand Third Middle Section. According to the structure of Tanhai Region, Chengzikou-Qingyun Ridge, Yihezhuang-Wudiningjin Ridge, Chenjiazhuang-Binxian Ridge, and Qingtuozi-Kendong Ridge are located from northwest to southeast. In between horizontally located are Chengbei Hollow, Huanghekou Hollow, Bonan Hollow, Gunan Hollow, and other oil-bearing hollows.

Simulation results in Figs. 10a and 10b show the present oil-concentration isograms in these two layers during  $3.0 \times 10^7$  years. The results of numerical simulation indicate that the oil in Sand third middle region migrates along the fault towards Sand Third Upper Region and accumulates on the uplifted zone around the low-lying area and on the slope, that is, Chengdao area, Laohekao, Stake No. 5, and Gudong area. The present situation of oil exploration of Shengli Oilfield is basically the same.

The above computation and analysis indicate that our large-scale careful parallel numerical simulation system (when mesh step length is 200 m) can perform precise numerical simulation by using 3D seismic interpretation results without losing a single small stratigraphic trap and,

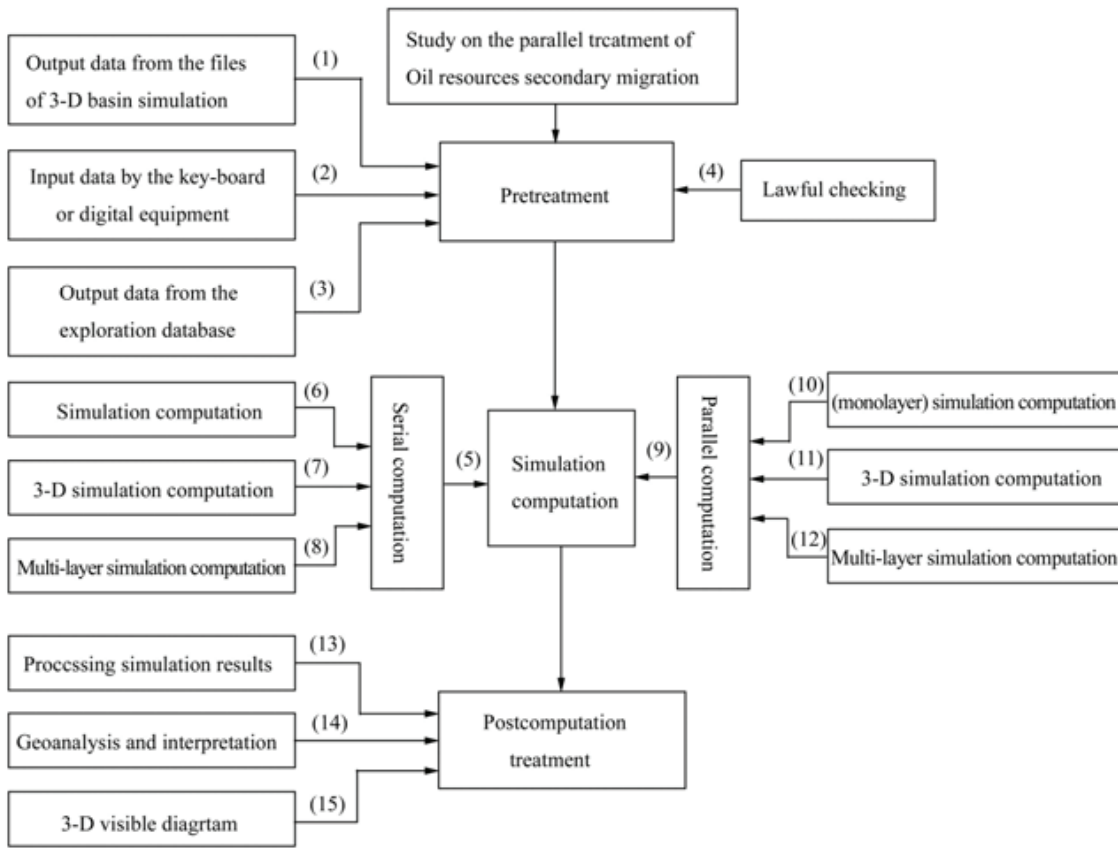


FIG. 9: The structure of the procedure module

therefore, can be used to evaluate present oil resources and explore new oil fields.

## 5. NUMERICAL ANALYSIS OF THE MODEL PROBLEM

As for the numerical method of oil migration and accumulation of the multilayer in porous media, for the sake of brevity, we consider one simple model problem, i.e., the nonstationary flow computation of multilayer fluid dynamics in porous media. We have to find out the following nonlinear convection-dominated diffusion coupling systems with a moving boundary value problem (Catalan 1992; Yuan, 1999, 1992):

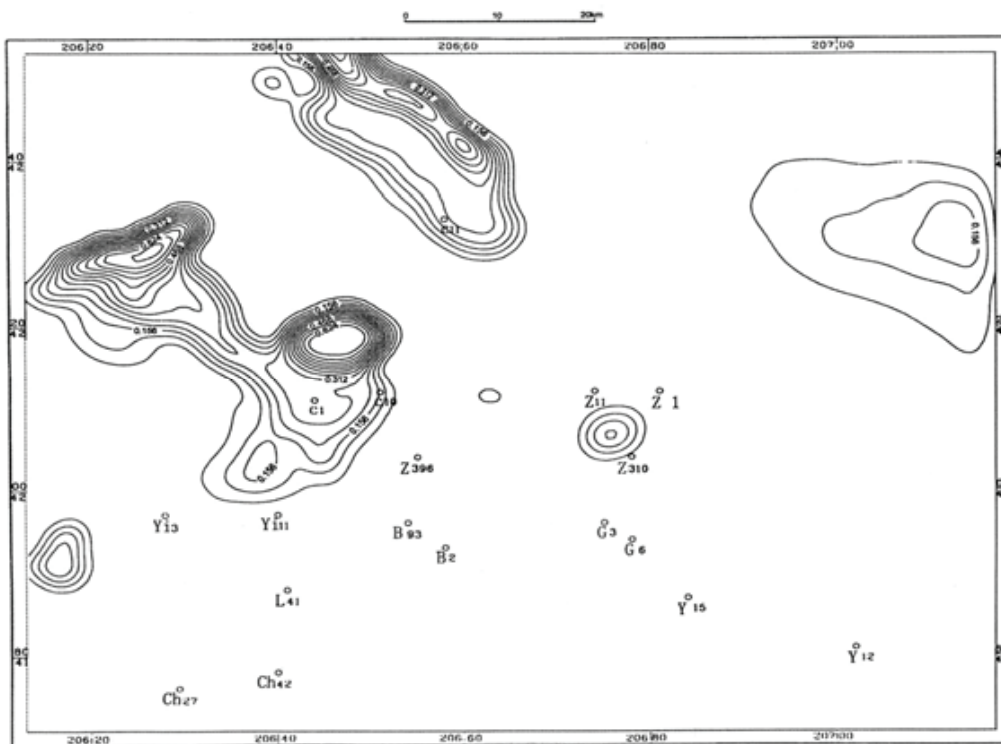
$$\begin{aligned} \Phi_1(x, y, t) \frac{\partial u}{\partial t} + \bar{a}(x, y, t) \cdot \nabla u - \nabla \cdot [K_1(x, y, t) \nabla u] \\ - K_2(x, y, z, t) \frac{\partial w}{\partial z} \Big|_{z=\mu(t)} = Q_1(x, y, t, u) \\ (x, y)^T \in \Omega(t), t \in J = (0, T] \end{aligned} \quad (25a)$$

$$\begin{aligned} \Phi_2(x, y, z, t) \frac{\partial w}{\partial t} = \frac{\partial}{\partial z} \left[ K_2(x, y, z, t) \frac{\partial w}{\partial z} \right] \\ (x, y, z)^T \in \Omega, H(t), t \in J \end{aligned} \quad (25b)$$

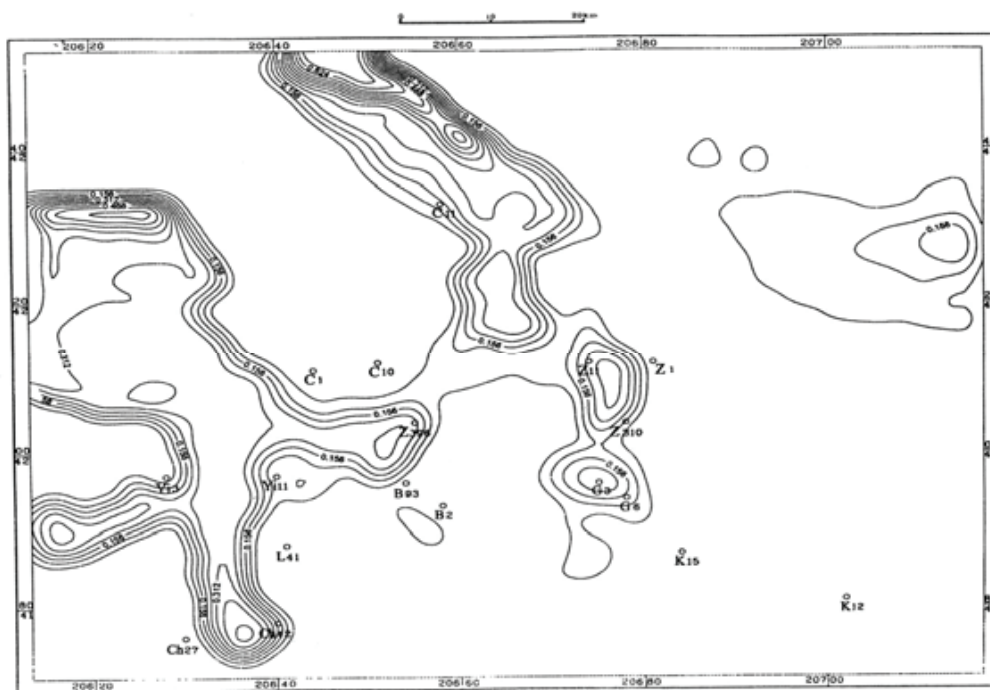
$$\begin{aligned} \Phi_3(x, y, t) \frac{\partial v}{\partial t} + \bar{b}(x, y, t) \cdot \nabla u - \nabla \cdot [K_3(x, y, t) \nabla v] \\ + K_2(x, y, z, t) \frac{\partial w}{\partial z} \Big|_{z=0} = Q_3(x, y, t, v) \\ (x, y)^T \in \Omega(t), t \in J \end{aligned} \quad (25c)$$

where

$$\begin{aligned} \Omega(t) &= \{X \mid \chi_1(t) \leq x \leq \chi_2(t), \sigma_1(t) \leq y \leq \sigma_2(t), t \in J\}, \Theta(t) \\ &= \{(x, y, z) \mid \chi_1(t) \leq x \leq \chi_2(t), \sigma_1(t) \leq y \leq \sigma_2(t), 0 \leq z \leq \mu(t), t \in J\} \\ \nabla &= \left( \frac{\partial}{\partial x}, \frac{\partial}{\partial y} \right)^T \end{aligned}$$



(a)



(b)

**FIG. 10:** a)  $3.0 \times 10^7$  year's Sand Third Upper oil concentration isograms; b)  $3.0 \times 10^7$  years' Sand Third Middle oil concentration isograms



The boundary conditions are

$$\begin{aligned} u(x, y, t)|_{\partial\Omega(t)} = 0, w(x, y, z, t)|_{(x,y)^T \in \partial\Omega(t), z \in (0, \mu(t))} \\ = 0, v(x, y, t)|_{\partial\Omega(t)} = 0 \end{aligned} \quad (26a)$$

$$\begin{aligned} w(x, y, z, t)|_{z=\mu(t)} = u(x, y, t), w(x, y, z, t)|_{z=0} \\ = v(x, y, t), (x, y)^T \in \Omega(t), t \in J \\ \text{(interior boundary condition)} \end{aligned} \quad (26b)$$

The initial conditions are

$$\begin{aligned} u(x, y, 0) = u_0(x, y), (x, y)^T \in \Omega(0), w(x, y, z, 0) \\ = w_0(x, y, z), (x, y, z)^T \in \Theta(0) \\ v(x, y, 0) = v_0(x, y), (x, y)^T \in \Omega(0) \end{aligned} \quad (27)$$

The unknown functions  $u$ ,  $w$ , and  $v$  are the potential functions.  $\nabla u$ ,  $\nabla v$ , and  $\partial w/\partial z$  are Darcy's velocity.  $\Phi_\alpha$  ( $\alpha = 1, 2, 3$ ) is the porosity,  $K_\alpha$  ( $\alpha = 1, 2, 3$ ) is the stratigraphical permeability,  $\bar{a}(x, y, t) = [a_1(x, y, t), a_2(x, y, t)]^T$ , and  $\bar{b}(x, y, t) = [b_1(x, y, t), b_2(x, y, t)]^T$  are the convection coefficients.  $Q_1(x, y, u)$ ,  $Q_2(x, y, v)$  are the external volumetric flow rates.

Let  $\Delta t = T/L$  be the time step and  $t^n = n\Delta t$ . For  $\Omega^n = \Omega(t^n)$ , we adopt an equidistant mesh of  $\chi_1(t^n) = x_0^n < x_1^n < \dots < x_{N_1}^n = \chi_2(t^n)$ ,  $\sigma_1(t^n) = y_0^n < y_1^n < \dots < y_{N_1}^n = \sigma_2(t^n)$ , and the point number is  $N_1 + 1$ . For  $\Theta^n = \Theta(t^n)$ , we also adopt equidistant mesh, and the point number is  $N_2 + 1$ . The space steps are  $h_1^n = [\chi_2(t^n) - \chi_1(t^n)]/N_1$ ,  $h_2^n = [\sigma_2(t^n) - \sigma_1(t^n)]/N_1$ , and  $h_3^n = \mu(t^n)/N_2$ . Let  $U(x_i^n, y_j^n, t^n) = U_{ij}^n$ ,  $V(x_i^n, y_j^n, t^n) = V_{ij}^n$ ,  $W(x_i^n, y_j^n, z_k^n, t^n) = W_{ijk}^n$ ,  $\delta_x, \delta_y, \delta_z$ , and  $\delta_{\bar{x}}, \delta_{\bar{y}}, \delta_{\bar{z}}$  be the forward and backward difference quotients, respectively.  $dt u_{ij}^n$  is the forward quotient of net function  $u_{ij}^n$ .

For Eq. (25a), the characteristic finite difference fractional steps scheme is given by

$$\begin{aligned} \hat{\Phi}_1(x_i^{n+1}, y_j^{n+1}, t^{n+1}) \frac{U_{ij}^{n+1/2} - \hat{U}_{ij}^n}{\Delta t} \\ = \delta_{\bar{x}}(K_1^n \delta_x U^{n+1/2})_{ij} + \delta_{\bar{y}}(K_1^n \delta_y U^n)_{ij} \\ + K_{2,ij,N_2-1/2}^{n+1} \delta_{\bar{z}} W_{ij,N_2}^{n+1} + Q_1(x_i^{n+1}, y_j^{n+1}, \hat{U}_{ij}^n) \\ 1 \leq i \leq N_1 - 1, 1 \leq j \leq N_1 - 1 \end{aligned} \quad (28a)$$

$$U_{ij}^{n+1/2} = 0, (i, j) \in \partial\Omega_h \quad (28b)$$

$$\begin{aligned} \hat{\Phi}_1(x_i^{n+1}, y_j^{n+1}, t^{n+1}) \frac{U_{ij}^{n+1} - U_{ij}^{n+1/2}}{\Delta t} \\ = \delta_{\bar{y}} [K_1^n \delta_y (U^{n+1} - U^n)]_{ij} \\ 1 \leq i \leq N_1 - 1, 1 \leq j \leq N_1 - 1 \end{aligned} \quad (28c)$$

$$U_{ij}^{n+1} = 0, (i, j) \in \partial\Omega_h \quad (28d)$$

where  $\hat{\Phi}_1(x, y, t) = \Phi_1(x, y, t) + (1/2)h_3\Phi_2[x, y, \mu(t), t]$ . We interpret  $U^n(X)$  as the piecewise biquadratic interpolation,  $\hat{U}_{ij}^n = U^n(\hat{X}_{1,ij}^n)$ ,  $\hat{X}_{1,ij}^n = X_{ij}^n - \bar{a}_{ij}^{n+1} \Delta t / \hat{\Phi}_{1,ij}^{n+1}$ .

For Eq. (25b), the finite difference scheme is

$$\begin{aligned} \Phi_2(x_i^{n+1}, y_j^{n+1}, z_k^{n+1}, t^{n+1}) \frac{W_{ijk}^{n+1} - W_{ijk}^n}{\Delta t} \\ = \delta_{\bar{z}}(K_2 \delta_z W)_{ijk}^{n+1} \\ 1 \leq i \leq N_1 - 1, 1 \leq j \leq N_1 - 1, 1 \leq k \leq N_2 - 1 \end{aligned} \quad (29a)$$

The boundary conditions are

$$\begin{aligned} W_{o,jk}^{n+1} = W_{N_1,jk}^{n+1} = W_{i,o,k}^{n+1} = W_{i,N_1,k}^{n+1} = 0 \\ W_{ij,N_2}^{n+1} = U_{ij}^{n+1}, W_{ij,o}^{n+1} = V_{ij}^{n+1} \end{aligned} \quad (29b)$$

For Eq. (25c), the characteristic finite difference fractional steps scheme is given by

$$\begin{aligned} \hat{\Phi}_3(x_i^{n+1}, y_j^{n+1}, t^{n+1}) \frac{V_{ij}^{n+1} - \hat{V}_{ij}^n}{\Delta t} \\ = \delta_{\bar{x}}(K_3^n \delta_x V^{n+1/2})_{ij} + \delta_{\bar{y}}(K_3^n \delta_y V^n)_{ij} \\ - K_{2,ij,1/2}^{n+1} \delta_z W_{ij,0}^{n+1} + Q_3(x_i^{n+1}, y_j^{n+1}, \hat{V}_{ij}^n) \\ 1 \leq i \leq N_1 - 1, 1 \leq j \leq N_1 - 1 \end{aligned} \quad (30a)$$

$$V_{ij}^{n+1/2} = 0, (i, j) \in \partial\Omega_h \quad (30b)$$

$$\begin{aligned} \hat{\Phi}_3(x_i^{n+1}, y_j^{n+1}, t^{n+1}) \frac{V_{ij}^{n+1} - V_{ij}^{n+1/2}}{\Delta t} \\ = \delta_{\bar{y}} [K_3^n \delta_y (V^{n+1} - U^n)]_{ij} \\ 1 \leq i \leq N_1 - 1, 1 \leq j \leq N_1 - 1 \end{aligned} \quad (30c)$$

$$V_{ij}^{n+1} = 0, (i, j) \in \partial\Omega_h \quad (30d)$$

where  $\hat{\Phi}_3(x, y, t) = \Phi_3(x, y, t) + \frac{1}{2}h_3\Phi_2(x, y, 0, t)$ . We interpret  $V^n(X)$  as the piecewise biquadratic interpolation,  $\hat{V}_{ij}^n = V^n(\hat{X}_{2,ij}^n)$ ,  $\hat{X}_{2,ij}^n = X_{ij}^{n+1} - \bar{b}_{ij}^{n+1} \Delta t / \hat{\Phi}_{3,ij}^{n+1}$ .

The algorithm for a time step is as follows. Assume that the approximate solution  $\{U_{ij}^n, W_{ijk}^n, V_{ij}^n\}$  at time  $t^n$

is known. It is needed to find out the approximate solution  $\{U_{ij}^{n+1}, W_{ijk}^n, V_{ijk}^{n+1}\}$  at time  $t^{n+1}$ . First, from schemes (28a) and (28b), we can obtain  $\{U_{ij}^{n+1/2}\}$ ; second, from (28c) and (28d), we obtain  $U_{ij}^{n+1}$ ; next, from (30a) and (30b), we can obtain  $\{V_{ij}^{n+1/2}\}$ ; from (30c) and (30d), we obtain  $\{V_{ij}^{n+1}\}$ ; and finally, from scheme (29) and interior boundary condition (26b), we obtain  $\{W_{ijk}^{n+1}\}$ . So a complete time step can be taken.

*Theorem:* Suppose that the exact solution of problems (25)–(27) satisfies a smooth condition. Adopt the modified characteristic finite difference fractional steps schemes (28)–(30). The following error estimate holds:

$$\begin{aligned} & \|u - U\|_{\bar{L}^\infty(J, h^1)} + \|v - V\|_{\bar{L}^\infty(J, h^1)} + \|w - W\|_{\bar{L}^\infty(J, h^1)} \\ & + \|d_t(u - U)\|_{\bar{L}^2(J, t^2)} + \|d_t(v - V)\|_{\bar{L}^2(J, t^2)} \\ & [2pt] + \|d_t(w - W)\|_{\bar{L}^2(J, t^2)} \leq M\{h^2 + \Delta t\} \end{aligned} \quad (31)$$

where

$$\begin{aligned} h &= \max_n \{h_1^n, h_2^n, h_3^n\}, \|g\|_{\bar{L}^\infty(J; X)} \\ &= \sup_{n \Delta t \leq T} \|g^n\|_X, \|g^n\|_{\bar{L}^2(J; X)} \\ &= \sup_{n \Delta t \leq T} \left\{ \sum_{n=0}^N \|g^n\|_X^2 \Delta t \right\}^{1/2} \end{aligned}$$

## 6. CONCLUSION

From geological science, geochemistry, permeation fluid mechanics, and computing techniques, this paper considers the theory, method, and application of numerical simulation of an oil-gas basin. The present paper is organized as follows. Section 1, Introduction, is a summary of basin circumstances. Section 2 is a study on numerical simulation and analysis of resources evaluation and actual application in Jiyang Depression of Shengli Oilfield. Section 3 is a study on the 3D numerical simulation of single-layer migration and accumulation and actual application in Dongying Hollow. Section 4 is a study on the large-scale accurate parallel numerical simulation of multilayer migration and accumulation and actual application in Huimin Hollow, Dongying Hollow, Tanhai Region, and Yangxin Hollow. Section 5 is a study on the theoretical analysis of the characteristic finite difference fractional steps method of multilayer migration-accumulation model problem, enabling our applied software numerical simulation system to be based on solid mathematic and

mechanic theories. In practical, the scientific research of the 3D multilayer numerical simulation of migration and accumulation is very difficult and complex. This paper does not consider the earthquake effect and migration and accumulation of gas resources. We must consider this from now on.

## REFERENCES

- Allen, P. A., Allen, J. R., and Chen, Q., *Basin Analysis: Principles and Application* (transl), Petroleum Press, Beijing, 1995.
- Catalan, L., An experimental study of secondary oil migration, *AAPG Bull.*, vol. 76, no. 5, pp. 638–650, 1992.
- Cha, M., *Secondary Hydrocarbon Migration and Accumulation*, Geology Press, Beijing, 1997.
- Dembicki, H., Jr., Secondary migration of oil experiments supporting efficient movement of separate, buoyant oil phase along limited conduits, *AAPG Bull.*, vol. 73, no. 8, pp. 1018–1021, 1989.
- Ewing, R. E., Mathematical modeling and simulation for multiphase flow in porous media, *Numerical Treatment of Multiphase Flows in Porous Media*, Lecture Notes in Physics, vol. 1552, Springer-Verlag, New York, pp. 43–57, 2000.
- Ewing, R. E., *The Mathematics of Reservoir Simulation*, SIAM, Philadelphia, 1983.
- Han, Y.-J., Wang, J., and Mao, J.-B., Basin numerical simulation (BNS) and its application, *Symposium on Methodology and Application of Oil and Gas Resources Evaluation*, Petroleum Industry Press, Beijing, 1988.
- Hubbert, M. K., Entrapment of petroleum under hydrodynamic conditions, *AAPG Bull.*, vol. 37, no. 8, pp. 1954–2026, 1953.
- Inst. of Math. of Shandong Univ. and Computer Centre of Shenghi Petroleum Administration: Study on Three-Dimensional Basin Simulation System, 1993.4.
- Inst. of Math. of Shandong Univ. and Computer Centre of Shenghi Petroleum Administration: Study on the Second Quantitative Simulation for Migration-Accumulation, 1997.12.
- Inst. of Math. of Shandong Univ. and Exploration Inst. of Shenghi Petroleum Administration: Study on the Multilayers for Oil Source Migration-Accumulation, 2001.4.
- Inst. of Math. of Shandong Univ. and Exploration Inst. of Shenghi Petroleum Administration: Study on Numerical Simulation of Oil Migration-Accumulation Passageway, 2005.10.
- Inst. of Math. of Shandong Univ. and Exploration Institute of Shenghi Petroleum Administration: Study on Careful Parallel Regional Numerical Simulation of Secondary Oil Migration-accumulation, 2004.10.

- Li, T.-M., *An Introduction to Quantitative Research for Petroleum Geology*, Petroleum University Press, Dongying, 1989.
- Shi, G.-R., *Numerical Simulation Method of Oil-Gas Basin*, Petroleum Press, Beijing, 1994.
- Ungerer, P., Burous, J., Doligez, B., Chenet, P. Y., Burus, J., Bessis, F., Lafargue, E., Giroir, G., Heum, O., and Eggen, S., A 2-D model of basin petroleum by two-phase fluid flow, application to some case studies, *Migration of Hydrocarbon in Sedimentary Basins*, Doligez, B., Ed., Editions Techniq., Paris, pp. 415–455, 1987.
- Ungerer, P., Fluid flow, hydrocarbon generation, and migration, *AAPE Bull.*, vol. 74, no. 3, pp. 309–335, 1990.
- Walte, D. H., Migration of hydrocarbons facts and theory, 2nd IFP Exploration Research Conference, Paris, 1987.
- Wang, J. and Guan, D., *The Model Study of Oil-Gas Migration-Accumulation*, Petroleum Press, Beijing, 1999.
- Welte, D. H. and Yukler, M. A., Petroleum origin and accumulation in basin evolution—A quantitative model, *AAPG Bull.*, vol. 65, no. 8, pp. 1387–1396, 1981.
- Yuan, Y.-R., The characteristic finite difference fractional steps method for compressible two-phase displacement problems, *Sci. China, (Ser. A)*, vol. 1, no. 42, pp. 48–57, 1999.
- Yuan, Y.-R., The upwind finite difference fractional steps method for combinatorial systems of dynamics of fluids in porous media and its application, *Sci. China, (Ser. A)*, vol. 45, no. 5, pp. 578–593, 2002.
- Yuan, Y.-Y., The finite difference method for the three-dimensional nonlinear coupled system of dynamics of fluids in porous media, *Sci. China, (Ser. A)*, vol. 49, no. 2, pp. 185–211, 2006.
- Yukler, M. A., Cornford, C., and Welte, D. H., One-dimensional model to simulate geologic hydrodynamic and thermodynamic development of a sedimentary basin, *Geol. Rundschau*, vol. 67, no. 3, pp. 960–979, 1978.
- Zeng, J.-H. and Jin, Z.-J., *Physical Simulation of Secondary Oil-gas Migration and Accumulation*, Petroleum Industry Press, Beijing, 2000.
- Zhang, H., Review and prospect of oil-gas migration, *Oil-Gas Migration Collected Works*, Zhang, H.-F., Ed., Petroleum University Press, Dongying, Shandong, pp. 3–6, 1995.

# ON FLEXURAL VIBRATIONS OF POROELASTIC CIRCULAR CYLINDRICAL SHELLS IMMERSSED IN AN ACOUSTIC MEDIUM

S. Ahmed Shah<sup>1,\*</sup> & M. Tajuddin<sup>2</sup>

<sup>1</sup>Department of Mathematics, Deccan College of Engineering and Technology, Hyderabad – 500 001 (AP) India

<sup>2</sup>Department of Mathematics, Osmania University, Hyderabad – 500 007 (AP) India

\*Address all correspondence to S. Ahmed Shah E-mail: ahmed\_shah67@yahoo.com

Original Manuscript Submitted: 5/11/2009; Final Draft Received: 7/3/2009

*Employing Biot's theory of wave propagation in liquid-saturated porous media, flexural vibrations of poroelastic circular cylindrical shells of different wall thicknesses and infinite extent immersed in an acoustic medium are investigated. Let the poroelastic cylindrical shells be homogeneous and isotropic. The frequency equation of flexural vibrations propagating in a poroelastic solid cylinder, each for a pervious and an impervious surface is obtained as a limiting case when the ratio of thickness to the inner radius tends to infinity as the inner radius tends to zero. Cutoff frequencies when the wave number is zero are obtained both for pervious and impervious surfaces. For zero wave number, the frequency equation of longitudinal shear vibrations is independent of nature of the surface, i.e., pervious or impervious, and is also independent of the presence of fluid within and around the poroelastic cylindrical shell. The nondimensional phase velocity for propagating modes is computed as a function of the ratio of thickness to wavelength in the absence of dissipation. Results are presented graphically for two types of poroelastic materials and then discussed. Previous results are shown as a special case of the present investigation. Results of purely elastic solid are obtained.*

**KEY WORDS:** Biot's theory, Flexural vibrations, poroelastic cylindrical shell, pervious surface, impervious surface, phase velocity, cut-off frequency

## 1. INTRODUCTION

Gazis (1959) discussed the propagation of free harmonic waves along a hollow elastic circular cylinder of infinite extent. Kumar (1971) studied the flexural vibrations of fluid-filled circular cylindrical shells. Employing Biot's (1956) theory, Tajuddin and Sarma (1980) studied torsional vibrations of poroelastic cylinders. Malla Reddy and Tajuddin (2000) studied plane-strain vibrations of thick-walled hollow poroelastic cylinders. Wisse et al. (2002) presented the experimental results of guided wave modes in porous cylinders. Kanj et al. (2003) presented the poromechanics of anisotropic hollow cylinders.

Chao et al. (2004) studied shock-induced borehole waves in porous formations. Tajuddin and Ahmed Shah (2006, 2007) studied circumferential waves and torsional vibrations of infinite hollow poroelastic cylinders in the presence of dissipation. Farhang et al. (2007) investigated wave propagation in transversely isotropic cylinders. Ahmed Shah (2008) investigated the axially symmetric vibrations of fluid-filled poroelastic cylindrical shells in the absence of dissipation.

In the present analysis, flexural vibrations of poroelastic circular cylindrical shells of various wall thicknesses and infinite extent immersed in an acoustic medium are investigated employing Biot's (1956) theory. Biot's

model consists of an elastic matrix permeated by a network of interconnected spaces saturated with liquid. The frequency equation of such vibrations is derived, each for a pervious surface and an impervious surface. Cutoff frequencies when the wave number is zero are obtained for pervious and impervious surfaces. For zero wave number, the frequency equation of longitudinal shear vibrations is independent of nature of surface as well as the presence of fluid within and around the poroelastic shell. This frequency equation is discussed for limiting values of the ratio of thickness to inner radius  $h/r_1$  when these values are too small and too large. When  $h/r_1 \rightarrow 0$ , it gives the frequencies of a thin poroelastic cylindrical shell, and when  $h/r_1 \rightarrow \infty$  with  $r_1 \rightarrow 0$ , modes of a poroelastic solid cylinder are obtained. The nondimensional phase velocity for propagating modes is computed in the absence of dissipation for poroelastic cylindrical shells immersed in an acoustic medium, each for a pervious and an impervious surface. The cutoff frequency as a function of  $h/r_1$  is determined. Results are presented graphically for two types of poroelastic materials and then discussed. Results of some previous works are shown as a special case of the present investigation. By ignoring liquid effects and after rearrangement of terms, results of a purely elastic solid are obtained.

The considered problem is applicable to deep-sea sound sources and transducers, petrochemical industries. In the field of acoustics, the shells are used as acoustic waveguides, ultrasonic delay lines, and frequency control devices.

## 2. GOVERNING EQUATIONS

The equations of motion of a homogeneous, isotropic poroelastic solid (Biot, 1956) in the presence of dissipation  $b$  are

$$\begin{aligned} N\nabla^2\vec{u} + (A + N)\nabla e + Q\nabla \epsilon & \\ = \frac{\partial^2}{\partial t^2}(\rho_{11}\vec{u} + \rho_{12}\vec{U}) + b\frac{\partial}{\partial t}(\vec{u} - \vec{U}) & \quad (1) \\ Q\nabla e + R\nabla \epsilon = \frac{\partial^2}{\partial t^2}(\rho_{12}\vec{u} + \rho_{22}\vec{U}) - b\frac{\partial}{\partial t}(\vec{u} - \vec{U}) & \end{aligned}$$

where  $\nabla^2$  is the Laplacian,  $\mathbf{u} = (u, v, w)$  and  $\mathbf{U} = (U, V, W)$  are displacements of solid and liquid, respectively,  $e$  and  $\epsilon$  are the dilatations of solid and liquid,  $A, N, Q$ , and  $R$  are all poroelastic constants, and  $\rho_{ij}$  ( $i, j = 1, 2$ ) are the mass coefficients following Biot (1956). The poroelastic constants  $A$  and  $N$  correspond to familiar Lamé constants in a purely elastic solid. The coefficient  $N$  represents the

shear modulus of solid. The coefficient  $R$  is a measure of pressure required on the liquid to force a certain amount of the liquid into the aggregate while the total volume remains constant. The coefficient  $Q$  represents the coupling between the volume change of a solid to that of liquid.

The equation of motion for a homogeneous, isotropic, inviscid elastic fluid is

$$\nabla^2\Phi = \frac{1}{V_f^2} \frac{\partial^2\Phi}{\partial t^2} \quad (2)$$

where  $\Phi$  is the displacement potential function and  $V_f$  is the velocity of sound in fluid. The displacement of fluid is  $\mathbf{u}_f = (u_f, v_f, w_f)$ .

The stresses  $\sigma_{ij}$  and the liquid pressure  $s$  of a poroelastic solid are

$$\begin{aligned} \sigma_{ij} &= 2Ne_{ij} + (Ae + Q\epsilon)\delta_{ij}, \quad (i, j = 1, 2, 3) \\ s &= Qe + R\epsilon \end{aligned} \quad (3)$$

where  $\delta_{ij}$  is the well-known Kronecker delta function.

The fluid pressure  $P_f$  is given by

$$P_f = -\rho_f \frac{\partial^2\Phi}{\partial t^2} \quad (4)$$

In Eq. (4),  $\rho_f$  is the density of the fluid.

The subscript “if” or “of” associated with a fluid quantity means that the quantity is related to either the inner or outer fluid. For example,  $V_{if}$  is the velocity of sound in the inner fluid and  $P_{of}$  is the outer fluid pressure.

## 3. SOLUTION OF THE PROBLEM

Let  $(r, \theta, z)$  be the cylindrical polar coordinates. Consider a homogeneous, isotropic, infinite poroelastic cylindrical shell immersed in an inviscid elastic fluid. Let the inner and outer radii of the poroelastic cylindrical shell be  $r_1$  and  $r_2$ , respectively, so that the wall thickness of the shell is  $h [= (r_2 - r_1) > 0]$ . The axis of the poroelastic shell is in the direction of the  $z$ -axis. The fluid column within the poroelastic cylindrical shell extends from zero to infinity in the axial direction and zero to  $r_1$  in the radial direction. The outer fluid extends from  $r_2$  to infinity in the radial direction and zero to infinity in the axial direction. Then for flexural vibrations, the displacement of a solid  $\mathbf{u} = (u, v, w)$ , which can readily be evaluated from field Eq. (1) when  $|kV_1| < \omega$ , is

$$\begin{aligned}
 u(r, \theta, z, t) &= \left\{ C_1 \frac{\partial}{\partial r} J_1(\alpha_1 r) + C_2 \frac{\partial}{\partial r} Y_1(\alpha_1 r) \right. \\
 &+ C_3 \frac{\partial}{\partial r} J_1(\alpha_2 r) + C_4 \frac{\partial}{\partial r} Y_1(\alpha_2 r) + \frac{A_3}{r} J_1(\alpha_3 r) \\
 &+ \left. \frac{B_3}{r} Y_1(\alpha_3 r) + A_1 2ik J_2(\alpha_3 r) + B_1 2ik Y_2(\alpha_3 r) \right\} \\
 &\times \cos \theta e^{i(kz + \omega t)} \\
 v(r, \theta, z, t) &= \left\{ -C_1 \frac{1}{r} J_1(\alpha_1 r) - C_2 \frac{1}{r} Y_1(\alpha_1 r) \right. \\
 &- C_3 \frac{1}{r} J_1(\alpha_2 r) - C_4 \frac{1}{r} Y_1(\alpha_2 r) - A_3 \frac{\partial}{\partial r} J_1(\alpha_3 r) \\
 &- \left. B_3 \frac{\partial}{\partial r} Y_1(\alpha_3 r) + A_1 2ik J_2(\alpha_3 r) + B_1 2ik Y_2(\alpha_3 r) \right\} \\
 &\times \sin \theta e^{i(kz + \omega t)} \\
 w(r, \theta, z, t) &= \left\{ C_1 ik J_1(\alpha_1 r) + C_2 ik Y_1(\alpha_1 r) \right. \\
 &+ C_3 ik J_1(\alpha_2 r) + C_4 ik Y_1(\alpha_2 r) - A_3 \frac{2}{r} J_1(\alpha_3 r) \\
 &- \left. B_3 \frac{2}{r} Y_1(\alpha_3 r) - A_1 2 \frac{\partial}{\partial r} J_2(\alpha_3 r) - B_1 2 \frac{\partial}{\partial r} Y_2(\alpha_3 r) \right\} \\
 &\times \cos \theta e^{i(kz + \omega t)} \quad (5)
 \end{aligned}$$

where  $C_1, C_2, C_3, C_4, A_3, B_3, A_1,$  and  $B_1$  are constants,  $k$  is the wave number,  $\omega$  is the frequency of the wave,  $J_1$  and  $J_2$  are Bessel functions of the first kind of order one and two, respectively, and  $Y_1$  and  $Y_2$  are Bessel functions of the second kind of order one and two, respectively. Here,  $i$  is a complex number and

$$\alpha_1^2 = \frac{\omega^2}{V_1^2} - k^2, \alpha_2^2 = \frac{\omega^2}{V_2^2} - k^2, \alpha_3^2 = \frac{\omega^2}{V_3^2} - k^2 \quad (6)$$

In Eq. (6),  $V_1, V_2,$  and  $V_3$  are dilatational wave velocities of the first and second kind and shear wave velocity, respectively (Biot, 1956). The displacement of the inner fluid column  $\mathbf{u}_{if} = (u_{if}, v_{if}, w_{if})$  for flexural vibrations is

$$\begin{aligned}
 u_{if} &= A_{if} \frac{\partial}{\partial r} J_1(\alpha_{if} r) \cos \theta e^{i(kz + \omega t)} \\
 v_{if} &= -\frac{A_{if}}{r} J_1(\alpha_{if} r) \sin \theta e^{i(kz + \omega t)} \quad (7) \\
 w_{if} &= A_{if} ik J_1(\alpha_{if} r) \cos \theta e^{i(kz + \omega t)}
 \end{aligned}$$

where  $A_{if}$  is a constant and

$$\alpha_{if}^2 = \frac{\omega^2}{V_{if}^2} - k^2 \quad (8)$$

With the help of the displacement potential function, the inner fluid pressure is given by

$$\begin{aligned}
 P_{if} &= A_{if} \omega^2 \rho_{if} J_1(\alpha_{if} r) \cos \theta e^{i(kz + \omega t)} \\
 &\text{when } |kV_{if}| < \omega \quad (9)
 \end{aligned}$$

Similarly, the displacement of the outer fluid and the outer fluid pressure are given by the equations

$$\begin{aligned}
 u_{of} &= A_{of} \frac{\partial}{\partial r} H_1^{(1)}(\alpha_{of} r) \cos \theta e^{i(kz + \omega t)} \\
 v_{of} &= -\frac{A_{of}}{r} H_1^{(1)}(\alpha_{of} r) \sin \theta e^{i(kz + \omega t)} \quad (10) \\
 w_{of} &= A_{of} ik H_1^{(1)}(\alpha_{of} r) \cos \theta e^{i(kz + \omega t)} \\
 P_{of} &= A_{of} \omega^2 \rho_{of} H_1^{(1)}(\alpha_{of} r) \cos \theta e^{i(kz + \omega t)}
 \end{aligned}$$

where  $A_{of}$  is a constant,  $H_n^{(1)}$  is Hankel function of the first kind and order  $n$ , and

$$\alpha_{of}^2 = \frac{\omega^2}{V_{of}^2} - k^2 \quad (11)$$

For imaginary values of  $\alpha_{of}$ , i.e., when the phase velocity  $\{\omega/k\}$  is less than  $V_{of}$  (velocity of sound in the outer fluid), the Hankel function of the first kind  $H_1^{(1)}(\alpha_{of} r)$  is replaced by modified Bessel function of the second kind  $K_1(\alpha_{of} r)$ .

Substituting the displacement function  $u, v, w$  from Eq. (5) and the fluid pressures from Eqs. (9) and (10) into Eq. (3), and with the help of Eq. (7), the relevant displacement, liquid pressure, and stresses are

$$\begin{aligned}
 \sigma_{rr} + s + P_{if} &= [C_1 M_{11}(r) + C_2 M_{12}(r) \\
 &+ C_3 M_{13}(r) + C_4 M_{14}(r) + A_3 M_{15}(r) + B_3 M_{16}(r) \\
 &+ A_1 M_{17}(r) + B_1 M_{18}(r) + A_{if} M_{19}(r)] \\
 &\times \cos \theta e^{i(kz + \omega t)} \quad (12)
 \end{aligned}$$

$$\begin{aligned}
 \sigma_{r\theta} &= [C_1 M_{21}(r) + C_2 M_{22}(r) + C_3 M_{23}(r) \\
 &+ C_4 M_{24}(r) + A_3 M_{25}(r) + B_3 M_{26}(r) \\
 &+ A_1 M_{27}(r) + B_1 M_{28}(r)] \sin \theta e^{i(kz + \omega t)} \quad (13)
 \end{aligned}$$

$$\begin{aligned}
 \sigma_{rz} &= [C_1 M_{31}(r) + C_2 M_{32}(r) + C_3 M_{33}(r) \\
 &+ C_4 M_{34}(r) + A_3 M_{35}(r) + B_3 M_{36}(r) + A_1 M_{37}(r) \\
 &+ B_1 M_{38}(r)] \cos \theta e^{i(kz + \omega t)} \quad (14)
 \end{aligned}$$

$$\begin{aligned}
 s &= [C_1 M_{41}(r) + C_2 M_{42}(r) + C_3 M_{43}(r) \\
 &+ C_4 M_{44}(r)] \cos \theta e^{i(kz + \omega t)} \quad (15)
 \end{aligned}$$

$$\frac{\partial s}{\partial r} = [C_1 N_{41}(r) + C_2 N_{42}(r) + C_3 N_{43}(r) + C_4 N_{44}(r)] \cos \theta e^{i(kz+\omega t)} \quad (16)$$

$$u - u_{if} = [C_1 M_{51}(r) + C_2 M_{52}(r) + C_3 M_{53}(r) + C_4 M_{54}(r) + A_3 M_{55}(r) + B_3 M_{56}(r) + A_1 M_{57}(r) + B_1 M_{58}(r) + A_{if} M_{59}(r)] \cos \theta e^{i(kz+\omega t)} \quad (17)$$

$$\sigma_{rr} + s + P_{of} = [C_1 M_{61}(r) + C_2 M_{62}(r) + C_3 M_{63}(r) + C_4 M_{64}(r) + A_3 M_{65}(r) + B_3 M_{66}(r) + A_1 M_{67}(r) + B_1 M_{68}(r) + A_{of} M_{6,10}(r)] \cos \theta e^{i(kz+\omega t)} \quad (18)$$

$$u - u_{of} = [C_1 M_{10,1}(r) + C_2 M_{10,2}(r) + C_3 M_{10,3}(r) + C_4 M_{10,4}(r) + A_3 M_{10,5}(r) + B_3 M_{10,6}(r) + A_1 M_{10,7}(r) + B_1 M_{10,8}(r) + A_{of} M_{10,10}(r)] \times \cos \theta e^{i(kz+\omega t)} \quad (19)$$

In Eqs. (12)–(19),  $M_{1,10}(r)$  represents an element appearing in the first row and tenth column.  $M_{10,10}(r)$  represents an element appearing in the tenth row and tenth column. The coefficients  $M_{ij}(r)$  and  $N_{ij}(r)$  are given in the Appendix [see Eq. (A.1)].

#### 4. FREQUENCY EQUATION

For perfect contact between the poroelastic cylindrical shell and the fluids, we assume that the normal stresses and radial displacements are continuous at  $r = r_1$  and  $r = r_2$ . Thus, the boundary conditions in case of a pervious surface are

$$\begin{aligned} \sigma_{rr} + s + P_{if} &= 0, \quad \sigma_{r\theta} = 0, \quad \sigma_{rz} = 0, \quad s = 0 \\ u - u_{if} &= 0, \quad \text{at } r = r_1 \\ \sigma_{rr} + s + P_{of} &= 0, \quad \sigma_{r\theta} = 0, \quad \sigma_{rz} = 0, \quad s = 0 \\ u - u_{of} &= 0, \quad \text{at } r = r_2 \end{aligned} \quad (20)$$

The boundary conditions in the case of an impervious surface are

$$\begin{aligned} \sigma_{rr} + s + P_{if} &= 0, \quad \sigma_{r\theta} = 0, \quad \sigma_{rz} = 0, \quad \frac{\partial s}{\partial r} = 0 \\ u - u_{if} &= 0, \quad \text{at } r = r_1 \\ \sigma_{rr} + s + P_{of} &= 0, \quad \sigma_{r\theta} = 0, \quad \sigma_{rz} = 0, \quad \frac{\partial s}{\partial r} = 0 \\ u - u_{of} &= 0, \quad \text{at } r = r_2 \end{aligned} \quad (21)$$

Substitution of Eqs. (12)–(15) and (17)–(19) into Eq. (20) results in a system of 10 homogeneous algebraic equations with 10 constants  $C_1, C_2, C_3, C_4, A_3, B_3, A_1, B_1, A_{if}$ , and  $A_{of}$ . For a nontrivial solution, the determinant of the coefficients must vanish. By eliminating these constants, the frequency equation of flexural vibrations of a poroelastic circular cylindrical shell immersed in a fluid in case of a pervious surface is

$$|A_{ij}| = 0, \quad i, j = 1 \dots 10 \quad (22)$$

In Eq. (22), the elements  $A_{ij}$  are

$$\begin{aligned} A_{ij} &= M_{ij}(r_1), \quad i = 1 \dots 5, \quad \text{and } j = 1 \dots 10 \\ A_{ij} &= M_{ij}(r_2), \quad i = 6 \dots 10, \quad \text{and } j = 1 \dots 10 \end{aligned} \quad (23)$$

where  $M_{ij}(r)$  are defined in the Appendix [see Eq. (A.1)].

Arguing along similar lines, Eqs. (12)–(14) and (16)–(19), together with the Eq. (21), yield the frequency equation of flexural vibrations of poroelastic circular cylindrical shell immersed in fluid, in case of an impervious surface, to be

$$|B_{ij}| = 0, \quad i, j = 1 \dots 10 \quad (24)$$

where the elements  $B_{ij}$  are

$$\begin{aligned} B_{ij} &= A_{ij}, \quad i = 1, 2, 3, 5, 6, 7, 8, 10 \quad \text{and } j = 1 \dots 10 \\ B_{4j} &= N_{4j}(r_1), \quad j = 1 \dots 10 \\ B_{9j} &= N_{4j}(r_2), \quad j = 1 \dots 10 \end{aligned} \quad (25)$$

where  $M_{ij}(r)$  and  $N_{ij}(r)$  are defined in Eq. (A.1) in the Appendix.

Setting the outer-fluid density to zero, i.e.,  $\rho_{of} \rightarrow 0$ , and then by eliminating the liquid effects from the frequency equation of a pervious surface (22), the results of a purely elastic solid are obtained as a special case considered by Kumar (1971). The frequency equation of an impervious surface (24) has no counterpart in a purely elastic solid.

#### 4.1 Frequency Equation for a Poroelastic Solid Cylinder

When the ratio of thickness to inner radius of the poroelastic cylindrical shell, i.e.,  $h/r_1 \rightarrow \infty$  as  $r_1 \rightarrow 0$ , it reduces to a poroelastic solid cylinder of radius  $h$ . Then, the frequency equation of a pervious surface (22) is reduced to

$$|P_{ij}| = 0, \quad i, j = 1 \dots 5 \quad (26)$$

where the elements  $P_{ij}$  are defined in the Appendix [see Eq. (A.3)].

Similarly, the frequency equation (24), when  $r_1 \rightarrow 0$  and with finite  $h$ , reduces to

$$|Q_{ij}| = 0, \quad i, j = 1 \dots 5 \quad (27)$$

where the elements  $Q_{ij}$  are defined in the Appendix [see Eq. (A.4)].

Equations (26) and (27) are the frequency equations of flexural vibrations propagating in a poroelastic solid cylinder of radius  $h$  immersed in fluid, for a pervious and an impervious surface, respectively.

### 4.2 Cutoff Frequencies

The frequencies obtained by equating the wave number to zero are referred to as the cutoff frequencies. Thus, for  $k = 0$ , the frequency equation of a pervious surface (22) reduces to the product of two determinants as

$$D_1 D_2 = 0 \quad (28)$$

where  $D_1$  and  $D_2$  are

$$D_1 = \begin{vmatrix} A_{11} & A_{12} & A_{13} & A_{14} & A_{15} & A_{16} & A_{19} & 0 \\ A_{21} & A_{22} & A_{23} & A_{24} & A_{25} & A_{26} & 0 & 0 \\ A_{41} & A_{42} & A_{43} & A_{44} & 0 & 0 & 0 & 0 \\ A_{51} & A_{52} & A_{53} & A_{54} & A_{55} & A_{56} & A_{59} & 0 \\ A_{61} & A_{62} & A_{63} & A_{64} & A_{65} & A_{66} & 0 & A_{6,10} \\ A_{71} & A_{72} & A_{73} & A_{74} & A_{75} & A_{76} & 0 & 0 \\ A_{91} & A_{92} & A_{93} & A_{94} & 0 & 0 & 0 & 0 \\ A_{10,1} & A_{10,2} & A_{10,3} & A_{10,4} & A_{10,5} & A_{10,6} & 0 & A_{10,10} \end{vmatrix}$$

$$D_2 = \begin{vmatrix} A_{37} & A_{38} \\ A_{87} & A_{88} \end{vmatrix} \quad (29)$$

The elements  $A_{ij}$  of  $D_1$  and  $D_2$  are defined in Eq. (23) are now evaluated for  $k = 0$ . From Eq. (28), it is clear that either  $D_1 = 0$  or  $D_2 = 0$  and these two equations give the cutoff frequencies of flexural vibrations of a poroelastic cylindrical shell immersed in an acoustic medium for a pervious surface. The equation

$$D_1 = 0 \quad (30)$$

depend on physical parameters of the poroelastic shell and the fluid, while the equation

$$D_2 = 0 \quad (31)$$

does not depend on fluid parameters. Hence, Eq. (30) give the cutoff frequencies of flexural vibrations of poroelastic cylindrical shells immersed in an acoustic medium for a pervious surface. Equation (31) is the frequency

equation of longitudinal shear vibrations, which gives the cutoff frequencies independent of the presence of fluid within and around the poroelastic cylindrical shell.

Similarly, the frequency equation of an impervious surface (24) when  $k = 0$  is reduced to the product of two determinants

$$D_3 D_4 = 0 \quad (32)$$

where  $D_3$  and  $D_4$  are

$$D_3 = \begin{vmatrix} B_{11} & B_{12} & B_{13} & B_{14} & B_{15} & B_{16} & B_{19} & 0 \\ B_{21} & B_{22} & B_{23} & B_{24} & B_{25} & B_{26} & 0 & 0 \\ B_{41} & B_{42} & B_{43} & B_{44} & 0 & 0 & 0 & 0 \\ B_{51} & B_{52} & B_{53} & B_{54} & B_{55} & B_{56} & B_{59} & 0 \\ B_{61} & B_{62} & B_{63} & B_{64} & B_{65} & B_{66} & 0 & B_{6,10} \\ B_{71} & B_{72} & B_{73} & B_{74} & B_{75} & B_{76} & 0 & 0 \\ B_{91} & B_{92} & B_{93} & B_{94} & 0 & 0 & 0 & 0 \\ B_{10,1} & B_{10,2} & B_{10,3} & B_{10,4} & B_{10,5} & B_{10,6} & 0 & B_{10,10} \end{vmatrix}$$

$$D_4 = \begin{vmatrix} B_{37} & B_{38} \\ B_{87} & B_{88} \end{vmatrix} \quad (33)$$

The elements  $B_{ij}$  of  $D_3$  and  $D_4$  are defined in Eq. (25) are now evaluated for  $k = 0$ . From Eq. (32), it is clear that either  $D_3 = 0$  or  $D_4 = 0$ . The equation

$$D_3 = 0 \quad (34)$$

gives the cutoff frequencies of flexural vibrations of a poroelastic cylindrical shell immersed in an acoustic medium in case of an impervious surface, while the equation

$$D_4 = 0 \quad (35)$$

yields the cutoff frequencies independent of the presence of fluid. Equations (31) and (35) are the same by virtue of Eq. (25). Hence, Eq. (35) is independent of nature of surface, i.e., pervious or impervious. Therefore, the cutoff frequencies given by Eq. (35) are independent of the presence of fluid within and around the poroelastic cylindrical shell and nature of surface. By using recurrence relations for Bessel functions (Abramowitz and Stegun, 1965), Eq. (35) is simplified to

$$J'_1(\alpha_3 r_1) Y'_1(\alpha_3 r_2) - J'_1(\alpha_3 r_2) Y'_1(\alpha_3 r_1) = 0 \quad (36)$$

where  $\alpha_3$  is defined in Eq. (6) for  $k = 0$ .

Equation (36) is the same for poroelastic cylindrical shells immersed in an acoustic medium and a poroelastic cylindrical shell in vacuum, as well as for pervious and impervious surfaces. By eliminating the liquid effects from Eq. (36), the results of a purely elastic solid discussed by Gazis (1959) are obtained. The frequency



equation (36) is discussed for limiting values of  $h/r_1$  when these values are too small and too large.

*For a thin poroelastic cylindrical shell:* When  $h/r_1 \ll 1$ , under the verifiable assumption of nonzero  $\alpha_3 h$ , it is seen that  $\alpha_3 r_1 \gg 1$  and  $\alpha_3 r_2 \gg 1$ . Using the well-known Hankel-Kirchhoff asymptotic approximations for Bessel functions (Abramowitz and Stegun, 1965),

$$J_1'(x) \approx \sqrt{\frac{2}{\pi x}} \left[ -\sin\left(x - \frac{3\pi}{4}\right) - \frac{7}{8x} \cos\left(x - \frac{3\pi}{4}\right) \right]$$

$$Y_1'(x) \approx \sqrt{\frac{2}{\pi x}} \left[ \cos\left(x - \frac{3\pi}{4}\right) - \frac{7}{8x} \sin\left(x - \frac{3\pi}{4}\right) \right]$$

the frequency equation of longitudinal shear vibrations (36) reduces to

$$\sin(\alpha_3 h) - \frac{7\alpha_3 h}{8\alpha_3^2 r_1 r_2} \cos(\alpha_3 h) \approx 0 \quad (37)$$

Equation (37) is the frequency equation of longitudinal shear vibrations of a thin poroelastic cylindrical shell. When  $\alpha_3 r_1 \rightarrow \infty$  and  $\alpha_3 r_2 \rightarrow \infty$ , Eq. (37) is reduced to

$$\sin(\alpha_3 h) \approx 0, \Rightarrow \alpha_3 h = \pi q, \quad q = 1, 2, 3, \dots$$

so that

$$\omega = \frac{q\pi V_3}{h}, \quad q = 1, 2, 3, \dots \quad (38)$$

which are the frequencies of a poroelastic plate of thickness  $h$ . Moreover, near the origin  $h/r_1 = 0$ , and assuming

$$\alpha_3 h = q\pi + \eta^*, \quad \eta^* \ll 1 \quad (39)$$

then using the frequency equation of longitudinal shear vibrations of a thin poroelastic cylindrical shell, Eq. (37) gives

$$\eta^* = \frac{7}{8q\pi} \left( \frac{h}{r_1} \right)^2, \quad q = 1, 2, 3, \dots \quad (40)$$

On substituting Eq. (40) into Eq. (39) and using Eq. (38), we can write

$$\omega = \frac{V_3 q \pi}{h} \left[ 1 + \frac{7}{8(q\pi)^2} \left( \frac{h}{r_1} \right)^2 \right], \quad q = 1, 2, 3, \dots \quad (41)$$

which are the frequencies of longitudinal shear vibrations of a poroelastic plate of thickness  $h$  near the origin.

*For a poroelastic solid cylinder:* When  $h/r_1 \rightarrow \infty$  as  $r_1 \rightarrow 0$ , the frequency Eq. (36) tends asymptotically to

$$J_1'(\alpha_3 h) = 0 \quad (42)$$

which is the frequency equation of longitudinal shear vibrations of a poroelastic solid cylinder of radius  $h$ . In Eq. (42), by ignoring the liquid effects, results of a purely elastic solid are obtained as a special case considered by Gazis (1959).

## 5. NONDIMENSIONALIZATION OF THE FREQUENCY EQUATION

For propagating modes in a nondissipative medium, the wave number  $k$  is real. The phase velocity  $C$  is the ratio of the frequency to the wave number, i.e.,  $C = \omega/k$ . To analyze the frequency Eqs. (22) and (24), it is convenient to introduce the following nondimensional variables:

$$\begin{aligned} a_1 &= PH^{-1}, & a_2 &= QH^{-1}, & a_3 &= RH^{-1} \\ a_4 &= NH^{-1}, & m_{11} &= \rho_{11}\rho^{-1}, & m_{12} &= \rho_{12}\rho^{-1} \\ m_{22} &= \rho_{22}\rho^{-1}, & \tilde{x} &= (V_0 V_1^{-1})^2, & \tilde{y} &= (V_0 V_2^{-1})^2 \\ \tilde{z} &= (V_0 V_3^{-1})^2, & \delta &= hL^{-1}, & t &= \rho_{if}\rho^{-1} \\ m &= V_{if}V_3^{-1}, & t_1 &= \rho_{of}\rho^{-1}, & m_1 &= V_{of}V_3^{-1} \\ \Omega &= \omega h C_0^{-1}, & \xi &= C V_{if}^{-1} \end{aligned} \quad (43)$$

where  $\Omega$  is the nondimensional frequency,  $\xi$  is the nondimensional phase velocity of poroelastic cylindrical shells immersed in an acoustic medium,  $H = P + 2Q + R$ ,  $\rho = \rho_{11} + 2\rho_{12} + \rho_{22}$ ,  $C_0$  and  $V_0$  are the reference velocities ( $C_0^2 = N/\rho$ ,  $V_0^2 = H/\rho$ ),  $C [= \omega/k]$  is the phase velocity,  $h$  is the thickness of the poroelastic cylindrical shell, and  $L$  is the wavelength. Let

$$g = \frac{r_2}{r_1}, \quad \text{so that} \quad \frac{h}{r_1} = (g - 1) \quad (44)$$

## 6. RESULTS AND DISCUSSION

Two types of poroelastic materials are considered to carry out the computational work, one is sandstone saturated with kerosene, say, material I (Fatt, 1959), the other one is sandstone saturated with water, say, material II (Yew and Jogi, 1976), whose nondimensional physical parameters are given in Table 1.

For a given poroelastic material, the frequency Eqs. (22) and (24), when nondimensionalized using Eqs. (43) and (44), constitute a relation between the nondimensional phase velocity  $\xi$  and the ratio of thickness to wavelength  $\delta (= h/L)$  for fixed values of  $g$ . Different values of  $g$ , e.g., 1.034, 1.286, 3, and infinity, are taken

**TABLE: 1** Nondimensional physical parameters of materials I and II

Material	Parameter									
	$a_1$	$a_2$	$a_3$	$a_4$	$m_{11}$	$m_{12}$	$m_{22}$	$x^{\sim}$	$y^{\sim}$	$z^{\sim}$
I	0.843	0.065	0.028	0.234	0.901	-0.001	0.101	0.999	4.763	3.851
II	0.960	0.006	0.028	0.412	0.877	0	0.123	0.913	4.347	2.129

for numerical computation. These values of  $g$  represent a thin poroelastic cylindrical shell, moderately thick poroelastic cylindrical shell, thick poroelastic cylindrical shell, and poroelastic solid cylinder, respectively. The values of  $\delta$  lie in  $[0, 1]$ . The nondimensional phase velocity  $\xi$  is determined for different values of  $\delta$  and for fixed values of  $g$ , each for a pervious and an impervious surface. For poroelastic cylindrical shells immersed in an acoustic medium, the values of  $m, m_1, t,$  and  $t_1$  are taken as  $m = m_1 = 1.5$  and  $t = t_1 = 0.4$ .

To compute the cutoff frequencies of flexural vibrations of poroelastic cylindrical shells immersed in an acoustic medium, Eqs. (30) and (34) are nondimensionalized using Eqs. (43) and (44). Equations (30) and (34) constitute the relation between the nondimensional frequency  $\Omega$  and the ratio of wall thickness to inner radius  $h/r_1$ . For a broad spectrum of values of  $h/r_1$ , the frequency  $\Omega$  is computed for the considered poroelastic materials, I and II. To compute the phase velocity and the cutoff frequency of flexural vibrations of poroelastic cylindrical shells immersed in an acoustic medium, the values of  $t, t_1, m,$  and  $m_1$  are taken as  $t = t_1 = 0.4$  and  $m = m_1$

$= 1.5$ . The computed phase velocity and frequency are presented in Figs. 1–5. Phase velocity as a function of wavelength is presented in Figs. 1–4 for poroelastic cylindrical shells immersed in an acoustic medium. The cutoff frequencies are presented in Fig. 5. The phase velocity and frequency are computed for pervious and impervious surfaces and both the considered materials. Figure 1 shows the phase velocity of a thin poroelastic cylindrical shell immersed in an acoustic medium. From Fig. 1, it is seen that the phase velocity is the same for pervious and impervious surfaces in  $0 \leq \delta < 0.3$  in case of material I. Beyond  $\delta = 0.3$ , in general, the phase velocity of an impervious surface is higher than that of a pervious surface. The phase velocity of pervious and impervious surfaces is the same for a thin poroelastic cylindrical shell immersed in an acoustic medium in case of material II. In general, the phase velocity in the case of material II is higher than that of material I for pervious and impervious surfaces. Therefore, it can be said that the presence of mass coupling parameter is reducing the phase velocity. Figure 2 shows the phase velocity of a moderately thick poroelastic cylindrical shell immersed in an acoustic medium for

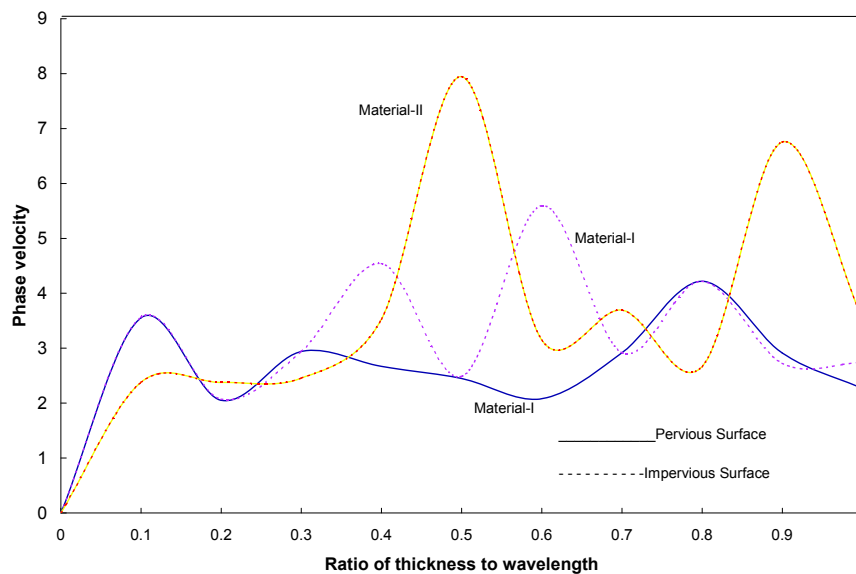


**FIG. 1:** Phase velocity as a function of wavelength (Mat-I, Mat-II, Thin Shell)

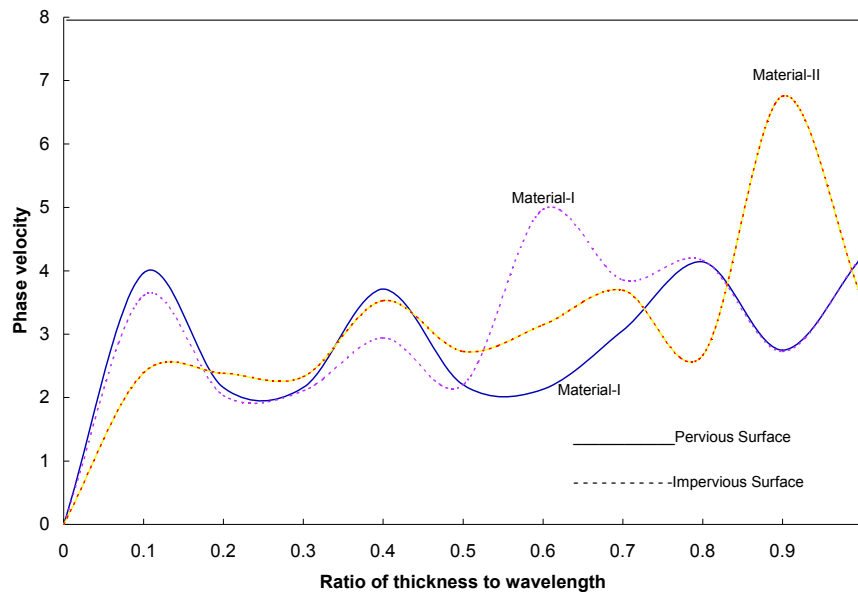


**FIG. 2:** Phase velocity as a function of wavelength (Mat-I, Mat-II, Moderately Thick Shell)

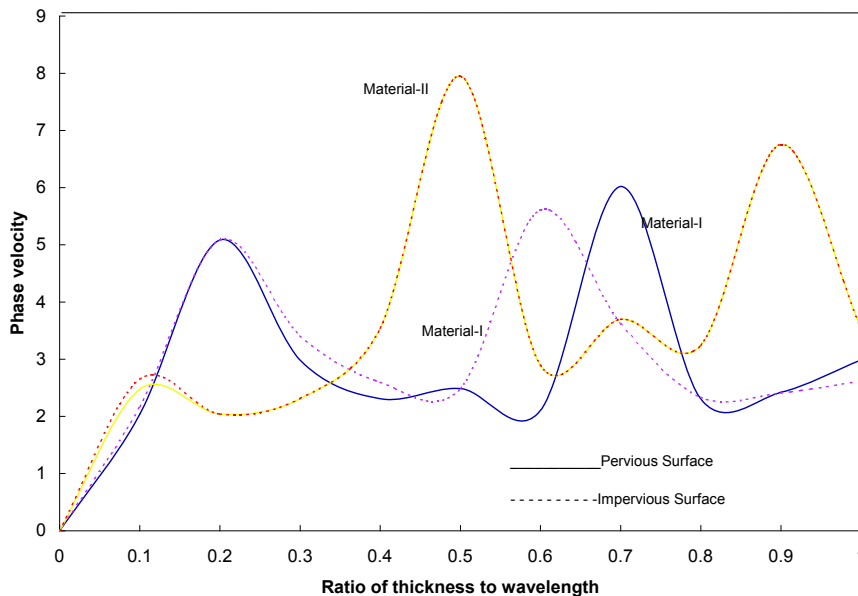


**FIG. 3:** Phase velocity as a function of wavelength (Mat-I, Mat-II, Thick Shell)

the considered materials. From Fig. 2, it is clear that the phase velocity of an impervious surface is higher than that of a pervious surface in  $0.5 \leq \delta < 0.8$ , otherwise it is same as that of a pervious surface. Here again, the phase velocity of a pervious and impervious surface is the same in case of material II. When the wavelength is

large, i.e.,  $0 \leq \delta < 0.2$ , the phase velocity for material II is less than that of material I; and for  $0.85 < \delta < 1$ , the phase velocity of material II is higher than that of material I, both for pervious and impervious surfaces. An increase of wall thickness has no significant effect on the phase velocity of a pervious surface, while it increases the phase

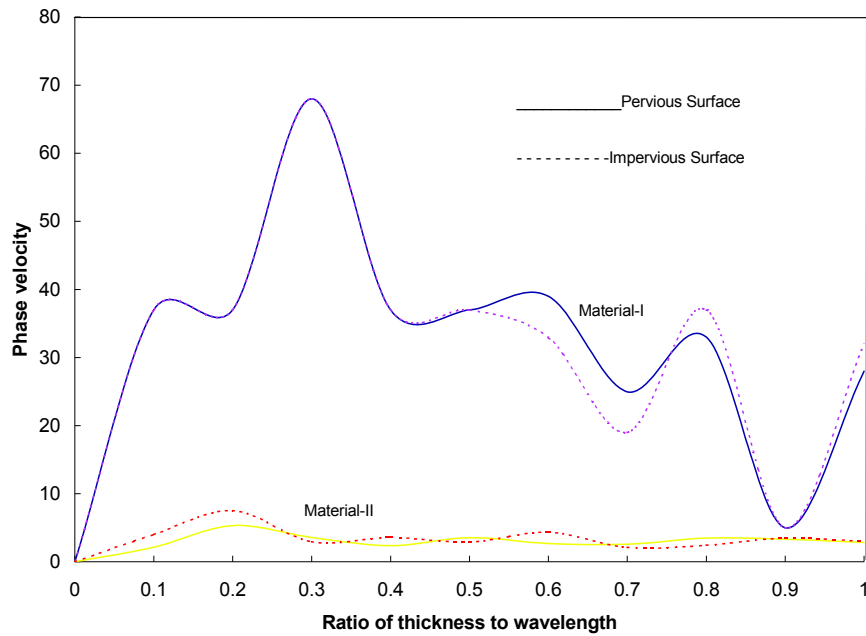


FIG. 4: Phase velocity as a function of wavelength (Mat-I, Mat-II, Solid Cylinder)

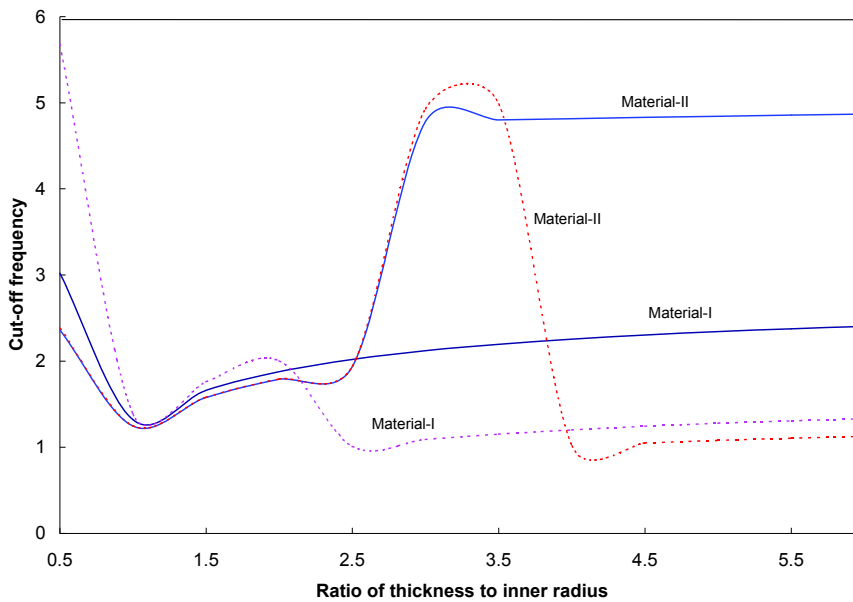


FIG. 5: Frequency as a function of ratio of thickness to inner radius (Mat-I, Mat-II)

velocity of an impervious surface for both the considered materials. The phase velocity of thick poroelastic cylindrical shells immersed in an acoustic medium is presented in Fig. 3 for both a pervious and an impervious surface and the considered materials. It is seen from Fig. 3 that

the phase velocity, in general, is the same for pervious and impervious surfaces for both the considered materials. The phase velocity for material II is higher than that of material I. Therefore, the presence of mass coupling parameter is reducing the phase velocity in case of a thick

poroelastic cylindrical shell. An increase of thickness has no significant effect on the phase velocity of pervious and impervious surfaces in case of the considered materials.

The phase velocity of a poroelastic solid cylinder for both a pervious and an impervious surface for the considered materials is presented in Fig. 4. The phase velocity of an impervious surface is less than that of a pervious surface in  $0.5 < \delta < 0.75$ ; otherwise, it is same as that of a pervious surface in case of material I. The phase velocity of pervious and impervious surfaces, in general, is the same in case of material II. The phase velocity of material I is higher than that of material II. Unlike a poroelastic cylindrical shell, in case of a poroelastic solid cylinder, the presence of mass coupling parameter is increasing the phase velocity of pervious and impervious surfaces. The phase velocity of a poroelastic solid cylinder in case of material I is higher than that of the phase velocity of poroelastic cylindrical shells. The phase velocity of a poroelastic solid cylinder in case of material II is almost the same as that of the phase velocity of poroelastic cylindrical shells. The frequency as a function of ratio of thickness to inner radius is presented in Fig. 5 for both the considered materials for both a pervious and an impervious surface. When the wall thickness is small, the frequency of an impervious surface is higher than that of a pervious surface in case of material I. For moderately thick poroelastic cylindrical shells, the frequency of a pervious and impervious surface is the same. For thick poroelastic cylindrical shells, the phase velocity of an impervious surface is lower than that of a pervious surface. With the increase of thickness, there is a small increase in the frequency. The variation of frequency in case of material II is similar to that of material I. Frequency in case of material II for a pervious surface is higher than that of the frequency in case of material I for thick poroelastic cylindrical shells. With the increase of wall thickness of a poroelastic cylindrical shell, there is no significant increase in the frequency in case of material II for a pervious surface.

## 7. CONCLUDING REMARKS

The study of flexural vibrations in poroelastic cylindrical shells immersed in an acoustic medium has led to following conclusions.

1. The frequency equation of longitudinal shear vibrations is independent of nature of surface and the presence of fluid within and around the poroelastic cylindrical shell.
2. In general, the phase velocity of an impervious surface is higher than that of a pervious surface in case of material I.
3. The phase velocity of a pervious and an impervious surface is the same in case of material II.
4. There is no significant effect on the phase velocity of a pervious surface with the increase of thickness for the considered materials.
5. The phase velocity of a poroelastic solid cylinder in case of material I is higher than that of material II for both a pervious and an impervious surface.
6. The frequency of an impervious surface is lower than that of a pervious surface for the considered materials.

## ACKNOWLEDGMENTS

The authors are thankful to Editor-in-Chief Prof. Kambiz Vafai and to the reviewers for suggestions on improving the quality of this paper.

## REFERENCES

- Abramowitz, A. and Stegun, I. A., *Handbook of Mathematical Functions*, National Bureau of Standards, Washington, 1965.
- Ahmed Shah, S., Axially symmetric vibrations of fluid-filled poroelastic circular cylindrical shells, *J. Sound Vib.*, vol. 318, pp. 389–405, 2008.
- Biot, M. A., Theory of propagation of elastic waves in fluid-saturated porous solid, *J. Acoust. Soc. Am.*, vol. 28, pp. 168–178, 1956.
- Chao, G., Smeulders, D. M. J., and van Dongen, M. E. H., Shock-induced borehole waves in porous formations: Theory and experiments, *J. Acoust. Soc. Am.*, vol. 116, pp. 693–702, 2004.
- Farhang, H., Esmail, E., Anthony, N. S., and Mirnezami, A., Wave propagation in transversely isotropic cylinders, *Int. J. Solids Struct.*, vol. 44, pp. 5236–5246, 2007.
- Fatt, I., The Biot-Willis elastic coefficients for a sandstone, *J. Appl. Mech.*, vol. 26, pp. 296–297, 1959.
- Gazis, D. C., Three-dimensional investigation of the propagation of waves in hollow circular cylinders. I., Analytical foundation, *J. Acoust. Soc. Am.*, vol. 31, pp. 568–573, 1959.
- Kanj, M., Abousleiman, Y., and Ghanem, R., Anisotropic poromechanics solutions for the hollow-cylinders, *J. Eng. Mech.*, vol. 129, pp. 1277–1287, 2003.

- Malla Reddy, P. and Tajuddin, M., Exact analysis of the plane-strain vibrations of thick-walled hollow poroelastic cylinders, *Int. J. Solids Struct.*, vol. 37, pp. 3439–3456, 2000.
- Kumar, R., Flexural vibrations of fluid-filled circular cylindrical shells, *Acustica*, vol. 24, pp. 137–146, 1971.
- Tajuddin, M. and Sarma, K. S., Torsional vibrations of poroelastic cylinders, *Trans. ASME J. Appl. Mech.*, vol. 47, pp. 214–216, 1980.
- Tajuddin, M. and Ahmed Shah, S., Circumferential waves of infinite hollow poroelastic cylinders, *Trans. ASME, J. Appl. Mech.*, vol. 73, pp. 705–708, 2006.
- Tajuddin, M. and Ahmed Shah, S., On torsional vibrations of infinite hollow poroelastic cylinders, *J. Mech. Mater. Struct.*, vol. 2, pp. 189–200, 2007.
- Wisse, C. J., Smeulders, D. M. J., van Dongen, M. E. H., and Chao, G., Guided wave modes in porous cylinders: Experimental results, *J. Acoust. Soc. Am.*, vol. 112, pp. 890–895, 2002.
- Yew, C. H. and Jogi, P. N., Study of wave motions in fluid-saturated porous rocks, *J. Acoust. Soc. Am.*, vol. 60, pp. 2–8, 1976.

## APPENDIX

Coefficients  $M_{ij}(r)$  and  $N_{ij}(r)$  appearing in Eqs. (12)–(19) are

$$M_{11}(r) = \{[(Q+R)\delta_1^2 - (A+Q)]k^2 + [(Q+R)\delta_1^2 - (P+Q)]\alpha_1^2\} J_1(\alpha_1 r) + \frac{2N\alpha_1}{r} J_2(\alpha_1 r)$$

$$M_{15}(r) = \frac{-2N\alpha_3}{r} J_2(\alpha_3 r)$$

$$M_{17}(r) = 2Nik\alpha_3 J_1(\alpha_3 r) - \frac{4Nik}{r} J_2(\alpha_3 r)$$

$$M_{19}(r) = \omega^2 \rho_{if} J_1(\alpha_{if} r), \quad M_{1,10}(r) = 0$$

$$M_{21}(r) = \frac{2N\alpha_1}{r} J_2(\alpha_1 r)$$

$$M_{25}(r) = N\alpha_3^2 J_1(\alpha_3 r) - \frac{2N\alpha_3}{r} J_2(\alpha_3 r)$$

$$M_{27}(r) = Nik\alpha_3 J_1(\alpha_3 r) - \frac{4Nik}{r} J_2(\alpha_3 r)$$

$$M_{29}(r) = 0, \quad M_{2,10}(r) = 0$$

$$M_{31}(r) = \frac{2Nik}{r} J_1(\alpha_1 r) - 2Nik\alpha_1 J_2(\alpha_1 r)$$

$$M_{35}(r) = \frac{Nik}{r} J_1(\alpha_3 r)$$

$$M_{37}(r) = \frac{-N\alpha_3}{r} J_1(\alpha_3 r) + N(\alpha_3^2 - k^2) J_2(\alpha_3 r)$$

$$M_{39}(r) = 0, \quad M_{3,10}(r) = 0 \quad (\text{A.1})$$

$$M_{41}(r) = (R\delta_1^2 - Q)(k^2 + \alpha_1^2) J_1(\alpha_1 r), \quad M_{45}(r) = 0$$

$$M_{46}(r) = 0, \quad M_{47}(r) = 0, \quad M_{48}(r) = 0, \quad M_{49}(r) = 0$$

$$M_{4,10}(r) = 0, \quad M_{51}(r) = \frac{1}{r} J_1(\alpha_1 r) - \alpha_1 J_2(\alpha_1 r)$$

$$M_{55}(r) = \frac{1}{r} J_1(\alpha_3 r), \quad M_{57}(r) = 2ik J_2(\alpha_3 r)$$

$$M_{59}(r) = \frac{-1}{r} J_1(\alpha_{if} r) + \alpha_{if} J_2(\alpha_{if} r), \quad M_{5,10}(r) = 0$$

$$M_{6j}(r) = M_{1j}(r), \quad j = 1 \dots 8, \quad M_{69}(r) = 0$$

$$M_{6,10}(r) = \omega^2 \rho_{of} H_1^{(1)}(\alpha_{of} r), \quad M_{7j}(r) = M_{2j}(r)$$

$$j = 1 \dots 8, \quad M_{79}(r) = 0, \quad M_{7,10}(r) = 0$$

$$M_{8j}(r) = M_{3j}(r), \quad j = 1 \dots 8, \quad M_{89}(r) = 0$$

$$M_{8,10}(r) = 0, \quad M_{9j}(r) = M_{4j}(r), \quad j = 1 \dots 8$$

$$M_{99}(r) = 0, \quad M_{9,10}(r) = 0, \quad M_{10,j}(r) = M_{5j}(r)$$

$$j = 1 \dots 8, \quad M_{10,9}(r) = 0$$

$$M_{10,10}(r) = -\frac{1}{r} H_1^{(1)}(\alpha_{of} r) + \alpha_{of} H_2^{(1)}(\alpha_{of} r)$$

$$N_{41}(r) = \frac{(R\delta_1^2 - Q)(k^2 + \alpha_1^2)}{r} J_1(\alpha_1 r)$$

$$- \alpha_1 (R\delta_1^2 - Q)(k^2 + \alpha_1^2) J_2(\alpha_1 r),$$

$$N_{45}(r) = 0, \quad N_{46}(r) = 0, \quad N_{47}(r) = 0$$

$$N_{48}(r) = 0, \quad N_{49}(r) = 0, \quad N_{4,10}(r) = 0$$

$M_{12}(r), M_{16}(r), M_{18}(r), M_{22}(r), M_{26}(r), M_{28}(r), M_{32}(r), M_{36}(r), M_{38}(r), M_{42}(r), M_{52}(r), M_{56}(r), M_{58}(r), M_{62}(r), M_{66}(r), M_{68}(r), N_{42}(r)$  are similar expressions as  $M_{11}(r), M_{15}(r), M_{17}(r), M_{21}(r), M_{25}(r), M_{27}(r), M_{31}(r), M_{35}(r), M_{37}(r), M_{41}(r), M_{51}(r), M_{55}(r), M_{57}(r), M_{61}(r), M_{65}(r), M_{67}(r), N_{41}(r)$  with  $J_1, J_2$  replaced by  $Y_1$  and  $Y_2$ , respectively.

$M_{13}(r), M_{23}(r), M_{33}(r), M_{43}(r), M_{53}(r), M_{63}(r), N_{43}(r)$  are similar expressions as  $M_{11}(r), M_{21}(r), M_{31}(r), M_{41}(r), M_{51}(r), M_{61}(r), N_{41}(r)$  with  $\alpha_1, \delta_1$  replaced by  $\alpha_2, \delta_2$  respectively,  $M_{14}(r), M_{24}(r), M_{34}(r), M_{44}(r), M_{54}(r), M_{64}(r), N_{44}(r)$  are similar expressions as  $M_{11}(r), M_{21}(r), M_{31}(r), M_{41}(r), M_{51}(r), M_{61}(r), N_{41}(r)$  with  $\alpha_1, \delta_1, J_1,$  and  $J_2$  replaced by  $\alpha_2, \delta_2, Y_1,$  and  $Y_2$ , respectively.

In Eq. (A.1),  $P = A + 2N$  and

$$\begin{aligned} \delta_i^2 &= \frac{1}{(RK_{12} - QK_{22})} [(RK_{11} - QK_{12}) \\ &- V_i^{-2}(PR - Q^2)], \quad (i = 1, 2) \\ K_{11} &= \rho_{11} - \frac{ib}{\omega}, \quad K_{12} = \rho_{12} + \frac{ib}{\omega} \\ K_{22} &= \rho_{22} - \frac{ib}{\omega} \end{aligned} \quad (\text{A.2})$$

The elements  $P_{ij}$  appearing in Eq. (26) are defined as

$$\begin{aligned} P_{11}(h) &= \{[(Q+R)\delta_1^2 - (A+Q)]k^2 + [(Q+R)\delta_1^2 \\ &- (P+Q)]\alpha_1^2\} J_1(\alpha_1 h) + \frac{2N\alpha_1}{h} J_2(\alpha_1 h) \\ P_{12}(h) &= \{[(Q+R)\delta_2^2 - (A+Q)]k^2 + [(Q+R)\delta_2^2 \\ &- (P+Q)]\alpha_2^2\} J_1(\alpha_2 h) + \frac{2N\alpha_2}{h} J_2(\alpha_2 h) \\ P_{13}(h) &= \frac{-2N\alpha_3}{h} J_2(\alpha_3 h) \\ P_{14}(h) &= 2Nik\alpha_3 J_1(\alpha_3 h) - \frac{4Nik}{h} J_2(\alpha_3 h) \\ P_{15}(h) &= \omega^2 \rho_{of} H_1^{(1)}(\alpha_{of} h), \quad P_{21}(h) = \frac{2N\alpha_1}{h} J_2(\alpha_1 h) \\ P_{22}(h) &= \frac{2N\alpha_2}{h} J_2(\alpha_2 h) \\ P_{23}(h) &= N\alpha_3^2 J_1(\alpha_3 h) - \frac{2N\alpha_3}{h} J_2(\alpha_3 h) \\ P_{24}(h) &= Nik\alpha_3 J_1(\alpha_3 h) - \frac{4Nik}{h} J_2(\alpha_3 h), \quad P_{25}(h) = 0 \\ P_{31}(h) &= \frac{2Nik}{h} J_1(\alpha_1 h) - 2Nik\alpha_1 J_2(\alpha_1 h) \\ P_{32}(h) &= \frac{2Nik}{h} J_1(\alpha_2 h) - 2Nik\alpha_2 J_2(\alpha_2 h) \end{aligned}$$

$$\begin{aligned} P_{33}(h) &= \frac{Nik}{h} J_1(\alpha_3 h) \\ P_{34}(h) &= \frac{-N\alpha_3}{h} J_1(\alpha_3 h) + N(\alpha_3^2 - k^2) J_2(\alpha_3 h) \\ P_{35}(h) &= 0, \quad P_{41}(h) = (R\delta_1^2 - Q)(k^2 + \alpha_1^2) J_1(\alpha_1 h) \\ P_{42}(h) &= (R\delta_2^2 - Q)(k^2 + \alpha_2^2) J_1(\alpha_2 h) \\ P_{43}(h) &= 0, \quad P_{44}(h) = 0, \quad P_{45}(h) = 0 \\ P_{51}(h) &= \frac{1}{h} J_1(\alpha_1 h) - \alpha_1 J_2(\alpha_1 h) \\ P_{52}(h) &= \frac{1}{h} J_1(\alpha_2 h) - \alpha_2 J_2(\alpha_2 h) \\ P_{53}(h) &= \frac{1}{h} J_1(\alpha_3 h), \quad P_{54}(h) = 2ik J_2(\alpha_3 h) \\ P_{55}(h) &= -\frac{1}{h} H_1^{(1)}(\alpha_{of} h) + \alpha_{of} H_2^{(1)}(\alpha_{of} h) \end{aligned} \quad (\text{A.3})$$

In Eq. (A.3),  $J_1, J_2$  are Bessel functions of the first kind of order one and two;  $H_1^{(1)}$  and  $H_2^{(1)}$  are Hankel functions of the first kind of order one and two, respectively.

The elements  $Q_{ij}$  appearing in Eq. (27) are defined as

$$\begin{aligned} Q_{ij} &= P_{ij}; \quad i = 1, 2, 3, 5, \quad j = 1 \dots 5, \quad \text{and} \\ Q_{41}(h) &= \frac{(R\delta_1^2 - Q)(k^2 + \alpha_1^2)}{h} J_1(\alpha_1 h) \\ &- \alpha_1 (R\delta_1^2 - Q)(k^2 + \alpha_1^2) J_2(\alpha_1 h) \\ Q_{42}(h) &= \frac{(R\delta_2^2 - Q)(k^2 + \alpha_2^2)}{h} J_1(\alpha_2 h) \\ &- \alpha_2 (R\delta_2^2 - Q)(k^2 + \alpha_2^2) J_2(\alpha_2 h) \\ Q_{43}(h) &= 0, \quad Q_{44}(h) = 0, \quad Q_{45}(h) = 0 \end{aligned} \quad (\text{A.4})$$

# RECONCILIATION OF PACKED COLUMN PERMEABILITY DATA—PART 1. THE TEACHING OF GIDDINGS REVISITED

*Hubert M. Quinn*

*Chief Technical Officer, The Wrangler Group LLC*

Address all correspondence to H. M. Quinn E-mail: Hubert@wranglergroup.com

*Original Manuscript Submitted: 10/16/2008; Final Draft Received: 8/14/2009*

*In his classic text, Giddings (1965) put in writing a “Rosetta Stone” for packed column permeability research, which has gained little recognition since then. This lack of recognition is due partly to the complex nature of the subject matter and partly to the context, which was purely chromatographic. In it, he established experimentally that the value of his parameter  $\phi'$  pertaining to packed chromatographic columns was 300 for well-packed columns containing narrow distributions of spherical nonporous glass beads. Unfortunately, however, even though engineers and chromatographers spend much of their energy dealing with the same subject matter—the flow of liquids through conduits and packed beds—neither of these scientific disciplines recognized the relative importance of this contribution to the understanding of the pressure-flow relationship in general, and packed beds in particular. In this paper, we explore Giddings’ unique concept of mean fluid velocity through a cross section. As a result, when taken in conjunction with his measured values for  $\phi'$ , the inescapable conclusion is that the true value of the permeability coefficient in the Kozeny-Blake equation is not Carman’s celebrated value of 180, but rather the much greater value of 267. Moreover, we also demonstrate that although Giddings applied his conclusion concerning its value (which he expressed in 1991) to all particle types, his bona fides was rooted in his measurements on the nonporous smooth spherical glass beads reported in his 1965 textbook. Finally, in an elaboration of Giddings’ Table 5.3-1, we show that all his experimental results, both for columns packed with porous particles and for columns packed with nonporous particles, support this value.*

**KEY WORDS:** *darcy, permeability, fluid velocity, interstitial fraction, bed porosity, kozeny constant*

## 1. INTRODUCTION

Darcy’s law of 1856 is a basic statement of the relationship, at low flow velocities, between the pressure gradient and the fluid flow through columns packed with granular materials. In particular, it establishes that the relationship is linear between pressure gradient and fluid flux. Accordingly, on a plot of measured pressure differential against measured fluid flux, all data points fall on a straight line. However, Darcy’s law gives no hint as to how one could independently determine the slope of the line. A great deal of effort has been put forth over the

past many decades to gain an understanding of what other variables affect the slope of the line and in what particular arrangement said variables should be incorporated into a definitive expression (Dullien, 1992; Churchill, 1988; Whitaker, 1986; Sanchez-Palencia, 1980; Moura Neto and Melo, 2001; Moura Neto et al., 1998). Not least among the subjects of this investigation is the value of the so-called constant of proportionality (Scheidegger, 1957). In addition, some investigators have focused on the so-called wall effect, because of the inability of rigid particles to “nest” against a column wall, on the one hand, and the effect of fluid friction against the wall, on the other.



### NOMENCLATURE

$A_i$	column cross section available for solute/fluid diffusion [cm <sup>2</sup> ]	$r_c$	radius of capillary [cm]
$A_0$	column cross section available for fluid convective flow [cm <sup>2</sup> ]	$t_0$	time for elution of unretained solute [s]
$A_t$	column cross section available for fluid migration [cm <sup>2</sup> ]	<b>Greek Symbols</b>	
$d_c$	diameter of capillary [cm]	$\varepsilon$	Giddings' column external porosity in his 1991 text
$\Delta P$	pressure drop along column (calculated) [gcm <sup>-1</sup> s <sup>-2</sup> ]	$\varepsilon_0$	current authors' external column porosity
$d_p$	spherical particle diameter equivalent [cm]	$\varepsilon_i$	current authors' internal column porosity
$dp/dz$	column pressure differential [gcm <sup>-1</sup> s <sup>-2</sup> ]	$\varepsilon_t$	current authors' total column porosity
$K$	permeability coefficient in Darcy's equation	$\Phi$	ratio of column external porosity to column total porosity
$K_0$	Giddings' Specific permeability coefficient in Darcy's equation	$\phi$	flow resistance parameter
$K_c$	Giddings' nonspecific velocity correlation coefficient	$\phi'$	Giddings' modified flow resistance parameter
$L$	column length [cm]	$\eta$	fluid absolute viscosity [gcm <sup>-1</sup> s <sup>-1</sup> ]
$P_0$	empirical constant	$\mu_c$	mean fluid velocity in a capillary [cms <sup>-1</sup> ]
$Q$	volumetric fluid flow rate [cm <sup>3</sup> min <sup>-1</sup> ]	$\mu_i$	average fluid interstitial linear velocity [cms <sup>-1</sup> ]
$q$	fluid flux in Darcy's equation [cms <sup>-1</sup> ]	$\mu_s$	average fluid superficial linear velocity [cms <sup>-1</sup> ]
		$\mu_t$	average mobile phase velocity [cms <sup>-1</sup> ]
		$\nu$	Giddings' mean fluid velocity through a cross-section [cms <sup>-1</sup> ]
		$\langle \nu \rangle$	Giddings' interstitial fluid velocity [cms <sup>-1</sup> ]

(Coulson, 1935; Dugeon, 1966; Finnemore and Franzini, 2002; Giloaguen et al., 2001; Gupte, 1970; Happel and Brenner, 1965).

## 2. THE TEACHING OF GIDDINGS

In his first textbook, Giddings (1965) develops his own equation for the relationship between pressure gradient and fluid flow in a packed column. Making reference to the mathematical difficulties associated with the Navier-Stokes equation, he begins the development of his equation where everyone else begins—with Darcy's law and permeability (p 205),

$$q = -K \frac{dp}{dz} \quad (1)$$

where

$q$  = fluid flux (fluid flow per unit cross section)

$dp/dz$  = column differential pressure gradient

$K$  = constant of proportionality

The negative sign in Eq. (1) indicates that fluid flux  $q$  and pressure gradient act in opposite directions. That is

to say, fluid moves from a location of high pressure to a location of low pressure along the longitudinal axes of a packed column. The differential form of Darcy's equation  $dp/dz$  is used because it also applies to gas chromatography, in which case the fluid is compressible and the pressure gradient changes along the length of the column. The quantity  $dp$  represents the infinitesimal change in column pressure for the corresponding infinitesimal change in longitudinal column length  $dz$ . In the case of liquid chromatography, however, when the fluid is a liquid and consequently noncompressible (to a first approximation), one may re-express Eq. (1) as

$$q = \frac{K \Delta P}{L} \quad (2)$$

Giddings further modifies the constant of proportionality  $K$  so that it is the more "specific" term  $K_0$  by incorporating the fluid viscosity as an equation variable. Thus, he writes

$$q = \frac{K_0 \Delta P}{L \eta} \quad (3)$$

where  $K_0$  = specific permeability coefficient

## 2.1 Mean Fluid Velocity

Giddings' concept of fluid velocity is rooted in his definition of column porosity introduced on page 198 of his 1965 textbook as "Porosity, by definition, is the fraction of a total volume element occupied by all free space." In the case of a packed column, this definition of porosity corresponds to *total* column porosity  $\varepsilon_t$  not column external porosity  $\varepsilon_0$ . Moreover, in a clarification found in his footnote relating to the definition, Giddings suggests that because one cannot distinguish between the free space *between* the particles and that contained *within* the particles, one cannot measure *chromatographically* the separate subsections of porosity in a chromatographic column filled with porous particles. Giddings therefore excluded the technique that has become known as inverse size exclusion chromatography (ISEC). This is because he did not accept that the technique provides an acceptable differentiation between the fractional free space *inside* and the fractional free space *outside* the particle fraction within columns packed with porous particles. ISEC is based on the use of a homologous series of unretained solutes, some of which fully penetrate the pore network of porous particles, some of which are partially excluded, and some of which are fully excluded from the pore network by virtue of their size in solution. Since unretained solutes typically used by chromatographers fully permeate the pore network, and these are the solutes used to measure fluid velocity, this technique when combined with measured flow rate and empty column volume results in a measure of column *total* porosity, not column *external* porosity. Giddings is teaching, therefore, that one cannot measure *chromatographically* the external porosity of a column packed with porous particles to any acceptable degree of accuracy. Accordingly, in defining the meaning of his fluid velocity term  $v$  as "mean fluid velocity through a cross-section," Giddings took a much different view from that embodied in the accepted definition of the  $q$  term in Darcy's equation. In its broadest interpretation, Giddings' definition includes both types of fluid transport found to coexist within a packed granular column, namely, convective fluid transport *between* the particles and fluid transport by diffusion *within* the "blind" pores of the particles. Blind pores are pores within the particle that have only one fluid opening, i.e., they are not through pores. Accordingly, Giddings realized that the measured velocity of an unretained solute, which is what a chromatographer measures, is the same as the mobile phase velocity (Guiochon et al., 1994), and is equivalent to the mean fluid velocity through a cross section of

any packed column regardless of whether the particles are porous or nonporous. Therefore, one may write Giddings' mean fluid velocity through a cross section thusly

$$v = \mu_t \quad (4)$$

where  $v$  = Giddings mean fluid velocity through a cross section.

He also recognized that the cross section of a packed column that the unretained solute experiences varies depending on whether the particles in the column are porous or nonporous. Consequently, the use of mobile phase velocity is not straightforward *from a permeability point of view* because it does not differentiate between convective and diffusive mass transfer. This is a problem with columns packed with porous particles because fluid motion due to diffusion does not contribute to friction and must be ignored in considerations of column permeability.

Thus, on the one hand, when the particles are porous, an unretained solute dissolved in the fluid that percolates through the interstices of the particles, experiences a column cross section that corresponds to that fraction of the empty column cross section available for fluid "migration" by either of the two mechanisms of mass transfer mentioned. This cross section has a component both internal and external to the particle fraction. Additionally, an unretained solute will experience this cross section even though fluid equilibrium exists inside and outside the particles because intraparticle diffusion is driven by solute concentration, not fluid composition. This is an important consideration because it is customary to take permeability measurements under conditions of fluid equilibrium in order to take advantage of a constant fluid viscosity value. This column cross section is represented by the product of the total column porosity and the empty column cross section. Accordingly, the column cross section available for fluid migration is:

$$A_t = \varepsilon_t A \quad (5)$$

where

$A_t$  = cross section available for fluid migration in columns packed with porous particles

$A$  = cross section of the corresponding empty column

On the other hand, when the particles are nonporous, the only mass transfer mechanism present is that due to the "flow" of fluid between the particles. Accordingly,

in recognition of the common meaning usually attached to the term flow, which has the connotation of convective transport, that fraction of the empty column cross section available for fluid flow is the appropriate cross section applicable to Giddings' definition of mean fluid velocity, when the unretained solute velocity does *not* contain any component due to diffusion. This cross section has only a component external to the particle fraction and is represented by the product of the external column porosity and the empty column cross section,

$$A_0 = \varepsilon_0 A \quad (6)$$

where  $A_0$  = cross section available for fluid convective flow.

In columns packed with porous particles, the difference between the column cross section available for fluid migration and fluid convective flow is the cross section available for solute-fluid diffusion. One can therefore write

$$A_i = A_t - A_0 = (\varepsilon_t - \varepsilon_0)A = \varepsilon_i A \quad (7)$$

where  $A_i$  = cross section available for unretained solute diffusion in a column packed with porous particles.

Because Giddings' definition of mean fluid velocity depends on the specific set of circumstances under which the unretained solute finds itself, i.e., either in a column packed with porous particles or in a column packed with nonporous particles, his teaching may be stated as twofold:

1. Columns packed with porous particles,

$$v = \frac{Q}{A_t} = \frac{Q}{A\varepsilon_t} = \mu_t = \frac{L}{t_0} \quad (8)$$

2. Columns packed with nonporous particles,

$$v = \frac{Q}{A_0} = \frac{Q}{A\varepsilon_0} = \mu_t = \mu_i = \frac{L}{t_0} \quad (9)$$

Chromatography is a *thermodynamically* driven process, whereas ordinary flow through porous media is a *hydrodynamically* driven process. This distinction results in the use of different velocity frames, some of which overlap and some of which do not. Engineers often measure volumetric fluid flow rate and calculate bulk velocity (also known as superficial velocity) from the column cross-sectional area. Chromatographers typically inject tracers into packed columns to measure the rate of change in longitudinal distance using the elution time of the tracer.

For columns packed with nonporous particles, both these methodologies produce the same result for fluid velocity, whether chromatographers express it as mobile phase velocity or interstitial velocity. This is because there are no pores within the particles to influence the elution time of an injected solute. Thus, the time it takes for an unretained solute to traverse the length of the column is a function of the total porosity of the column  $\varepsilon_t$ , which in this case (i.e., nonporous particles) happens to be the same as the external porosity  $\varepsilon_0$  of the column.

For columns packed with porous particles, on the other hand, these methodologies do *not* produce the same result for fluid velocity because the chromatographers' experimental technique of determining  $t_0$  is influenced by solute diffusion in the pores of the particles. Giddings recognized that chromatographers are focused on *total* column porosity rather than *external* column porosity because the former is a more useful *thermodynamic* property to know than the latter. On the other hand, he realized that in columns packed with porous particles, the mobile phase velocity is not *directly* related to pressure drop. Accordingly, he developed a framework by which chromatographers can use their porous particles in combination with measured mobile phase velocity to, in a sense, "back-calculate" for the external porosity of the column, which is a necessary *independent variable* in the pressure-flow relationship in a granular bed. To do this, however, he needed a compensation factor to (i) *discount* the contribution of molecular diffusion in measurements of mobile phase velocity and (ii) establish a methodology by which chromatographers' measurements of total column porosity  $\varepsilon_t$  could be used in permeability determinations, all in columns packed with porous particles.

## 2.2 Giddings use of the Term $\Phi$

In order to enable chromatographers to use their mobile phase velocity measurements for columns packed with porous particles in determinations of column permeability, Giddings combines the use of total column porosity  $\varepsilon_t$  with a new term  $\Phi$  borrowed from thermodynamic theory, which he says stands for the ratio of the free space fraction between the particles to the total free space fraction in the column, i.e., the ratio of a fraction to a fraction. Thus,

$$\Phi = \frac{\varepsilon_0}{\varepsilon_t} \quad (10)$$

By combining the term  $\Phi$  with measured values for the mobile phase velocity, Giddings avoids the necessity of

having to measure the external column porosity in a column packed with porous particles. We can show this as follows:

$$\frac{\mu_t}{\Phi} = \frac{\mu_t \varepsilon_t}{\varepsilon_0} = \mu_i = \frac{\mu_s}{\varepsilon_0} \quad (11)$$

Accordingly, since Giddings used only “well-packed” columns in his experiments and since he had established using nonporous particles in which there is no uncertainty in the measurement of column external porosity, that well-packed columns have an external porosity of approximately 0.4, Giddings’ methodology relies on an *inferred value* for  $\varepsilon_0$ . This is a necessary step in the process of getting from a measured mobile phase velocity to a “measured” superficial velocity in columns packed with porous particles. This process relies, of course, on the fact that Giddings was (i) relying on his in-house column packing expertise to produce consistently well-packed columns with both porous and nonporous particles and (ii) comparing his measured pressure drop and total column porosity values for columns packed with porous and nonporous particles and “back-calculating” for the value of his  $\Phi$  parameter.

Giddings goes on to say that for porous particles used in gas-liquid chromatography, the value of total column porosity is about 0.8, i.e.,  $\varepsilon_t = 0.8$ . He further points out that since the external porosity of a well-packed chromatographic column has a  $\varepsilon_0 \sim 0.4$ , this means that for gas chromatographic support particles, the value of  $\Phi \sim 0.5$ , i.e.  $(0.4)/(0.8)$ .

Since in liquid chromatographic columns filled with nonporous particles, the external porosity is the same as the total porosity, i.e.,  $\varepsilon_0 = \varepsilon_t$  and then  $\Phi = 1$ . Thus, if the measured value for  $\varepsilon_t$  is 0.4 in a well-packed column, then  $\varepsilon_0$  is also 0.4. Additionally, if in a well-packed liquid chromatographic column filled with porous particles the measured value for  $\varepsilon_t$  is 0.6 and by comparison to the value for a well-packed column when the particles are nonporous  $\varepsilon_0 = 0.4$ , then  $\Phi = .4/.6 = .667$ . This means that the total porosity is distributed 2/3 in the interparticle space and 1/3 in the intraparticle space.

### 2.3 The Particle Size Term

There is no provision in Darcy’s law per se to incorporate the concept of particle size. Therefore, one has to adopt some hypothetical framework to accommodate this term. This is done by Giddings via the adaptation of a model based on flow through a capillary. Accordingly, he starts with Poiseuille’s equation for flow in a capillary, which is

$$Q = \frac{\pi d_c^4}{128\eta} \left[ \frac{-dp}{dz} \right] \quad (12)$$

where  $d_c$  = diameter of capillary.

As before, one can eliminate the negative sign by substituting  $\Delta P/L$  for  $[-dp/dz]$ . This gives

$$Q = \frac{\Delta P \pi d_c^4}{128L\eta} \quad (13)$$

Substituting the radius for diameter and rearranging gives

$$Q = \frac{\Delta P r_c^2 \pi r_c^2}{8L\eta} \quad (14)$$

where  $r_c$  = radius of capillary.

Switching the fluid flow term from volumetric flow rate to fluid velocity, one may write

$$\mu_c = \frac{\Delta P r_c^2}{8L\eta} \quad (15)$$

where

$$\mu_c = \frac{Q}{\pi r_c^2} \quad (16)$$

which is the mean fluid velocity in a capillary.

Thus, in general terms, one can represent the relationship between mean fluid velocity and pressure gradient expressed in Eq. (15) as

$$\mu_c = \frac{K_c \Delta P r_c^2}{L\eta} \quad (17)$$

where  $K_c$  = Giddings’ implicit permeability coefficient appropriately chosen to correspond to the meaning of  $\mu_c$ .

Giddings now makes the transition from the capillary model to the packed bed. He accomplishes this by *intuitively* maintaining the same general relationship between mean flow velocity and the other variables. In other words, he makes like substitutions on both sides of the equality sign, and incorporates an *experimentally verified* permeability coefficient, thus maintaining the validity of the equality. Accordingly, (i) he replaces the  $\mu_c$  term with an equivalent velocity term  $\mu_t$  and (ii) he replaces the  $r_c^2$  term with a dimensionally equivalent term  $d_p^2$ , and (iii) he replaces the implicit permeability coefficient  $K_c$  with the dimensionless parameter  $\phi'$ , which is a modified form of a term  $\phi$  known in the chromatographic literature as the “flow resistance parameter.” This is a term that relates *measured* pressure gradient and *mobile phase velocity* to other measurable column parameters. In so doing, he equates the term  $K_c$  to the reciprocal of  $2\phi'$  (i.e.,  $K_c = 1/2\phi'$ ).

Thus, substituting for  $\mu_c$ ,  $r_c$ , and  $K_c$ , gives

$$\mu_c = \frac{\Delta P d_p^2}{2\phi' L \eta} \quad (18)$$

where  $\phi'$  = Giddings' modified flow resistance parameter.

The numerical value of 2 that appears in the denominator of Eq. (18) would appear to be redundant. It adds nothing to the concept of the flow resistance parameter, which is a recognizable parameter to practicing chromatographers. However, Giddings had an ulterior motive for putting it in, as shall be demonstrated below.

### 3. IDENTIFYING THE VALUE FOR $P_0$

#### 3.1 Nonporous Particles

Giddings states that the value of  $\phi'$  has been determined experimentally in his laboratory to be 300 for nonporous particles (see p. 207 in Giddings, 1965).

Therefore, substituting for  $\phi'$  in Eq. (18) gives

$$\mu_t = \frac{\Delta P d_p^2}{600 L \eta} \quad (19)$$

Substituting for  $\mu_t = \mu_i = \mu_s/\varepsilon_0$  and rearranging gives

$$\frac{\Delta P}{L} = \frac{600 \mu_s \eta}{\varepsilon_0 d_p^2} \quad (20)$$

Now one can relate Eq. (20) to the general form of the Kozeny-Blake equation and solve for the value of  $P_0$ . Eliminating terms common to both equations gives

$$P_0 = \frac{600 \varepsilon_0^2}{(1 - \varepsilon_0)^2} \quad (21)$$

Substituting Giddings' typical value of 0.4 for  $\varepsilon_0$  in well-packed columns gives

$$P_0 = 267$$

His statement in his later textbook corroborates the assumption that Giddings' columns contained an external porosity of 0.4 (Giddings, 1991). If a value of 270 is used for  $P_0$  in the above Eq. (21), we get a value of 0.4015 for  $\varepsilon_0$ , which is within Giddings' specified range for  $\varepsilon_0 = .40 \pm 0.03$  for a well-packed column (p. 199 in Giddings, 1965).

#### 3.2 Porous Particles

Discounting the contribution of diffusion by combining the mobile phase velocity with Giddings' parameter  $\Phi$ , one may re-express Eq. (19) as

$$\frac{\mu_t}{\Phi} = \frac{\Delta P d_p^2}{600 L \eta} \quad (22)$$

Substituting for  $\mu_t/\Phi = \mu_i = \mu_s/\varepsilon_0$  and rearranging results once again in Eq. (19). Accordingly, by substituting the value of 0.4 for  $\varepsilon_0$ , it follows that the value for  $P_0$  is 267.

### 4. AN ELABORATION OF GIDDINGS' TABLE 5.3-1 RANGE OF $\phi'$ VALUES

Table 1 herein contains an extrapolation of the data in Giddings' Table 5.3-1. It illustrates his methodology of arriving at his rounded value of 270 for  $P_0$  and is based on his suggestion that "... the most *practical* approach to the study of pressure drop-particle size-flow relationships in granular-bed chromatography is through the use of equations (5.3-7) and (5.3-8)" (p. 209), both of which are based on the factor  $\Phi$ . It is obvious from the table, then, that Giddings carried the customary assumptions for typical columns packed with both porous and nonporous particles. The first two rows of the table contain these details. The third and fourth rows of the table represent Giddings' range of measurements of  $\phi'$  values for the columns that contain the nonporous glass beads. Note that the range of his  $\phi'$  values demonstrates that while they were all *close* to having an external porosity of 0.4, his assumption for a typical column, neither one had *exactly* a value of 0.4. Alumina and ChromaSorb, on the other hand, are both porous materials. Their measured  $\phi'$  values are contained in the remaining rows of the table. In the case of these porous particles, Giddings used a combination of his measured values for column total porosity  $\varepsilon_t$ , taken in columns packed with the porous particles themselves, and his measured values for external porosity  $\varepsilon_0$  (which is the same as  $\varepsilon_t$ ), taken in columns packed with his nonporous glass beads, to compute his  $\Phi$  parameter. Giddings' comment that "It was necessary to approximate  $\Phi$  (inter-particle fraction of void) as 0.5 to calculate  $\phi'$  for alumina and Chromasorb" simply indicates that these materials have a higher specific pore volume than typically assumed for porous particles. In Table 1, this process is captured by demonstrating that when the values for  $\phi'$ ,  $\varepsilon_0$ , and  $\varepsilon_t$  are input into the Giddings' equation in combination with the dependent variable  $\Phi$ ,

**TABLE: 1** Elaboration of Giddings' Table 5.3-1 range of  $\phi'$  values

Particle Description	$\phi' = \phi\Phi/2$	$2\phi$	$\varepsilon_0$	$(1 - \varepsilon_0)^2$	$\varepsilon_t$	$\Phi$	$\phi = 2\phi'/\Phi$	$P_0\phi = \varepsilon_0^3 / ((1 - \varepsilon_0)^2 \varepsilon_t)$
Giddings' typical non-porous column	300	600	0.40	0.36	0.40	1.00	600	267
Giddings typical porous column	300	600	0.40	0.36	0.60	0.67	900	267
50/60 mesh glass beads	250	500	0.42	0.33	0.42	1.00	502	267
50/60 mesh glass beads	280	560	0.41	0.35	0.41	1.00	562	267
30/40 mesh alumina	300	600	0.40	0.36	0.80	0.50	1,204	267
50/60 mesh alumina	260	520	0.42	0.34	0.84	0.50	1,043	267
60/80 mesh chromasorb W (5% DNP)	350	700	0.38	0.38	0.77	0.50	1,404	267
60/80 mesh chromasorb W (20% DNP)	330	660	0.39	0.37	0.79	0.50	1,333	267

the back-calculated value for  $P_0$  is 267 (approximately 270).

## 5. GIDDINGS' ATTEMPT TO RECONCILE WITH CARMAN

In recognition of the fact that Giddings could not rely on any theoretically derived value for the permeability coefficient between pressure gradient and fluid velocity (because none had been developed in 1965 and, incidentally, none has yet been published), he had to fall back on the only empirically determined value available to him at that time. This was Carman's rework of the Kozeny-Blake equation, in which Carman allegedly validated a value of 180 for the correlation coefficient. Accordingly, he gives the following preamble to his inclusion of the multiplier of 2 in Eq. (37): "Many investigators, starting with Slichter, have obtained expressions for the dependence of permeability on porosity. By far, the best-known expression is the Kozeny-Carman equation, although its content was largely anticipated by Blake (1921). These approximate equations can be derived from capillary models using an empirical parameter. The derivation will not be repeated here since it is discussed in the standard references (e.g., Carman, 1937; Scheidegger, 1957). The Kozeny-Carman equation gives the specific permeability as  $K_0 = d_p^2 f_0^3 / [180(1 - f_0)^2]$  [Eq. (5.3-10) in Giddings text]. The parameter  $\phi'$ , related to  $K_0$  in Eq. (5.3-9) (in Giddings text), is thus found to be  $\phi' = [90(1 - f_0)^2] / f_0^2$  [Eq. (5.3-11) in Giddings text] and is thus a function only of the interparticle porosity  $f_0''$ ."

The "empirical parameter," which Giddings was referring to in the model for capillary flow, is obviously Carman's coefficient of 180; hence; his need to add the multiple of 2 to align his development with that of Carman. Accordingly, he defines his implicit correlation coefficient thusly

$$K_c = \frac{1}{2\phi'} \quad (23)$$

where 2 = Giddings' reconciliation factor for Carman's value of 180.

By 1991, however, even though there still was no extant theoretical derivation of the value of  $P_0$ , Giddings had apparently concluded that he wanted to abandon his attempt to align his experimental results with Carman's value of 180. Accordingly, he discarded in his new text (Giddings, 1991) his use of the modified flow resistance parameter  $\phi'$  and his correction factor of 2. As we noted above, the new form of his equation simply used the classic flow resistance parameter without modification, which he stated was found empirically to range from 500 to 1000, depending on column *and* particle porosity, i.e., twice the value that he had used in 1965 for his corrected, modified flow resistance parameter. And, of course, he finally stated forthrightly that the value of  $P_0$  in the Kozeny-Carman equation is really 270.

## 6. CONCLUSIONS

Giddings anchors his methodology for assessing the permeability of columns packed with granular particles on the measured and velocity and the classical definition

of porosity. In addition, it is based on the concept that the pressure gradient and column porosity measurements are taken simultaneously, which necessitates that they are taken in the same fluid and thus insuring that both are self-calibrating. Moreover, it is based on the use of total column porosity in conjunction with known values for  $\Phi$  instead of column external porosity. This is Giddings' method of engineering around the difficulty of differentiating between the free space between the particles and the free space within the particle fraction of a column packed with porous particles. Accordingly, when compared to the general format of the Kozeny-Blake equation, and, in particular, accepting the validity of the porosity dependence term therein, Giddings' empirical equation validates a value of 267 for the permeability coefficient  $P_0$ . This is an important conclusion because it removes any doubt concerning the slope of a line achieved when fluid velocity is plotted against pressure gradient in a packed column containing either porous or nonporous particles and, therefore, is of utmost importance to the practicing engineer or chromatographer. Furthermore, Giddings' theoretical framework of relating the flow of fluid in a capillary to the flow of fluid in a packed column is an elegant enhancement to the work of Darcy (1856). Indeed, it is an appropriate companion to the ingeniously conceived experiments of the latter and the simple elegance of his sand-filled pipes.

## REFERENCES

- Blake, F. C., The resistance of packing in fluid flow, *Trans. Am. Inst. Chem. Eng.*, Vol. 14, pp. 415–421, 1921.
- Carman, P. C., Flow through granular beds, *Trans. Am. Inst. Chem. Eng.* Vol. 15, 1937.
- Churchill, S. W., *Viscous Flows, The Practical Use of Theory*, Butterworths, Stoneham, 1988.
- Coulson, J. M., The streamline flow of liquids through beds composed of spherical particles, PhD Thesis, University of London, 1935.
- Darcy, H., *Les Fontaines Publiques de la Ville de Dijon*, Victor Dalmont, Paris, 1856.
- Dugeon, C. R., An experimental study of the flow of Water through coarse granular media, *Houille Blanche*, vol. 7, p. 785, 1966.
- Dullien, F. L., *Porous Media, Fluid Transport and Pore Structure*, Academic Press, New York, 1992.
- Finnemore, E. J. and Franzini, J. B., *Fluid Mechanics with Engineering Applications*, 10th ed., McGraw-Hill, New York, 2002.
- Giddings, J. C., *Dynamics of Chromatography, Part I, Principles and Theory*, Marcel Dekker, New York, 1965.
- Giddings, J. C., *Unified Separation Science*, Wiley, Hoboken, NJ, 1991.
- Giloaguén, E., Chonteau, M., Marcott, D., and Chapuis, R., Estimation of hydraulic conductivity of an unconfined aquifer using cokriging of GBR and hydrostratigraphic data, *J. Appl. Geophys.*, vol. 47, no. 2, 135–152, 2001.
- Gupte, A. R., PhD Dissertation, University Karlsruhe, 1970.
- Happel, J. and Brenner, H., *Low Reynolds Number Hydrodynamics with Special Application to Particulate Media*, Prentice-Hall, Englewood Cliffs, NJ, 1965.
- Moura Neto, F. and Melo, S. T., Darcy's law for a heterogeneous porous medium, *J. Porous Media*, vol. 4, no. 2, p. 165–178, 2001.
- Moura Neto, F. D., Paes Leme, P. J. Amaral Souto, H. P., and Vargas, A. S., Inertial and second grade effects on macroscopic equations for the flow of a fluid in a porous medium, *Transport Porous Media*, vol. 33, pp. 205–226, 1998.
- Sanchez-Palencia, E., *Non Homogeneous Media and Vibration Theory*, Lecture Notes in Physics, Vol. 127, Springer-Verlag, Berlin, 1980.
- Scheidegger, A. E., *The Physics of Flow through Porous Media*, MacMillan Co., New York, 1957.
- Whitaker, S., Flow in porous media I: A theoretical derivation of Darcy's law, *Transport Porous Media*, vol. 1, pp. 3–25, 1986.